Identification of Cosmic Nuclei with the CALET Electron Telescope on the International Space Station

Università degli Studi di Siena

DIPARTIMENTO DI SCIENZE FISICHE DELLA TERRA E DELL'AMBIENTE
SEZIONE DI FISICA

Identification of Cosmic Nuclei with the CALET Electron Telescope on the International Space Station

Tesi di Dottorato di Ricerca in Fisica Sperimentale
In Partial Fulfillment of the Requirements for the Ph. D. Degree in Experimental Physics

Candidate:
Francesco Stolzi

Supervisor:
Prof. Pier Simone Marrocchesi

Tutor:
Dott. Paolo Brogi

Ciclo di Dottorato XXIX

Contents

Introduction

CALET (CALorimetric Electron Telescope) is a high energy astroparticle physics experiment designed for long-term observations of high-energy Cosmic Rays (CRs) on the International Space Station (ISS). The mission is funded by the Japanese Space Agency (JAXA), in collaboration with the Italian Space Agency (ASI) and NASA. CALET reached the ISS on August 24, 2015 and, at the time of writing, the instrument is operating in science data mode: a two year period of observations has started with a target of 5 years. The purpose of the experiment is to perform precise measurements of high energy cosmic rays, with an extensive physics program that includes the detection of possible nearby sources of high energy electrons; searches for signatures of dark matter in the spectra of electrons and γ rays; monitoring gamma-ray transients and solar modulation; long exposure observations of cosmic nuclei from proton to iron and trans-iron elements; measurements of the CR relative abundances and secondary-to-primary ratios. The telescope is an all-calorimetric instrument, with a total thickness of 30 radiation length (X_0) and 1.3 proton interaction length (λ_I), preceded by a particle identification system. The instrument is composed of three main subsystem: at the top a Charge Detector (CHD) identifies the individual chemical elements in the cosmic-ray flux, then a fine granulated pre-shower IMaging Calorimeter (IMC) is followed by a Total Absorption Calorimeter (TASC) measuring the energy released. The CHD is designed to provide incident particle charge measurement over a wide dynamic range, from Z = 1 to Z = 40 with sufficient charge resolution to resolve individual elements. The IMC can image the early shower profile and reconstruct the incident direction of cosmic rays with good angular resolution. The TASC measures the total energy of the incident particle and discriminates electrons and gamma-rays from hadrons.

The main subject of the present thesis is the study of the performance of CALET in the identification of cosmic nuclei, by combining both IMC and CHD detectors. A clear identification of the incoming nuclei and the measurement of their energy is crucial both to measure absolute fluxes and the ratio of the fluxes of secondary-to-primary elements. From measurements of the energy dependence of the flux ratio it is possible to discriminate among different models of CR propagation in the galaxy.

The first chapter of the thesis provides an introduction to cosmic-ray physics, cosmic-ray propagation and acceleration. In chapter 2 the CALET instrument is described in detail and the anticipated telescope performances and the experimental program are reported. Chapters 3 and 4 include the original work of this thesis. The third chapter is focused on two aspects of the energy calibration process: the first one related to the energy position dependence correction in CHD, the second one to the correction for the quenching effect in the CHD and IMC. The fourth chapter is focused on the identification of cosmic nuclei: charge tagging using both the IMC and the CHD and the performance in terms of the charge resolution of both detectors are described in view of an accurate determination of light element fluxes with CALET. Finally in chapter 5 an overview on the current status of the CALET mission is given.

Chapter 1

Cosmic Rays

Direct experimental information about the properties of matter in the Universe can be gained not only with the detection of electromagnetic radiation of cosmic origin, but also with the study of cosmic-ray (CR) particles. The latter belong to a class of emitted energy known as *non-thermal* and their energy distribution is often characterized by a featureless spectrum that follows a single (or a broken) power law.

In this chapter, after a brief introduction on the discovery and the origin of this particles, the propagation and the acceleration mechanism of cosmic ray are described.

1.1 Introduction: cosmic-ray history

Cosmic-ray experimental investigation began in the early XX century, when it was discovered that electroscopes underwent discharge losses even if they were kept in darkness and far away from sources of natural radioactivity. In 1912 and in 1913, first Hess and then Kolhörster measured the ionisation of the atmosphere as a function of altitude with pioneering scientific balloon flights (Hess, 1912 [1]; Kolhörster, 1913 [2]). They found that the ionization rate from cosmic rays was greater at higher altitude than at sea level. This was clear evidence that the source of the ionising radiation must be located above the Earth's atmosphere.

In 1929, Skobel'cyn constructed a cloud chamber to study the properties of the electrons emitted in radioactive decays. Some of the tracks that he observed were hardly deflected at all and were found to be electrons with energies greater than $15 MeV$. He identified them as secondary electrons produced by the *Hess ultra-γ radiation*. These were the first pictures of the tracks produced by cosmic rays (Skobel'cyn, 1929 [3]).

In 1930, Millikan and Anderson studied the trajectories of particles passing through their cloud chamber that used an electromagnet stronger than Skobel'cyn's. Anderson observed curved tracks identical to those of electrons but with positive electric charge (Anderson, 1932 [4]). This discovery was confirmed by Blackett and Occhialini in 1933 using an automatic cloud chamber triggered when a cosmic ray passed through the instrument's volume. (Blackett and Occhialini, 1933 [5]). The existence of this particle, was predicted at the same time by Dirac. It was the discovery of the positron and consequently the first evidence of the existence of anti-matter.

The cloud chamber experiments showed that cosmic ray particles initiated showers of charged particles. Most of the high energy particles observed at the surface of the Earth are, in fact, secondary, tertiary (or higher) products of very high energy cosmic rays entering the atmosphere. In 1939 Pierre Auger reported a larger number of coincidences between widely separated detectors with respect to the predicted accidental rate. He found that the cosmic radiation events were coincident in time, meaning that they were associated with a single event: an air shower (Auger et al., 1939 [6]). The particles responsible for initiating the showers must have energies exceeding $10^{15} eV$ at the top of the atmosphere. This was direct evidence for the acceleration of charged particles to extremely high energies in astronomical sources.

The astrophysical study of the origin and propagation of the cosmic rays could take advantage of direct measurements from the 1960s when cosmic-ray particle detectors were flown on satellites. These observations established many crucial facts about the primary particles present in the cosmic radia-

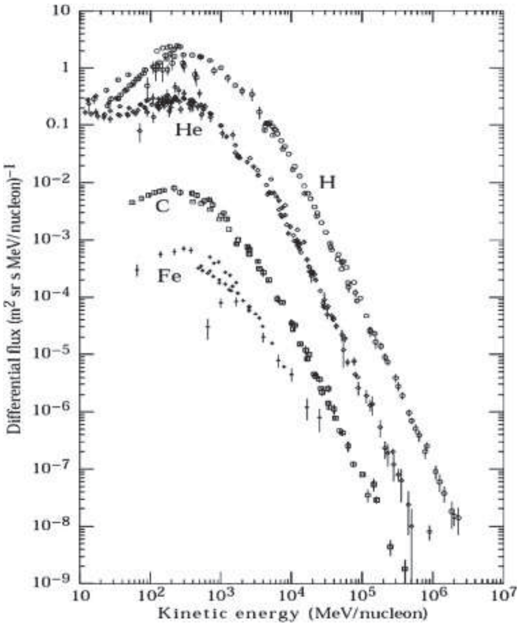

Figure 1.1: *The differential energy spectrum of cosmic rays as measured from above the Earth's atmosphere (Simpson, 1983 [7]).*

tion; first of all, the energy spectra. In the region where the energy spectrum is unaffected by the Solar Wind, the spectrum for protons, electrons and nuclei with energies in the range $10^9 - 10^{14} eV$ can be described by a power-law:

$$dN/dE = KE^{-\gamma} \tag{1.1.1}$$

with $\gamma \approx 2.5 - 2.7$ (Fig. 1.1).

The chemical composition of the cosmic rays is similar to the abundances of the elements in the solar system with some important exceptions, particularly for the light elements such as lithium, beryllium and boron that are present with higher abundances in cosmic rays.

At the very highest energies, above $10^{14} eV$, cosmic rays are detected by large air shower arrays located on the surface of the Earth. One of the most important point about this very high energy (VHE) particle is their origin. Their arrival directions seem to be isotropic over the sky, from the first observations by the huge Auger air-shower array in Argentina. Now, small anisotropies are being searched for in the arrival directions of the highest energy cosmic rays. In addition, the expected cut-off in the spectrum above about $3 \times 10^{19} eV$ due to interactions with photons of the Cosmic Microwave Background Radiation is studied.

1.1.1 The energy spectrum of cosmic rays

The energy spectrum of cosmic rays covers an energy range of about fourteen orders of magnitude from MeV to $10^{20} eV$. As shown in Fig. 1.2, the CR flux has a power-law behaviour that indicates a non-thermal origin of the particles. At energies below $Gev/nucleon$ the energy spectrum shows a pronounced cut-off relative to the power law observed at high energies. This phenomenon, known as solar modulation, is due to the fact that the cosmic-ray particles diffuse in towards the Earth from interstellar space through the outflowing Solar Wind. The higher is the solar activity, the larger the disturbances in the interplanetary magnetic field which interfere with the propagation of particles with energies less than about $1 GeV/nucleon$ [1].

As mentioned above, for energies above $10^9 eV$ the energy spectrum can be represented well by power-law (1.1.1) and it can be subdivided into three regions:

from 10^9eV to 10^{15}eV In this region the spectral index is $\gamma \approx 2.7$, and the origin of CR is linked to the supernovae remnants in the Galaxy. Particles up to an energy of about $100\, TeV$ can be measured directly by experiments on balloons or satellites, but for higher energies the flux is too small to be measured directly, because a typical detection area of the order of $1 m^2$ requires a too long observation time with respect to the average duration of a balloon flight.

from 10^{15}eV to 10^{19}eV In this region the spectral index is $\gamma \approx 3.1$. At this energy the sources (e.g.AGN) of CR are assumed to be extra-galactic.

[1] A detailed description of Solar modulation can be found in the following references [9], [10].

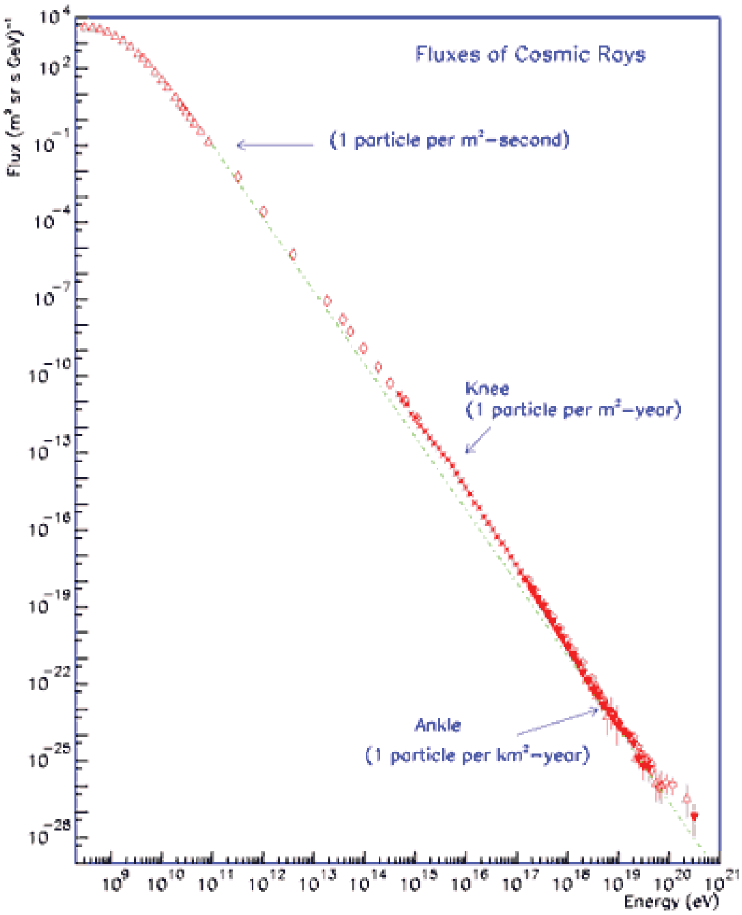

Figure 1.2: *The cosmic ray spectrum measured at the top of the atmosphere. Above an energy of* $10^9 eV$ *the spectrum shows a power-law behavior. The integrated flux above the ankle is about 1 cosmic ray per* km^2 *year (Swordy, 2001 [8]).*

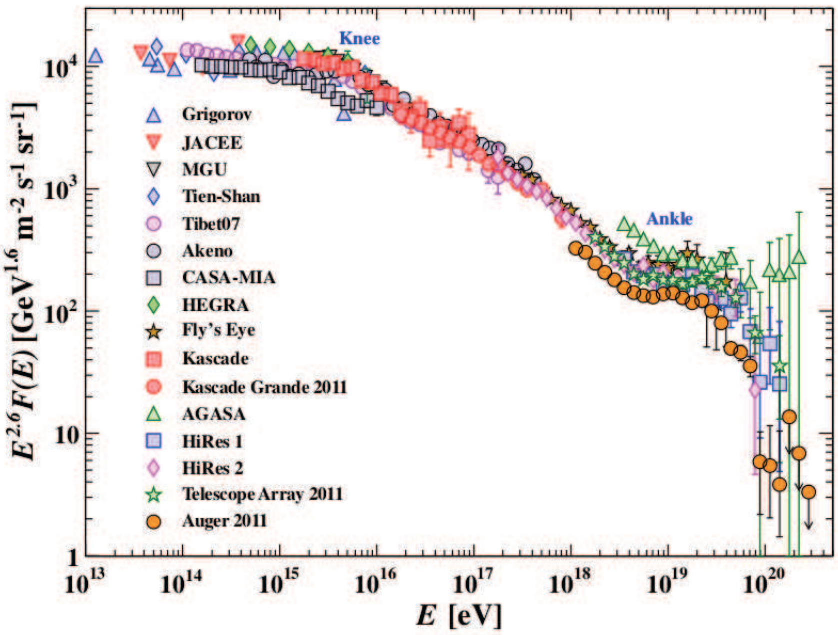

Figure 1.3: *The differential energy spectrum of high energy cosmic rays presented in the form $dN/dE(E) \times E^{2.6}$ (Beringer et al., 2012 [11]).*

The cosmic radiation is studied by observing extensive air showers. Ground based experiments use the atmosphere above them as the detection medium, and hence, the detection area can be increased considerably compared to balloon or satellite experiments.

above 10^{19}eV In this region the spectral index tends to flatten again: $\gamma \approx 2.7$. Cosmic rays have such large Lorentz factors that photons of the Cosmic Microwave Background Radiation have very high energies in the rest frame of the cosmic ray and so photo-pion and photo-pair production can take place, which degrade the energy of the cosmic ray.

To reveal small structures in the energy spectrum, the flux is usually multiplied by the energy to some power. The all-particle energy spectrum multiplied by $E^{2.6}$ is shown in Fig. 1.3. In this representation some spectral features can be identified. The first one is the so-called knee at about $4.5\,PeV$, where the power-law spectral index changes from $\gamma \approx 2.7$ to $\gamma \approx 3.1$. The second feature is the probable presence of a second knee at about $400\,PeV$, where the spectrum exhibits a second steeping to $\gamma \approx 3.3$. The presence of this second knee is not so evident and its existence is not yet established. Another feature of the energy spectrum is the so-called ankle at energies of about $10^{19} eV$.

1.1.1.1 The Greisen-Kuzmin-Zatsepin (GZK) cut off

At an energy above $5 \times 10^{19} eV$ Greisen, Kuzmin and Zatsepin predicted a drastic reduction of CR flux (Greisen, 1966 [12]; Zatsepin and Kuzmin, 1966 [13]). This cutoff (GZK) is based on the interactions between cosmic rays and the photons of the cosmic microwave background radiation (CMB).

They independently showed that cosmic rays with energies over a threshold energy of $5 \times 10^{19} eV$would interact with blue shifted cosmic microwave background photons γ_{CBM} to produce pions via the Δ resonance:

$$\gamma_{CBM} + p \Longrightarrow \Delta^+ \Longrightarrow p + \pi^0 \tag{1.1.2}$$

$$\gamma_{CBM} + p \Longrightarrow \Delta^+ \Longrightarrow n + \pi^+ \tag{1.1.3}$$

According to this prediction the cosmic ray flux for energies above the threshold energy would decrease. This process is often called photo-disintegration. The collision of a $10^{20} eV$ proton with a $1/40 eV$ photon produces about $200 MeV$ in the center of mass, which is the peak for photo-pion production. The mean energy of a nucleon as a function of the propagation distance through the CMB is shown in Fig. 1.4. Its interaction with the CMB is a stochastic process where a significant amount of energy can be lost in a single collision. At the end of this process the cosmic particle, at about $100 Mpc$ from the source, reaches the GZK limit [14] [2]. Thus the energy loss length of cosmic ray is comparable with the distance of the closest galaxy clusters and only local sources should be seen at these energies.

[2] note that our Galaxy dimension is about 24 Kpc.

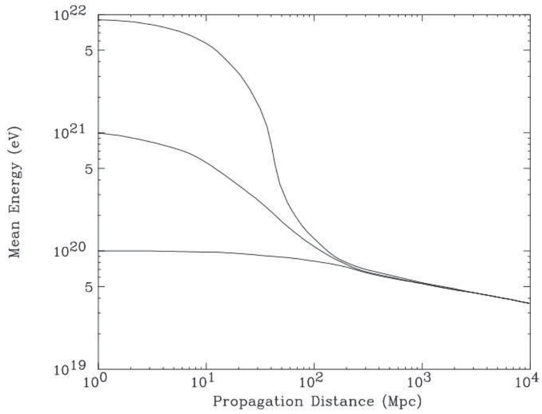

Figure 1.4: *Mean energy of protons as a function of propagation distance through the CMB. Curves are for source energies of* $10^{22}eV$*,* $10^{21}eV$*, and* $10^{20}eV$*.(Cronin, 2003 [14]).*

1.1.2 Chemical composition and relative abundances of cosmic rays

Direct measurements of the chemical composition and spectra of cosmic rays have been carried out with balloon and space experiments. Complementary measurements have been performed with ground telescopes, but in this case the identification is not direct: the primary nuclei are identified studying their interactions with the atmosphere. A compilation of direct observations, collected so far at energies lower than 100 TeV, are shown in Fig. 1.5. About 98% of cosmic rays are protons and nuclei while about 2% are electrons. Of the protons and nuclei, about 87% are protons, 12% are helium nuclei and the remaining 1% are heavier nuclei.

Primary cosmic rays are those particles accelerated at astrophysical sources and secondaries are those particles produced as a result of their interactions with the interstellar medium. Thus electrons, protons and helium, as well as carbon, oxygen, iron, and other nuclei synthesized in stars, are primaries. Nuclei such as lithium, beryllium, and boron (which are only marginally abundant end-products of stellar nucleosynthesis) are secondaries. Antiprotons and positrons are also in large part secondary. Whether a small fraction

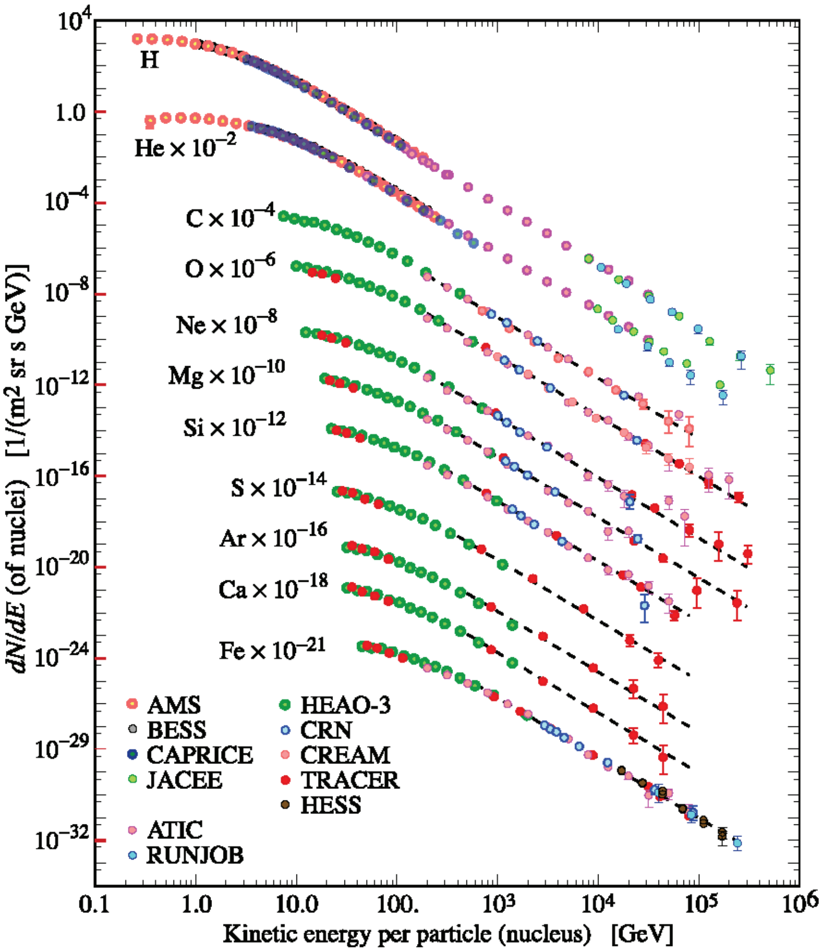

Figure 1.5: *Fluxes of nuclei of the primary cosmic radiation (Beringer et al., 2012 [11].)*

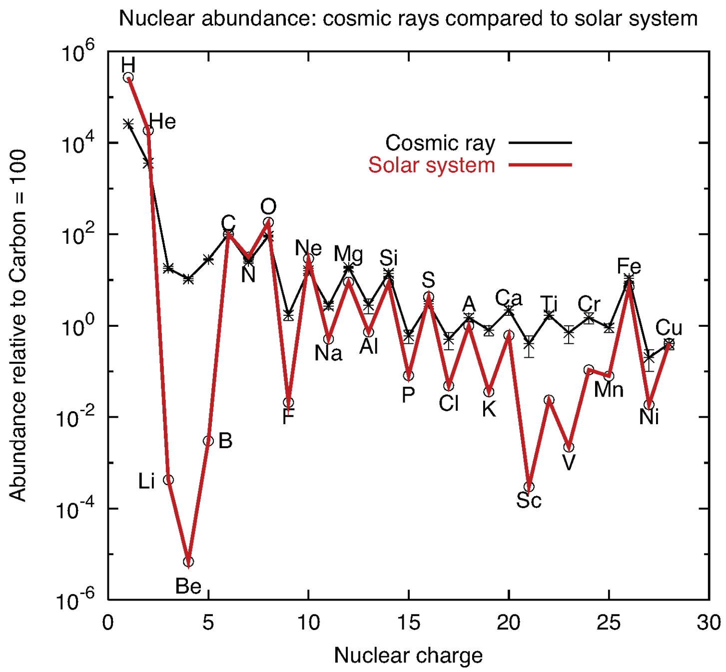

Figure 1.6: *Relative abundances in cosmic rays compared with solar system abundance.*

of these particles may be primary is a question of current debate. Fig. 1.6 reveals the overall similarities and differences between the abundances of the cosmic rays in the Solar System and in the ISM. The following features are evident:

(i) the relative abundance of elements in CRs is very similar to the abundance found in the solar system, which indicates that CRs are ordinary matter, but accelerated to very high energies. In particular the abundance peaks at carbon, nitrogen and oxygen and at the iron group are present both in the cosmic ray and Solar System abundances;

(ii) the odd-even effect in the relative stabilities of the nuclei according to atomic number, known to be present in the Solar System abundances of the elements, is also present in the cosmic rays but to a somewhat lesser degree;

(iii) the light elements, lithium, beryllium and boron are grossly overabundant in the cosmic rays relative to their Solar System abundances;

(iv) there is an excess abundance in the cosmic rays of elements between about calcium and iron;

(v) cosmic rays are deficient in H and He, which is not fully understood. It may indicate that heavy elements are easier to ionize and accelerate or it is a direct reflection of the source composition.

Some of the differences, specifically items **(iii)** and **(iv)** listed above, can be attributed to spallation in the interstellar medium between the sources of the cosmic rays and their arrival at the Earth. In these collisions, the cosmic ray nuclei are stripped of their electrons and fragmented, resulting in the production of nuclei with atomic and mass numbers lower than those of the primary nuclei. Therefore, the relative abundances of secondary nuclei with respect to their progenitors give a measure of the average amount of material that cosmic rays typically traverse between injection and observation.

In addition to overall chemical abundances, isotopic abundances are available for a number of species. The very lightest stable elements, ^1H, ^2H, ^3He and ^4He, form a special group of isotopes. Most of the helium was synthesised in the hot phase of Big Bang through the *p-p* chain while matter and radiation cooled down. ^2H and ^3He are present in very much larger abundances in the cosmic rays than they are in the interstellar medium and can be attributed to spallation reactions between the four species. These elements provide an independent check of the spallation models: their abundances are so much greater than those of the other elements that the spallation products of elements such as carbon, oxygen and nitrogen do not contribute significantly to the relative isotopic abundances of hydrogen and helium.

Some of the species created in spallation reactions are radioactive and hence, if the production rates of the different isotopes of a given element are known, information can be obtained about the time taken to reach the Earth from their sources. One of these cosmic ray clocks is the isotope ^{10}Be

which has a radioactive half-life of 1.5×10^6years, therefore a very useful discriminant to determine the typical lifetime of the spallation products in the vicinity of the Earth.

1.2 Acceleration mechanisms and sources

The basis of any mechanisms of CR acceleration in space up to very high energies is the interaction of individual particles with huge moving ensembles of particles through magnetic fields and induced electric fields. These moving ensembles (mass ejections, clouds, shock waves, magneto-hydrodynamic waves, etc.) have a huge kinetic energy many orders higher than the energy of an individual particle. Therefore the energy increase of the collective movement will lead to the gain of the energy of individual particles, and their energy become many orders higher than the energy of background plasma particles. The acceleration of an individual particle is possible only if the gain of energy per unit of time is larger than the loss of energy. The loss of energy depends on the mass m_{ac}, charge Ze, and kinetic energy E_k of the particle, as well as upon properties of background plasma, magnetic field intensity and electromagnetic radiation. The energy loss is especially important at small kinetic energies E_k (mostly ionization losses). In the intermediate energy region the energy loss per unit of time becomes much smaller than the energy gain, and the energy spectrum of accelerated particles will be dominated mainly by the rate of energy gain and probability of accelerated particles escaping from the acceleration volume. In the very high energy region, the losses of energy again become important. These energy losses and CR escaping from the acceleration volume lead to a significant deformation of the power energy spectrum $\propto E^{-\gamma}$ with a gradual increase of the power index γ as the particle energy increases. Let us start with the statistical mechanism of charged particle acceleration.

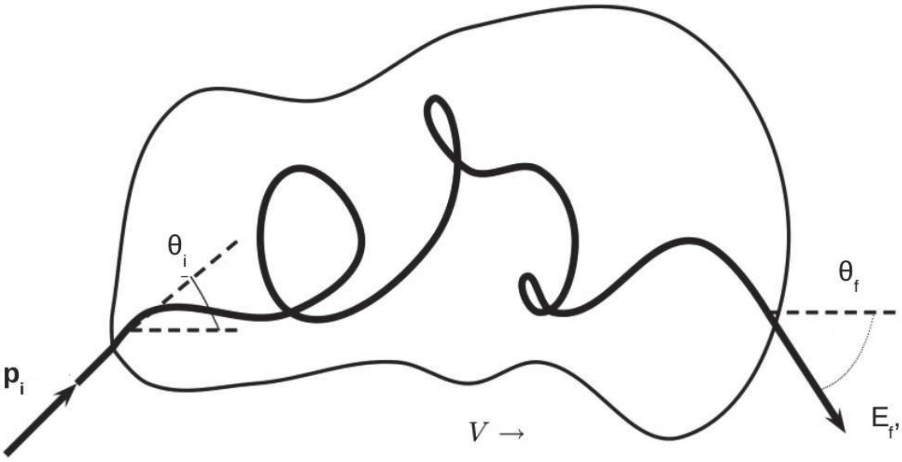

Figure 1.7: *Elastic scattering of a cosmic ray with a magnetic cloud moving with velocity V.*

1.2.1 The mechanism of Diffusive Shock Acceleration

1.2.1.1 Second order Fermi mechanism

In 1949 Fermi [15] proposed a stochastic mechanism to accelerate particles through moving magnetic clouds.

Let us consider a cosmic ray with initial energy E_i *scattering* elastically on a magnetic cloud that moves with velocity $V \ll c$. Let us derive the energy gain $\xi = (E_f - E_i)/E_i$ per scattering. The variables E_i, θ_i and E_f, θ_f are shown in Fig. 1.7, and the *prime* and *unprime* notation denotes the cloud system and the lab system respectively. After the diffusion process has taken place inside the cloud, the average motion of the particle coincides with that of the gas cloud. The energy gain of the particle, which emerges at an angle θ_f with energy E_f, can be obtained by applying Lorentz transformations between the laboratory frame and the cloud frame. In the rest frame of the moving cloud, the cosmic ray particle has a total initial energy

$$E_i^{'} = \gamma E_i (1 - \beta cos\theta_i) \tag{1.2.1}$$

where $\gamma = \frac{1}{\sqrt{1-\beta^2}}$ and $\beta = V/c$ are the Lorentz factor and velocity of the cloud, respectively. Since the scattering off magnetic irregularities is collisionless and the cloud is very massive (so that its velocity is unchanged in the collision) energy is conserved, $E_f^{'} = E_i^{'}$. After Lorentz transformation, in the laboratory frame the energy of the particle after its encounter with the cloud is

$$E_f = \gamma E_f^{'}(1 + \beta cos\theta_f^{'}) \tag{1.2.2}$$

Hence it is possible to eliminate $E_f^{'}$ and to obtain as relative energy gain

$$\xi = \frac{E_f - E_i}{E_i} = \frac{1 - \beta cos\theta_i + \beta cos\theta_f^{'} - \beta^2 cos\theta_i cos\theta_f^{'}}{1 - \beta^2} - 1 \tag{1.2.3}$$

To proceed, one needs the average values of $cos\theta_i$ and $cos\theta_f^{'}$. But the cosmic ray scatters off magnetic irregularities many times in the cloud, so its exit direction is randomized, $\langle cos\theta_f^{'} \rangle = 0$. The collisionless scattered particle will gain energy in a head-on collision ($\theta_i > \pi/2$) and lose energy by tail-end ($\theta_i < \pi/2$) scattering. The collision rate of the cosmic ray with the cloud is proportional to their relative velocity ($v - V cos\theta_i$). For ultrarelativistic particles, $v \to c$, and the collision rate is

$$\frac{dn}{d\Omega_i} \propto (1 - \beta cos\theta_i). \tag{1.2.4}$$

$\langle cos\theta_i \rangle$ is obtained by averaging $cos\theta_i$ weighted by $\frac{dn}{d\Omega_i}$ over all angles so that

$$\langle cos\theta_i \rangle = -\frac{\beta}{3} \tag{1.2.5}$$

Plugging the value of $\langle cos\theta_f^{'} \rangle$ and $\langle cos\theta_i \rangle$ into Eq. (1.2.3) and taking into account that $\beta \ll 1$ gives as average gain

$$\langle \xi \rangle = \frac{1 + \beta^2/3}{1 - \beta^2} - 1 \simeq \frac{4}{3}\beta^2. \tag{1.2.6}$$

Thus $\xi \propto \beta^2 > 0$ and on average a cosmic ray gains energy scattering on *magnetic clouds* with velocity V.

The energy gain per scattering is however only of second order in the small parameter β, and acceleration is therefore rather inefficient.

The power law spectrum can be derived in the following way. Knowing the average time between collisions, the energy rate from (1.2.6) is:

$$\frac{dE}{dt} = \frac{4}{3}\frac{V^2}{cL}E = \alpha E \tag{1.2.7}$$

where L is the mean free path between clouds, along the field lines. Then it is possible to find the energy spectrum $N(E)$ by solving a diffusion-loss equation in the steady state and considering this energy rate, plus the assumption that τ_{esc} is the characteristic time for a particle to remain in the accelerating region. The diffusion-loss equation is

$$\frac{dN}{dt} = D\nabla^2 N + \frac{\partial}{\partial E}[b(E)N(E)] - \frac{N}{\tau_{esc}} + Q(E) \tag{1.2.8}$$

that, with the conditions $\frac{dN}{dt} = 0$ (steady-state solution), $D\nabla^2 N = 0$ (diffusion), $Q(E) = 0$ (no source). Keeping in mind that the energy loss term is $b(E) = -\frac{dE}{dt} = -\alpha E$, it reduces to

$$-\frac{\partial}{\partial E}[\alpha E N(E)] - \frac{N}{\tau_{esc}} = 0. \tag{1.2.9}$$

Differentiating with respect to E and rearranging one finds that

$$N(E)dE = const. \times E^{-1-\frac{1}{\alpha\tau_{esc}}}dE. \tag{1.2.10}$$

The second-order acceleration succeeds in generating a power-law spectrum, but it is not a completely satisfactory mechanism. Infact, on account of the observed low cloud density, the energy gain is very slow. Furthermore, the mechanism fails to explain the observed value of 2.7 for the exponent in the power-law spectrum: the energy spectrum depends strongly on the cloud parameters $\alpha\tau_{esc}$.

Acceleration at shocks, as summarized in the next paragraph, avoids both disadvantages.

1.2.1.2 First order Fermi mechanism

A more efficient acceleration may occur in the vicinity of plasma shocks occurring in astrophysical environments. This is the so called first-order

Fermi acceleration mechanism. The key feature of this process is that the acceleration is first order in the shock velocity and automatically results in a power-law spectrum with energy spectral index $\gamma \approx 2$.

Let us first write the essence of the original Fermi mechanism in a slightly different way. Let us define the constants β and P as follows: $E = \beta E_0$ is the average energy of the particle after one collision and P is the probability that the particle remains within the accelerating region after one collision. Then, after k collisions, there are $N = N_0 P^k$ particles with energies $E = E_0 \beta^k$. Eliminating k between these quantities,

$$\frac{ln(N/N_0)}{ln(E/E_0)} = \frac{lnP}{ln\beta} \Rightarrow \frac{N}{N_0} = \left(\frac{E}{E_0}\right)^{\frac{lnP}{ln\beta}} \tag{1.2.11}$$

where N is the number of particles with energy $> E$, since this is the number that reaches energy E and some fraction of them continue to be accelerated to higher energies. Therefore

$$N(E)dE = const. \times E^{-1+(\frac{lnP}{ln\beta})} dE. \tag{1.2.12}$$

The equivalence with the derivation of Fermi acceleration follows from Eq. (1.2.11), namely, $(lnP/ln\beta) = -(\alpha\tau_{esc})^{-1}$.

The diffusive shock acceleration process is first-order Fermi acceleration in the presence of strong shock waves and was discovered independently by a number of researchers in the late 1970s (Axford, Leer and Skadron (1977) [16], Krymsky (1977) [17], Bell (1978) [18] and Blandford and Ostriker (1978) [19]). Let us follow Bell's approach.

The model involves a strong shock propagating through a diffuse medium, for example, the shock waves which propagate through the interstellar medium ahead of the supersonic shells of supernova remnants. The main points are:

- a flux of high energy particles is assumed to be present both in front of and behind the shock front;

- the particles are assumed to be propagating at speeds close to that of light and so the velocity of the shock is very much less than the speed of the high energy particles;

- the high energy particles scarcely notice the shock at all since its thickness is normally very much smaller than the gyroradius of the high energy particle;

- because of scattering by streaming instabilities or turbulent motions on either side of the shock wave, when the particles pass though the shock in either direction, they are scattered so that their velocity distribution rapidly becomes isotropic in the frame of reference of the moving fluid on either side of the shock.

A strong shock wave travels at a highly supersonic velocity $U \gg c_s$, through stationary interstellar gas with density ρ_1 , pressure p_1 and temperature T_1, where c_s is the sound speed in the ambient medium, the Mach number M being U/c_s. The density, pressure and temperature behind the shock are ρ_2, p_2, T_2, respectively (Fig. 1.8 a). In the frame of reference in which the shock front is at rest the upstream gas flows into the shock front at velocity $v_1 = U$ and leaves the shock with a downstream velocity v_2 (Fig. 1.8 b). The equation of continuity requires mass to be conserved through the shock

$$\rho_1 v_1 = \rho_1 U = \rho_2 v_2 \tag{1.2.13}$$

In the case of a strong shock, $\rho_2/\rho_1 = (\gamma + 1)/(\gamma - 1)$ where γ is the ratio of specific heat capacities of the gas. For a monatomic or fully ionised gas $\gamma = 5/3$, so $\Rightarrow \rho_2/\rho_1 = 4$ and $v_2 = (1/4)v_1$ (Fig. 1.8 b).

Let us consider high energy particles ahead of the shock. Scattering ensures that the particle distribution is isotropic in the frame of reference in which the gas is at rest. The shock advances through the medium at velocity U but the gas behind the shock travels at a velocity $(3/4)U$ relative to the upstream gas (Fig. 1.8 c). When a high energy particle crosses the shock front, it increase its energy of ΔE. The particles are then scattered in

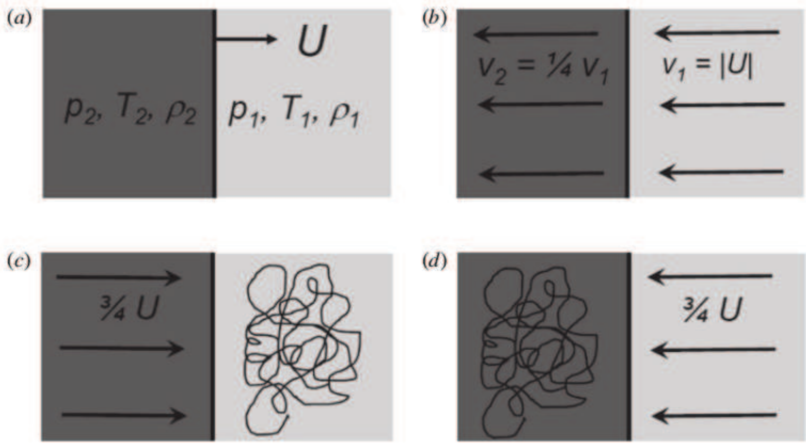

Figure 1.8: *The dynamics of high energy particles in the vicinity of a strong shock wave.*
(a) A strong shock wave propagating at a supersonic velocity U through stationary interstellar gas with ρ_1, p_1, T_1 . The density, pressure and temperature behind the shock are ρ_2, p_2, T_2 respectively;
(b) The flow of interstellar gas in the vicinity of the shock front in the reference frame in which the shock front is at rest. In this frame of reference, the ratio of the upstream to the downstream velocity is $v_1/v_2 = 4$ as shown in the figure;
(c) The flow of gas as observed in the frame of reference in which the upstream gas is stationary and the velocity distribution of the high energy particles is isotropic;
(d) The flow of gas as observed in the frame of reference in which the downstream gas is stationary and the velocity distribution of high energy particles is isotropic.

the region behind the shock front so that their velocity distributions become isotropic with respect to that flow.

Let us consider the opposite process whereby the particle diffuses from behind the shock to the upstream region in front of the shock (Fig. 1.8 d). Now the velocity distribution of the particles is isotropic behind the shock and, when they cross the shock front, they encounter gas moving towards the shock front, again with the same velocity (3/4)U. Even in this case the particle increases its energy by ΔE. Every time the particle crosses the shock front it receives an increase of energy (there are never crossings in which the particles lose energy) and the increment in energy is the same going in both directions. Thus in the case of the shock front, the collisions are always head-on and energy is transferred to the particles.
According to Eq. (1.2.12) β and P have to be determined to derive the power law spectrum. Let us evaluate the average increase in energy of the particle when crossing from the upstream to the downstream sides of the shock. The gas on the downstream side approaches the particle at a velocity $V = (3/4)U$ and so, performing a Lorentz transformation [3], the particle's energy when it passes into the downstream region is

$$E^{'} = \gamma_V (E + p_x V) \tag{1.2.14}$$

(p_x perpendicular to the shock). As shock is non relativistic ($V \ll c$), but the particle is relarivistic ($E = pc$, $p_x = (E/c)cos\theta$)

$$\begin{aligned} \Delta E = E^{'} - E = \gamma_V (E + p_x V) - E = (E + p_x V) - E = \\ = (pc + (pc/c)cos\theta V) - pc = pcos\theta V \end{aligned} \tag{1.2.15}$$

e

$$\frac{\Delta E}{E} = \frac{V}{c} cos\theta \tag{1.2.16}$$

The probability that the particles which cross the shock arrives within the angles θ to $\theta + d\theta$ is proportional to $sin\theta\, d\theta$ and the rate at which they approach the shock front is proportional to the x-component of their velocities,

[3]with $\gamma_V = \frac{1}{\sqrt{1-\beta^2}}$ and $\beta = V/c$.

$ccos\theta$. Therefore the probability (taking into account the particles with angle θ in the range 0 to $\pi/2$) of the particle crossing the shock is

$$P(\theta) = 2sin\theta cos\theta d\theta \tag{1.2.17}$$

and the average gain in energy on crossing the shock is

$$\left\langle \frac{\Delta E}{E} \right\rangle = \frac{V}{c} \int_0^{2\pi} 2cos^2\theta sin\theta d\theta = \frac{2}{3}\frac{V}{c}. \tag{1.2.18}$$

When the particle recrosses the shock it gains another fractional increase in energy $(2/3)(V/c)$. Therefore, in one round trip the fractional energy increase is,

$$\left\langle \frac{\Delta E}{E} \right\rangle = \frac{4}{3}\frac{V}{c}. \tag{1.2.19}$$

and finally

$$\beta = \frac{E}{E_0} = 1 + \frac{4V}{3c} \tag{1.2.20}$$

Now let us calculate the escape probability P.

The average number of particles crossing the shock in either direction is $1/4Nc$ (N is the number density of particles) since, as noted above, the particles scarcely notice the shock. The particles are removed from the region of the shock at a rate $NV = 1/4NU$. Thus, the fraction of the particles lost per unit time is $(1/4NU)/(1/4Nc) = U/c$. Then, the escape probability $P = 1 - (U/c)$.

Therefore,

$$\frac{lnP}{ln\beta} = \frac{ln(1 - U/c)}{ln(1 + 4V/3c)} \sim \frac{-U/c}{U/c} = -1 \tag{1.2.21}$$

Hence, the energy spectrum is

$$N(E)dE = \propto E^{-2}dE. \tag{1.2.22}$$

In spite of not having obtained the observed exponent of 2.7 yet, the first-order mechanism is very promising, being the most effective and probable one, since shock waves are expected to be present in different astrophysical environments. In addition, in contrast to the second-order mechanism, the model provides a constant numerical value for the exponent.

There is an upper limit to the energy to which particles can be accelerated by this mechanism (Lagage and Cesarsky (1983) [20]). The basic problem is that the first-order acceleration mechanism is a process which is not rapid enough. In the case of a supernova, the blast wave is decelerated once the remnant has swept up roughly its own mass of interstellar gas and then enters the Sedov phase of evolution. Although the acceleration mechanism continues throughout the life of a supernova remnant until it dissolves into the interstellar medium after about $10^5 - 10^6 years$, most of the particle acceleration occurs during the undecelerated blast wave phase which lasts less than about $10^3 years$ [20]. The maximum attainable energy of a particle in a magnetic field of flux density B and scale L can be estimated according to the following argument due to Syrovatskii.

The induced electric field in the region of interest can be extimated by,

$$\nabla \times \mathbf{E} = -\frac{\partial \mathbf{B}}{\partial t} \tag{1.2.23}$$

This equation, whereby U is the speed of the shock, can be rewritten to order of magnitude as

$$\frac{E}{L} \sim \frac{B}{L/U} \Rightarrow E \sim BU \tag{1.2.24}$$

The particle of charge Ze accelerated by the induced electric field has an energy

$$E_{max} = \int ZeEdx = ZeBUL = ZeBU^2t \tag{1.2.25}$$

For a young supernova remnants, $B = 10^{-10}T$, $U = 10^4 km/s$ and $t \approx 10^3 years$, and the maximum energy per nucleon is

$$E_{max} \sim 10^{14} eV. \tag{1.2.26}$$

More recent estimates give a maximum energy up to one order of magnitude larger for some type of supernova [21]

$$E_{max} \sim 5 \times 10^{15} eV. \tag{1.2.27}$$

Equations (1.2.25) show that heavier nuclei can be accelerated to higher energies. This would imply the existence of consecutive cut-offs in the energy spectra for individual elements proportional to their charge Z, starting with the proton component. This issue is not yet confirmed by direct experiments as they cannot yet reach the PeV scale for individual nuclei. The supernova acceleration model works well below the knee, but it fails to predict a sufficient number of CRs above $10^{15} eV$. Moreover, since the gyroradius r in the galactic magnetic field at $\sim 10^{18} eV$ is of the same order of the size of the galactic disk, a transition from galactic to extra-galactic cosmic rays may occur at this energy scale.

1.2.2 Sources of high energy cosmic rays

The changes in the slope of the energy spectrum and in the composition from protons to iron in the knee region suggest that there are at least two different kinds of cosmic ray sources. If, on the one hand the bulk of cosmic rays can be produced by Galactic sources, on the other hand the highest energy cosmic rays may have an extragalactic origin, being generated by more powerful galaxies than ours. A further argument favoring an extragalactic origin of cosmic rays with the highest energies is the observed isotropy of their arrival directions on large scales that suggests a cosmological distribution of their sources.

1.2.2.1 Energy from Supernova remnants (SNR)

The standard theory suggests that the bulk of cosmic rays (of energy below the knee) is accelerated in blast waves of super-novae remnants (SNR). The idea was justified by Ginzburg and Syrovatskii [22] through arguments based on the energetics of SNR. Let us assume that a volume around the galactic disk V_{GD} is uniformly populated by cosmic rays that are contained in this volume for a time t_{GD}, then the power needed to accelerate these particle can be estimated: let us take $V_{GD} = \pi(15\,kpc)^2(500\,pc) \sim 10^{67} cm^3$ (a disk of radius $\sim 15\,kpc$ and height $\sim 500\,pc$), the cosmic-ray energy density $\rho_e \sim 0.5\,eV/cm^3$ and $t_{GD} = 10^7 y$.
The power required to replenish the cosmic rays that leak out of the galactic

disk is

$$L_{CR} = \frac{V_{GD} \cdot \rho_e}{t_{GD}} = 3 \times 10^{40} erg/s \tag{1.2.28}$$

Three SNR of $10M\odot$ expanding with velocity of $5 \times 10^8 cm/s$ per century produce $3 \times 10^{42} erg/s$. Thus an acceleration efficency of only 1% would account for the energy content of the cosmic rays in the galactic disk. SNRs are attractive candidates for cosmic rays acceleration because they are large and live enough to carry out the acceleration process to high energy. The acceleration mechanism is belived to be stochastic acceleration at supernova blast shock.

1.2.2.2 Hillas Plot

A simple argument (Hillas, 1984 [23]) can be used to evaluate an upper bound for the energy which can be reached in the acceleration process. Let us consider extragalactic objects to be accelerated to energies exceeding $10^{20} eV$.

The first requirement for the acceleration of charged nuclei is that the magnetic field of the accelerating object (hereafter referred to as accelerator) contains the accelerated nucleus within the accelerator itself. Thus, the Larmor orbit $R_L = E/(ZeB)$ of accelerated particles has to fit inside the accelerator of size R, $R_L < R$. For known magnetic fields B and source sizes, one can constrain thus the maximal achievable energy

$$E_{max} = \gamma ZeBR \tag{1.2.29}$$

as it is done in Fig. 1.9 for a compilation of potential cosmic ray sources. In this figure, known as Hillas plot, the characteristic magnetic field B of each candidate cosmic accelerator is plotted versus its characteristic size R, for proton. Few candidate sources for acceleration to $E = 10^{20} eV$ seem to be compatible with Hillas argument. On the one hand, this constraint looks like a solid upper limit, because energy losses are neglected, the maximal acceleration time is finite and no accelerator is 100% efficient. On the other hand, nonlinear processes may lead to an amplification of magnetic fields

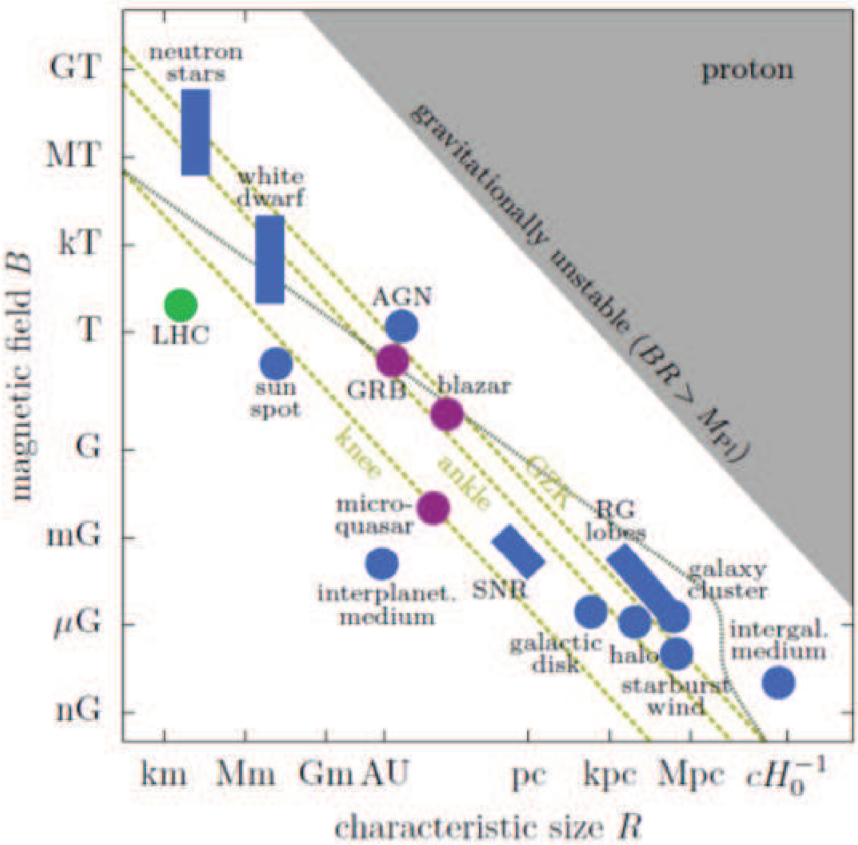

Figure 1.9: *Magnetic field strength versus size of various suggested cosmic ray sources. The yellow dashed lines show the lower limit for accelerators of protons at the CR knee ($\sim 10^{6.5}GeV$),CR ankle ($\sim 10^{9.5}GeV$) and the GZK suppression ($\sim 10^{10.6}GeV$). The gray area correspond to astrophysical environments with extremely large magnetic field energy that would be gravitationally unstable.(M. Ahlers et al. [24])*

inside the source. In general, sources neither too small (minimizing energy losses) nor too large (avoiding too long acceleration times) are favored.

1.3 Cosmic-ray propagation

Once accelerated, cosmic rays propagate through the interstellar medium before detection. The interstellar medium contains matter, magnetic fields and radiation fields, all of which are targets for cosmic ray interactions. Cosmic ray protons scatter in the magnetic fields and slowly diffuse away from their sources. Cosmic-ray nuclei interact mostly with the interstellar matter and produce all kinds of secondary particles. Electrons interact with the magnetic and radiation fields, as well as with the interstellar matter. In the magnetic fields they generate synchroton radiation, and in the radiation fields they boost gamma rays via the inverse Compton effect.

Most of the interstellar diffuse matter consists of hydrogen (only about 10% is helium and heavier nuclei) in the form of atomic neutral hydrogen (HI) and molecular hydrogen (H_2). Atomic H is present in the galactic arms at an average density of about $1\,atom/cm^3$ and the disk has a scale height of $100 - 150pc$. Molecular hydrogen is concentrated within the solar circle and especially in the galactic center. The average density H_2 within the solar circle is about $1\,cm^{-3}$. A much smaller fraction of the matter is in the form of ionized hydrogen of density $0.03\,cm^{-3}$. The ionized hydrogen has been detected well above the galactic disk with a height of about $700pc$. It is reasonable to assume that the disk contains a mixture of a neutral and ionized hydrogen. A good round number for the interstellar matter density is $1\,nucleon/cm^3$ [10].

Although there are strong fluctuations in the strength of the magnetic field and in the density of matter there are models that could be used to study the propagation of charged particles in the galaxy. The ionized gas and the associated magnetic field form a magnetohydrodynamic (MHD) fluid. It supports waves that travel with Alfven velocity. Cosmic rays scatter on these waves in their propagation.

The energy in MHD waves equals the energy density of the magnetic field,

$$\frac{\rho v_A}{2} = \frac{B^2}{8\pi} \tag{1.3.1}$$

For an average field of $3\,mG$ the energy density of the magnetic field is $\approx 0.25eV/cm^3$ smaller of the energy density of $\approx 0.5 - 1\,eV/cm^3$ carried by cosmic rays. Cosmic rays propagating in the interstellar medium must also induce Alfven waves which in turn act as scattering centers.

1.3.1 General Transport equation

The equation of cosmic rays transport is due to Ginzburg and Syrovatskii [22].

Let us write the cosmic ray propagation equation for a particular particle species in the general form (Strong, Moskalenko, 1998 [25]). This equation is valid for all types of particles and includes all the physical processes that cosmic rays experience in the acceleration and propagation in the Galaxy.

$$\begin{aligned}\frac{\partial n(\vec{r},p,t)}{\partial t} =& Q(\vec{r},p,t) + \vec{\nabla}\cdot(D_{xx}\nabla n - \vec{V_c}n) + \frac{d}{dp}p^2 D_{pp}\frac{d}{dp}\frac{1}{p^2}n + \\ & - \frac{\partial}{\partial p}[\dot{p}n - \frac{p}{3}(\vec{\nabla}\cdot\vec{V_c})n] - \frac{1}{\tau_f}n - \frac{1}{\tau_r}n\end{aligned} \tag{1.3.2}$$

were:

$n(\vec{r},p,t)$ is the particle density per unit of momentum p at position $\vec{r}$ and at time t.

$Q(\vec{r},p,t)$ is the source term, including primary, spallation and decay contributions;

D_{xx} is the spatial diffusion coefficient which is in general a function of $(\vec{r},\beta,R)$ where R is the rigidity (the momentum per unit of charge $R = p/Ze$);

$\vec{V_c}$ is the convection velocity, due to galactic wind;

D_{pp} is the diffusion tenson in momentum space and it describes diffusive reacceleration due to scattering of cosmic rays by Alfven waves. Defining the Alfven velocity V_a as characteristic velocity of weak disturbances propagating in a magnetic field, D_{pp} can be estimated as $D_{pp} = p^2 V_a / 9 D_{xx}$.

$\vec{\nabla} \cdot \vec{V_c}$ represents adiabatic momentum gain or loss in the non-uniform flow of gas with a frozen-in magnetic field whose inhomogeneities scatter the CR.

τ_f, τ_r are the time scale for fragmentation losses and the time scale for radioactive decay respectively.

The injection spectrum of primary nucleons is assumed to be a power law in momentum for the different species

$$\frac{dQ(p)}{dp} = p^{-\gamma} \tag{1.3.3}$$

where γ can vary with species. The spallation contributions of the source term $Q(\vec{r}, p, t)$ is $Q(\vec{r}, p) = \beta c n_p(\vec{r} p)[\sigma_H^{sp}(p)\rho_H(\vec{r}) + \sigma_{He}^{sp}(p)\rho_{He}(\vec{r})]$, where $\sigma_H^{sp}(p)$, $\sigma_{He}^{sp}(p)$ are the production cross sections for the secondary product from the progenitor on H and He targets, $\rho_H(\vec{r})$, $\rho_{He}(\vec{r})$ are the interstellar hydrogen and helium number densities, and $n_p(\vec{r} p)$ is the progenitor density.

Starting with the solution for the heaviest primaries and using this to compute the spallation source for their products, the complete system can be solved including secondaries, tertiaries etc. Then the CR spectra observed at Earth can be compared with direct observations, including solar modulation if required.

1.3.2 The transfer equation for light and stable nuclei

Let us consider the transport equation in a suitable approximation for light and stable nuclei. In this case the decay term in equation (1.3.2) is set to zero. Since several experimental data suggest that CR did not change significantly over the last hundred million years the term $\partial n/\partial t$ is set to zero (steady-state solution). Also, neglecting ionization loss term $\frac{\partial}{\partial p}[\dot{p}n]$ because of the high energy range of CR (GeV/n), neglecting the diffusion reacceleration term D_{pp} and galactic wind V_c, the equation for each nuclei species i is

$$Q_i + \nabla \cdot (D_i \nabla n_i) - \frac{1}{\tau_i} n_i + \sum_{j>i} \frac{P_{ji}}{\tau_{j\to i}} n_i = 0 \tag{1.3.4}$$

The third term in the equation represents the spallation losses, the last term represents the spallation gain of all species with $j > i$. P_{ji} is the probability that, in an inelastic collision, involving the destruction of the nucleus j, the species i is created. Expressing the spallation contributions in terms of inelastic collision cross section, the equation becomes

$$-Q_i - \nabla \cdot (D_i \nabla n_i) + \rho_{ISM}\beta c \sigma_i n_i - \sum_{j>i} \rho_{ISM}\beta c \sigma_{k\to i} n_j = 0 \tag{1.3.5}$$

where ρ_{ISM} is the density of interstellar medium, and $\sigma_{k\to i}$ the partial cross-section for the production of the nucleus i from the break-up of a nucleus of type k.

Let us decouple the equation into two parts: the first one describing the astrophysical aspects of the cosmic ray propagation, the second one describing the fragmentation by nuclear interactions with the interstellar medium. For this scope let us assume that the spatial distribution of sources is independent of the kind of nuclei, $Q_i(\vec{r}) = q_i \chi(\vec{r})$ where q_i are constants that determine the abundances of the nuclei at the sources. In this way the solution for transfer equation has the form [26]

$$n_i(\vec{r}) = \int_0^\infty n_i^{(\sigma)}(x) G(\vec{r}, x) dx. \tag{1.3.6}$$

$n_i^{(\sigma)}(x)$ and $G(\vec{r}, x)$ satisfy the following equation:

$$\rho_{IMS}\beta c \frac{\partial G}{\partial x} - \nabla \cdot (D \nabla G) = 0 \qquad \text{with } \rho_{IMS}\beta c G(\vec{r}, 0) = \chi(\vec{r}) \tag{1.3.7}$$

$$\frac{dn_i^{(\sigma)}}{dx} + \sigma_i n_i^{(\sigma)} - \sum_{j>i} \sigma_{j\to i} n_j^{(\sigma)} = 0 \qquad \text{with } n_i^{(\sigma)}(0) = q_i \tag{1.3.8}$$

The function G, known as path-length distribution, has to satisfy the boundary conditions for $n_i(\vec{r})$ related to the geometry of the containment volume. $G((\vec{r}), x)$ states that the cosmic-ray density at the position $\vec{r}$ is obtained by averaging the composition expressed by $n_i(x)$ over the distribution of path lengths $G(\vec{r}, x)$ traveled by CRs from their sources to the point $\vec{r}$.

$n_i^{(\sigma)}(x)$ represent the variation of the cosmic-ray composition due only to fragmentation processes after traversing an amount x of matter, and they are related only to the nuclear cross-sections.

1.3.3 The Leaky-Box Model

The main processes in the propagation process are described in the *Leaky-Box* approximation, which is a well accepted approximation to particle diffusion in the Galaxy. The leaky box model states that CRs propagate in the Galaxy containing their sources but when CRs reach the boundary they bounce elastically and at every step they can escape from it with certain probability P.

The model has two main requirement:

- particles traverse the galactic plane many times before escaping into the intergalactic medium;
- quantities all over the galaxy are spatially averaged so that the density of cosmic rays is constant.

Physically, the diffusion takes place rapidly so that, in the diffusion equation (1.3.5) the second term can be approximated according to the following replacement

$$\nabla \cdot (D_i \nabla n_i) \rightarrow \frac{n_i}{\tau_{esc}} \tag{1.3.9}$$

where $\tau_{esc} = \lambda_{esc}/(\rho_{ISM}\beta c)$ is the lifetime of CRs in the Galaxy and λ_{esc} is the mean amount of matter traversed by the CRs in the Galaxy before they escape from it.

According to the model, the motion of particles inside the propagation region is free motion. With the above replacement, the equation (1.3.5) becomes

$$-\frac{n_i}{\lambda_{esc}} + \sigma_i n_i = \frac{q_i}{\rho_{ISM}\beta c} + \sum_{j>i} \sigma_{j\to i} n_j^{(\sigma)} \tag{1.3.10}$$

where $\sigma_i = 1/\lambda_i$. With these approximations the cosmic rays propagation is described, for the various kinds of nuclei i, by a set of algebraic equations that can be solved analytically. In equation (1.3.10) the only parameter of the model is λ_{esc}. With the leaky box model it is possible to obtain an analytic solution of equation (1.3.7). After the replacement of the diffusion term with the escape term, the path-length distribution function can be expressed as:

$$G_{leaky}(x) = e^{-x/\lambda_{esc}} \tag{1.3.11}$$

and the solution of equation (1.3.10) for the differential intensity n_i of a cosmic-ray species i is

$$n_i = \frac{1}{\lambda_{esc}^{-1} + \lambda_i^{-1}} \times \left(\frac{q_i}{\rho_{ISM}\beta c} + \sum_{j>i} \frac{n_i}{\lambda j \to i} \right) \tag{1.3.12}$$

With the leaky box model it is possible to obtain information on the parameter λ_{esc} from the ratio of stable secondary-to-primary abundances.

Let us consider, for example, a secondary nucleus of type S whose only parent nucleus is of type P. In this case the equation (1.3.10) is reduced to a system of two equations:

$$\frac{q_P}{\rho_{ISM}\beta c} - \frac{n_P}{\lambda_P} - \frac{n_P}{\lambda_{esc}} = 0 \tag{1.3.13}$$

$$-\frac{n_S}{\lambda_S} - \frac{n_S}{\lambda_{esc}} + \frac{n_P}{\lambda_{P\to S}} = 0 \tag{1.3.14}$$

with the following solution for the secondary to primary ratio

$$\frac{S}{P} = \frac{n_S}{n_P} = \frac{\lambda_{esc}/\lambda_{P\to S}}{(1 + \lambda_{esc}/\lambda_S)} \tag{1.3.15}$$

for $\lambda_S \gg \lambda_P$ it become

$$\frac{S}{P} = \frac{\lambda_{esc}}{\lambda_{P\to S}} \tag{1.3.16}$$

In the extreme case of a secondary nucleus with a long interaction mean free path, the ratio S/P is directly proportional to the escape mean free path of CRs from the Galaxy.

1.3.4 Secondary to primary ratio

As explained in sec. 1.1.2 there are groups of elements that are overabundant by many order of magnitude, with respect to the solar system. The first one is the group of light elements Li, Be, B. The sub-Iron element Sc, Ti, V, Cr and Mn are also overabundant by about three orders of magnitude.

The reason for the *surplus* are the interactions of accelerated cosmic ray nuclei with the interstellar matter which produce the overabundant elements as spallation products. These elements are secondary elements in cosmic rays composition. The measured ratio of secondary to primary cosmic rays can be used to compute the mean amount of interstellar matter that cosmic rays have encountered before reaching the Earth.

Since for a given charge the diffusion process depends on the particle velocity, i.e. energy, one does not expect to have the same primary to secondary ratio at all energies. Higher energy nuclei will have shorter escape times and the flux of secondary elements should decrease with energy.

The study of the energy dependence of the secondary to primary ratio establishes the energy dependence of the containment time for cosmic rays in the Galaxy. Using measurements like the one shown in Fig. 1.10 one could fit the energy dependence of λ_{esc}. One of the most sensitive parameter is the secondary to primary ratio is B/C, as B is purely secondary and its main progenitors C and O are primaries. The B/C flux ratio is a clean and direct probe of propagation mechanisms, and it is considered as the standard tool for studying propagation models. Indeed, as a ratio of two nuclei with similar Z, it is less sensitive to systematic errors and to Solar modulation (at low energy) than single fluxes or other ratios of nuclei with more dissimilar charges. For the same reasons, the sub-Fe/Fe may also be useful. The B/C flux ratio, as well as the absolute boron and carbon fluxes, has been

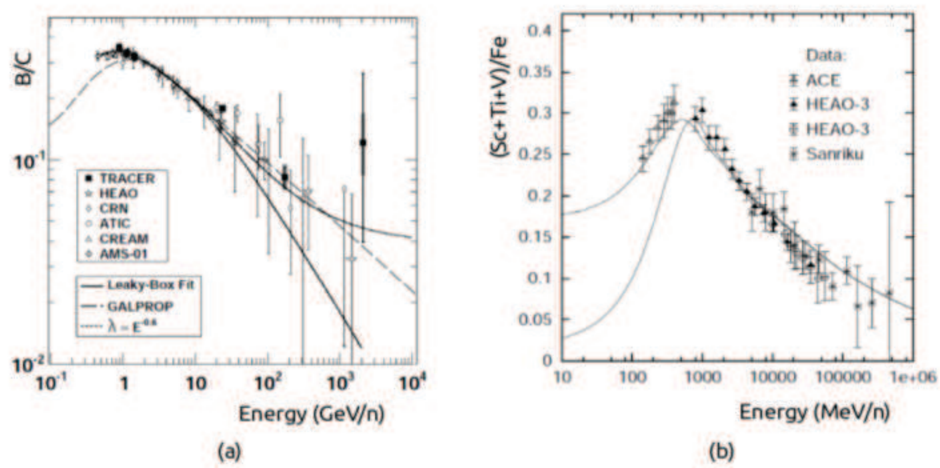

Figure 1.10: *a) The boron-to-carbon and (b) SubFe/Fe abundance ratio as a function of kinetic energy per nucleon for various experiments (A. Obermeier et al, 2011 [27]),(Strong and Moskalenko, 2001 [28]).*

measured by balloon-borne and by space-based experiments (Engelmann et al., 1990 [29]; Swordy et al., 1990 [30]; Webber et al., 2002 [31]; Aguilar et al., 2010 [32]; Lave et al., 2013 [33]; Oliva et al., 2013 [34]), with different techniques and spanning various energy ranges from about $80MeV/n$ up to few TeV/n. However, secondary-to-primary measurements on balloons suffer from the severe limitations of the residual systematic uncertainty on the subtraction of the irreducible background due to the atmospheric overburden at flight altitude.

Let us summarize some results about CRs propagation derivable using the leaky box model.

- At energies of few Gev/n the observed abundances of the stable secondary nuclei Li, Be, B and Sc, Ti, V, produced by the spallation of the nuclei C, N, O and Fe, are well described by assuming an escape length of $\lambda_{esc} = 5 - 10g/cm^2$.

  For ρ_{ISM} of 1 nucleon per cm^3 this corresponds to an escape time

$\tau_{esc} \approx 10^7 y$ [4]. Therefore it can be inferred that cosmic rays travel on average distances through the galaxy a factor hundred larger than the size of the galaxy ($10^5 ly$).

- The energy dependence of the secondary to primary ratio can be explained assuming an escape path length for particles with rigidity $R = pc/Ze$ and velocity β of the form [35]

$$\lambda_{esc}(R) = \frac{26.7\beta g/cm^2}{\left(\frac{\beta R}{1.0G}\right)^{\delta} + \left(\frac{\beta R}{1.4G}\right)^{-1.4}} \tag{1.3.17}$$

  with $\delta \approx 0.5 - 0.6$. From the observation, the decrease of the ratio of boron to carbon with the energy suggests that higher energy particles have a shorter escape time and traverse less matter. It implies that the acceleration occurs before the propagation (else the ratio would be constant or increase with energy).

- From Eq. (1.3.17), at high energies, λ_{esc} becomes

$$\lambda_{esc}(R) = \lambda_0 \left(\frac{R}{R_0}\right)^{-\delta} \tag{1.3.18}$$

  with $\lambda_0 \approx 10 - 15 g/cm^2$ and $R_0 \approx 4GV$ [36]. In this scenario at Earth one should observe a steepening of the acceleration spectrum from $E^{-\gamma}$ at acceleration to $E^{-(\gamma+\delta)}$ after propagation. For $\delta = 0.6$ this would suggest an acceleration spectrum with $\gamma = 2.1$, compatible with the spectral shape derived by a first order Fermi mechanism, to fit the $E^{-2.7}$ observed energy spectrum of cosmic rays.

The spallation processes during the CR propagation also influence the shape of the spectra. It is assumed that the energy spectra of all elements have the same spectral index at the source. Taking the path length of the particles in the Galaxy into account, it is found that the spectra of heavy nuclei observed at Earth should be flatter as compared to the light elements

[4] $\tau_{esc} = N_A \lambda_{esc}/c$

[37]. This fact is supported by direct measurements of individual energy spectra, e.g. the values for protons $\gamma_p = -2.71 \pm 0.02$ and iron $\gamma_{Fe} = -2.59 \pm 0.06$ differ as expected.

Chapter 2

The CALET experiment on the ISS

CALET (CALorimetric Electron Telescope) is a high energy astroparticle physics experiment planned for a long exposure mission aboard the International Space Station (ISS) by the Japanese Aerospace Exploration Agency (JAXA), in collaboration with the Italian Space Agency (ASI) and NASA.

CALET reached the ISS on August 24, 2015 and was emplaced on the Exposure Facility attached to the Japanese Experiment Module Kibo (JEM-EF). At the time of writing, the instrument is operating in science data mode transmitting data to the ground stations. A 2 years period of observations has started with a target of 5 years. The CALET telescope will perform precise measurements of high energy cosmic rays, extending the measurements performed by PAMELA, HEAT, AMS, FERMI, AGILE in space, by balloons in the upper atmosphere and by ground-based instruments including Atmospheric Cherenkov Telescopes (ACT). CALET is in a position to address many of the outstanding questions in high energy astrophysics with an extensive physics program that includes the detection of possible nearby sources of high energy electrons; searches for signatures of dark matter in the spectra of electrons and γ rays; long exposure observations of cosmic nuclei from proton to iron and trans-iron elements; measurements of the CR relative abundances and secondary-to-primary ratios. Moreover, CALET is monitoring gamma-ray transients and solar modulation.

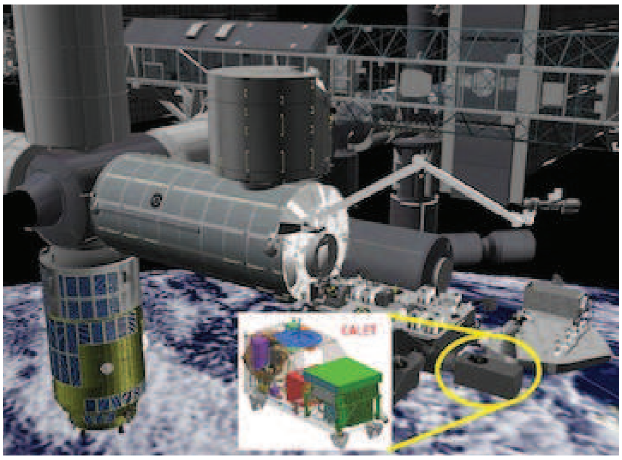

Figure 2.1: *An artist's view of the CALET payload on the Exposed Facility of the Japanese Experiment Module.*

2.1 CALET Apparatus

CALET [38] is an all-calorimetric instrument launched on August 19, 2015 from the Tenegashima Space Center with the Japanese HII-B launch carrier. CALET reached the ISS on August 24 on board of the transfer vehicle HTV5 (Kounotori) and was emplaced on the port #9 of the Exposure Facility of the Japanese Experimental Module Kibo. The CALET detector on JEM-EF platform stands on a pallet, supporting the calorimeter with its subsystems (Fig. 2.1).

The power-on and on orbit commissioning procedures of the detector were started and data relayed to the ground stations, after an early period needed for degassing. In mid October 2015 the preliminary phase of on-orbit check-out and calibrations were accomplished. Since then, the instrument is operating in science mode and transmitting data to the ground stations.

The CALET payload is shown in Fig. 2.2. It includes scientific and auxiliary equipment for a total mass of $612.8\,kg$, dimensions of $1.9 \times 0.8 \times 1.0\,m^2$ and nominal power consumption of $507\,W$. The main scientific instruments are *the electromagnetic CALorimeter* (CAL) and *the Calet Gamma-ray Burst Monitor* (CGBM) plus the following main subsystem:

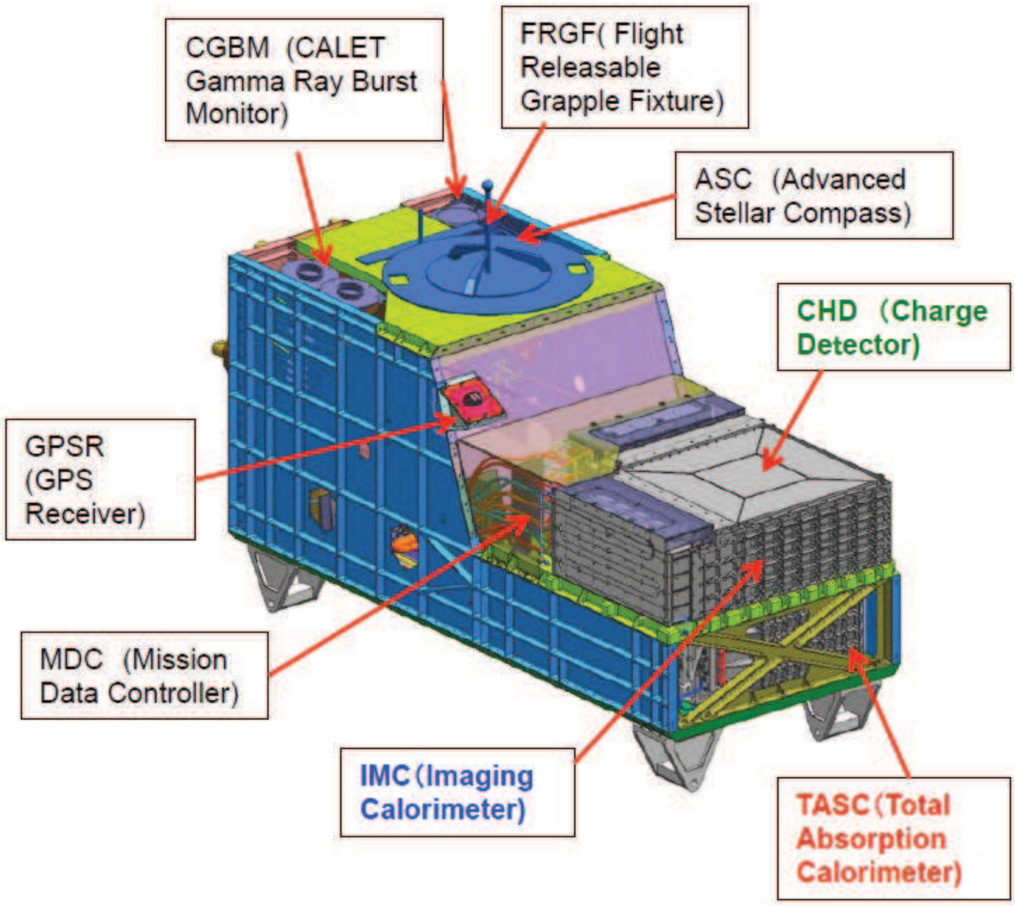

Figure 2.2: *The CALET pallet installments for the mission; it consists of the Main detector (CAL and CGBM) and Support equipments (GPSR, ASC, MDC, FRGF).*

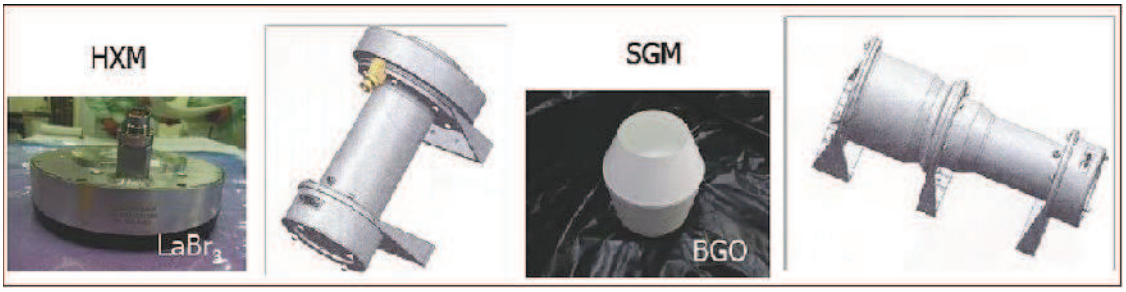

Figure 2.3: *The components of the CGBM.*

Flight Releasable Grapple Fixture (FRGF) provides grapple points for the robotic arm (and the astronauts);

Mission Data Controller (MDC) for detector systems management and data handling;

Advance Stellar Compass (ASC) and GPS receiver (GPSR) providing fine position and attitude data.

In the nexts sections a detailed description of the CGBM and of the CAL is reported.

2.1.1 The CALET gamma-ray burst monitor

The CGBM [39] is an ancillary scientific instrument which supports a capability for GRB observations by the CAL. It observes a lower energy range which the CAL can not cover and is aimed to obtain GRB spectra over a wide range from X-rays to gamma-rays. In addition to GRB observations, the CGBM carries out all sky observations of various gamma ray transients as soft gamma repeaters, solar flares, terrestrial gamma-ray flashes, and X-ray binaries. It is composed of three sensors and an electronics box (E-box) which processes the signal of sensors. The digitized data from the E-box output are formatted by the Mission Data Controller (MDC), and sent as a telemetry to the ground station at NASA.

The CGBM sensors, Fig. 2.3, are in total three detectors, two identical Hard X-ray Monitors (HXM) and one Soft Gamma-ray Monitor (SGM) to

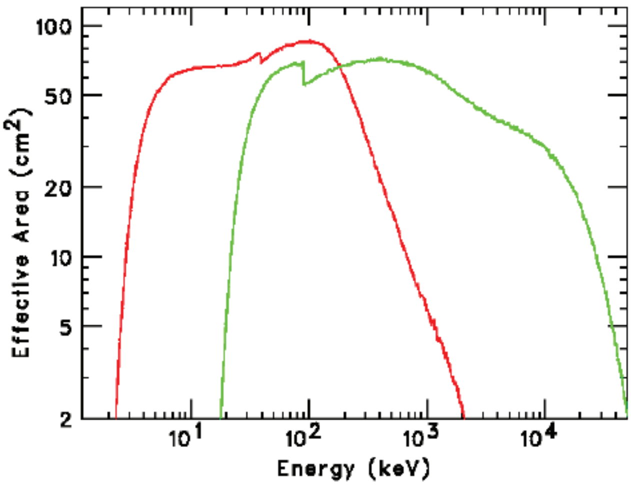

Figure 2.4: *Effective area of the CGBM HXM (shown in red) and SGM (green) [39].*

cover a wide energy range of $7\,keV$ to $20\,MeV$ by its combination. Each HXM is comprised of a two-layered scintillator of $LaBr_3(Ce)$ with excellent performance in terms of light yield, energy resolution, and time response in comparison with $NaI(Tl)$. Each of the two $LaBr_3(Ce)$ crystals is configured as two cylinders, the front cylinder with $66.0\,mm$ diameter and $6.35\,mm$ thick and the rear cylinder with $78.7\,mm$ diameter and $6.35\,mm$ thick. The beryllium entrance window with a $410\,mm$ thickness is used for soft X-ray detection below $10\,keV$. The SGM is made of a single BGO scintillator which has a high stopping power for gamma-rays due to its large density ($\rho = 7.13\,g/cm^3$) and effective atomic number ($Z_{eff} = 74$). The BGO crystal has a cylindrical shape with $102\,mm$ diameter and $76\,mm$ thickness.

Figure 2.4 shows the HXM and SGM effective area as a function of energy. The unique feature for the HXM is a sensitivity to soft X-rays below $10\,keV$. The HXM covers a lower energy range of $7 - 1000\,keV$, while the SGM covers a higher energy of $100\,keV - 20\,MeV$. Each sensor mainly contains a scintillation crystal, a photo-multiplier tube (PMT), a high voltage divider, and a charge sensitive amplifier (CSA). All the components are installed in an aluminum housing. The field of view for the HXM is limited by the light collimator within about 58° from the zenith to reduce possible contamination from the cosmic X-ray background and bright X-ray sources. This configuration allows a GRB detection rate of about 30-40 per year by the HXM.

2.1.2 The CALET Calorimeter

The main instrument of the mission is an all-calorimetric instrument, Fig. 2.5, designed to achieve a large proton rejection capability ($> 10^5$). It has a total thickness equivalent to 30 radiation length X_0 and 1.3 proton interaction length λ_I and a field of view of $\sim 45°$ from the zenith. The instrument is composed of three main subsystem: at the top a Charge Detector (CHD) identifies the individual chemical elements in the cosmic-ray flux, than a fine granulated pre-shower IMaging Calorimeter (IMC), followed by a Total Absorption Calorimeter (TASC) measure the energy released.

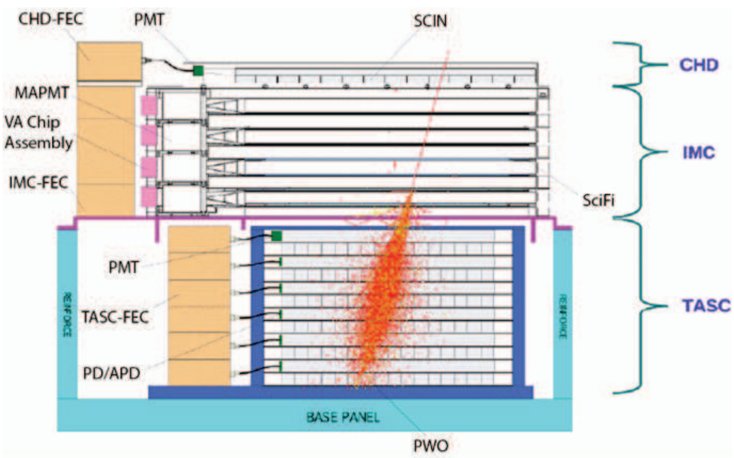

Figure 2.5: *A schematic side view of the main calorimeter. An example of a simulation event for a 1 TeV electron is superimposed to illustrate the shower development in the calorimeter.*

2.1.2.1 The Charge Detector

The CHD has been designed to measure the charge of incoming particles via the Z^2 dependence of the specific ionization loss. In this way it provides incident particle identification over a large dynamic range for charges in $Z = 1 \sim 40$. It consists of two crossed layers of plastic scintillators EJ204. Each layer consists of 14 scintillator paddles with dimensions $450\,mm(L)\times 32\,mm(W)\times 10\,mm(H)$. The paddle of the first (top) and of the second (bottom) layer are aligned along the Y and X directions, respectively. This segmented configuration has been optimized to reduce multi-hits on each paddle caused by backscattering particles. The generated scintillation light is collected and read out by a photomultiplier tube (PMT) Hamamatsu R11823, with a photo-cathode of $8\,mm$ diameter through an acrylic light guide (Fig. 2.6 (right)). The structural design of CHD is shown in Fig. 2.6 (left). The paddles are covered with Vikuiti ESR films (3M) in order to increase the light collection. The Front End Custom (FEC) of the CHD is almost the same as TASC-FEC [1], except that TASC-FEC employs dual range readout for each photo sensor to achieve a wide dynamic range, on the contrary CHD-FEC employs single readout.

2.1.2.2 The IMaging Calorimeter

Below the CHD, the IMC calorimeter images the early shower profile with a fine granularity by using $1\,mm$ square cross section scintillating fibers (SciFi) individually read out by Multi-Anode Photomultiplier Tubes.

The IMC consists of 7 layers of tungsten plates each separated by 2 layers of SciFi belts arranged in the X and Y direction and capped by an additional X,Y SciFi layer pair, for a total of 16 SciFi. Each SciFi belt is assembled with 448 fibers read out by a Hamamatsu R7600-M64 multi-anode photomultiplier tube shown in Fig. 2.7, together with two 8-fibers belts with their light guides and support system for the coupling with the PMT. Two con-

[1] See section 2.1.2.3.

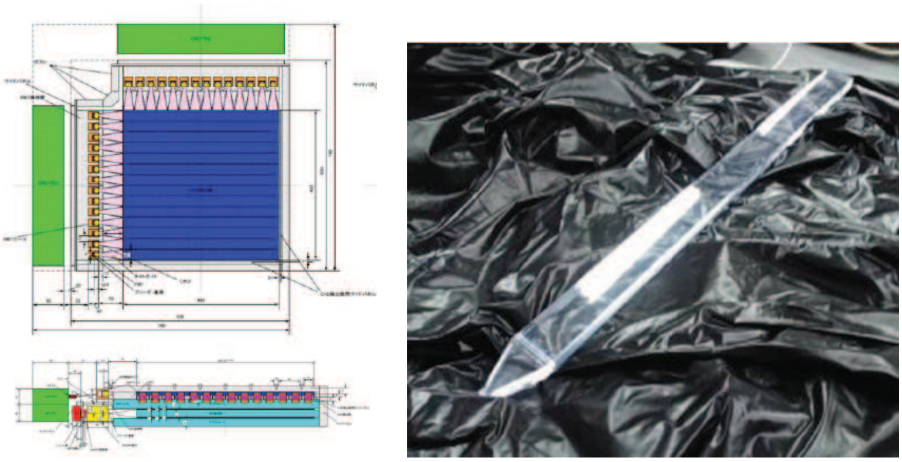

Figure 2.6: *Structural design of CALET-CHD (left), EJ204 scintillator and the acrylic light guide (right) [40].*

secutive X-Y pairs are spaced 2 cm apart by a honeycomb support structure, while the tungsten plates are placed directly on top of the SciFi pairs. This arrangement allows to get two independent transversal views of the shower development. The thickness of the tungsten layers increases with Z coordinate while, their areas become smaller and smaller, until it is equal to the top surface of the TASC detector. So, the IMC resulting shape is the one of a truncated pyramid in which the first three layers are 44.8 $cm(L) \times 44.8\, cm(W)$ and 0.07 cm thickness, the next two layers are 38.4 $cm(L) \times$ 38.4$cm(W)$ and 0.07 cm thickness and the last two layers are 32.0 $cm(L) \times$ 32.0 $cm(W)$ and 0.35 cm thickness. The total thickness of the IMC is equivalent to $3X_0$. The first five tungsten SciFi layers sample the shower every $0.2X_0$ and the last two layers provide $1.0X_0$ sampling.

The IMC is designed to act as a pre-shower, as electrons and γ-rays are likely to interact in the tungsten layers, generating an electromagnetic shower, while only a few protons and nuclei undergo an hadronic interaction, as the IMC depth is equivalent to only $0.11\lambda_0$. Moreover, IMC fine granularity allows to:

- *determine the starting point of the shower* in order to both separate electrons and positrons against the γ background, and for a more pre-

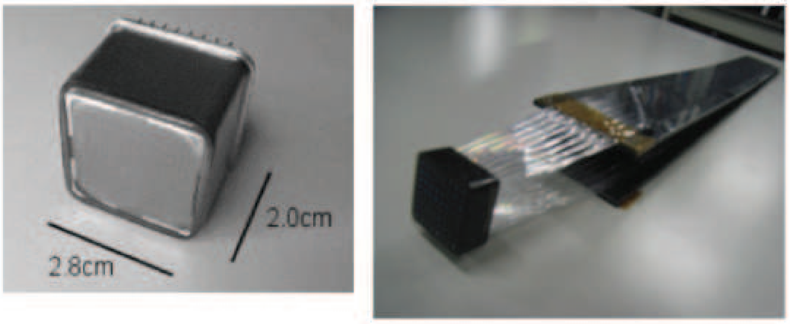

Figure 2.7: *The MA-PMT Hamamatsu R7600-M64 (left). The fiber belts with the system for the coupling with the MA-PMT(right).*

cise measurement of the hadronic particles energy;

- *reconstruct the incident particle trajectory;*
- *separate the incident particles from backscattered particles;*
- *provide a redundant measurement of the particle charge* in order to get a better identification of the different nuclear species.

An accurate study of the IMC detector performances can be found in [41].

2.1.2.3 The Total AbSorption Calorimeter

The TASC is an homogeneous calorimeter designed to measure the total energy of the incident particle and discriminate the electromagnetic from hadronic showers.

It is composed of 12 layers, each consisting of 16 lead tungstate (PWO) logs. Each log has dimensions of $326\,mm(L) \times 19\,mm(W) \times 20\,mm(H)$. Layers are alternately arranged with the logs oriented along orthogonal directions to provide a 3D reconstruction of the showers. Six layers image the X-Z view and the other six the Y-Z view. The total area of the TASC is $326 \times 326\,mm^2$ and the total thickness corresponds to about $27X_0$ and $1.2\lambda_0$ at normal incidence.

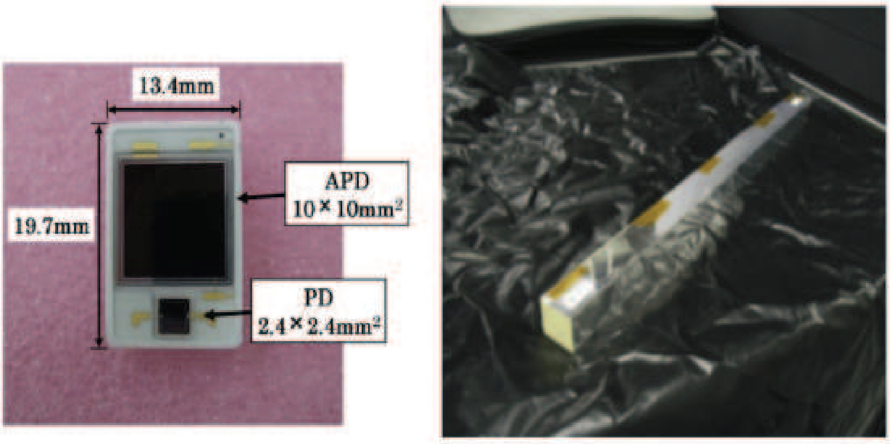

Figure 2.8: *APD Hamamatsu S8664-1010, active area of* $10\,mm \times 10\,mm$*, and PD S1227-33BR of* $2.4\,mm \times 2.4\,mm$ *(left) [42]. A picture of one of the lead-tungstate logs of the TASC (right).*

Each PWO log at the top layer (nearest to the IMC) is readout by the PMT to generate a trigger signal, while hybrid packages of silicon Avalanche PhotoDiode and silicon PhotoDiode (Dual APD-PD) are used to detect photons from all of the remaining PWO bars in the eleven layers. The dual APD-PD package is shown in Fig. 2.8 (left), together with the picture of one of the lead-tungstate logs of the TASC (Fig. 2.8 (right)). The readout front end system of each pair of the APD-PD sensors is configured with Charge Sensitive Amplifier (CSA) and pulse shaping amplifier with dual gain. A block diagram of the Front-end circuit for the CALET-TASC is shown in Fig. 2.9. Signals from each photodiode are amplified by the CSA with an high dynamic range of 4 orders of magnitude. Two shaping amplifier circuits with different gains are provided for signal processing with each CSA. Each shaping amplifier has two sections for each input channel with a gain ratio of 30:1, each getting digitized by a 16-bit A/D Converter. Such a readout system provides a dynamic range covering nearly six orders of magnitudes and allows to measure in each bar signal spanning from $0.5\,MIPs$ ($Minimum\,Ionizing\,Particles$) to $10^6\,MIPs$, which is the energy deposit expected from a proton-induced 1000 TeV shower [42]. In fact the main scientific objective of CALET is the

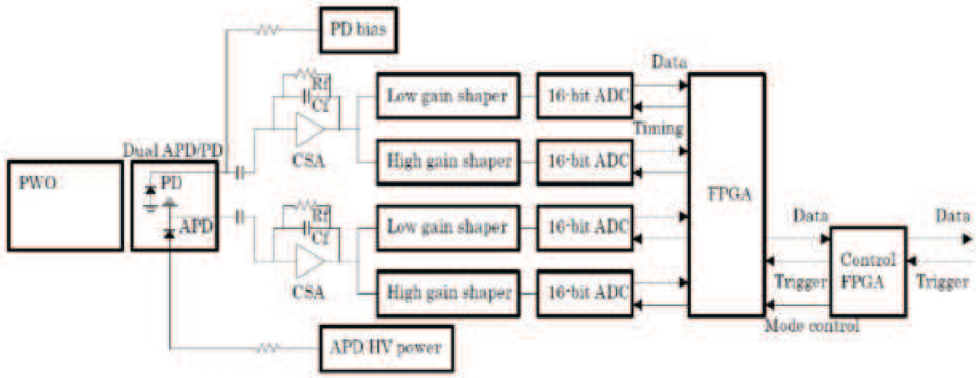

Figure 2.9: *Block diagram representation of the Front-End Circuit for the TASC read-out [42].*

measurement of the electron spectrum over the range from 1 GeV to 20 TeV. For this purpose, TASC is required to have a linear energy response from GeV up to the TeV region and an excellent resolution to resolve possible spectral features as expected in case of the presence of nearby CR sources or dark matter.

Furthermore, another necessary requirement is to efficiently identify high-energy electrons among the overwhelming background of CR protons. Particle identification information from both IMC and TASC is used to achieve an electron detection efficiency above 80% and a proton rejection power $\sim 10^5$.

2.2 Calet Performance

In this section are reported the performance of CALET to take data under different energy conditions and to identify interestings events.

2.2.1 Trigger system

The CALET trigger [43] is generated by the coincidence of the discriminated analog signals from different detector components i.e., each of CHD X and Y, IMC X1-X4, Y1-Y4, and TASC X1 lower discriminator (LD) signals with specific threshold settings Fig. 2.10. Since CALET takes data on wide range of energy, it features three primary trigger modes to take data under different conditions efficiently, as described in the following. In addition the Heavy Ion Trigger mode can be selected in combination with each primary trigger mode.

1. **High Energy Shower Trigger (HE)** This is the main trigger mode for CALET because it targets high energy electrons of $10\,GeV-20\,TeV$, high energy gamma-rays of $10\,GeV - 10\,TeV$, and protons and nuclei of a few $10\,GeV - 1000\,TeV$. It is based on the signals from the top layer of the TASC and the sum of signals from the IMC X4 and Y4 layers.

   By requiring a large energy deposit in the middle of the detector, high energy shower events are selectively triggered. As a result, it is possible maximize the exposure for the selected particles while strongly suppressing low energy particles and achieving a large solid angle acceptance at the same time.

2. **Low Energy Shower Trigger (LE)** The primary targets of the LE trigger are low energy electrons of $1\,GeV - 10\,GeV$ at high latitude (where the geomagnetic rigidity cut-off is lower than $2\,GV$) and GRB gamma rays of $> 1\,GeV$. To trigger electrons at high latitude, LD signals are required at CHD and IMC upper layers to restrict the incident

Trigger Mode	CHD X CHD Y [MIP]	IDyn X1 IDyn Y1 [MIP]	IDyn X2 IDyn Y2 [MIP]	IDyn X3 IDyn Y3 [MIP]	IDyn X4 IDyn Y4 [MIP]	TASC X1 [MIP]
HE	- -	- -	- -	- -	7.5 7.5	55
LE	0.7 0.7	0.7 0.7	0.7 0.7	0.7 0.7	2.5 2.5	7
Single	0.7 0.7	0.7 0.7	0.7 0.7	0.7 0.7	0.7 0.7	0.7
Heavy HE	50.0 50.0	- -	- -	- -	7.5 7.5	55
Heavy LE	50.0 50.0	0.7 0.7	0.7 0.7	0.7 0.7	2.5 2.5	7
Heavy Single	50.0 50.0	0.7 0.7	0.7 0.7	0.7 0.7	0.7 0.7	0.7

Figure 2.10: *CALET trigger mode with LD threshold.'-' indicates that the corresponding LD signal is not required for the trigger.*

angle of the particles. The energy deposit required in the middle of the detector is much lower than for the HE trigger, but it is significantly higher than that of MIP.

3. **Single Trigger (Single)** This trigger mode is dedicated to taking data of non-interacting particles for the detector calibration. All trigger sources are used and each threshold is set to a suitable value to detect one MIP signal.

Heavy Ion Trigger (Heavy) This is the trigger mode to collect heavy nuclei with charge > 2, it requires larger energy deposits in the CHD. Heavy mode is defined for each of normal HE, LE and Single trigger, resulting in six independent trigger modes. What distinguishes heavy modes from normal modes are the LD thresholds and LD-masks for the CHD only.

For the sake of completeness, a logic diagram of the trigger decision and data acquisition request for CALET is shown in Fig. 2.11.

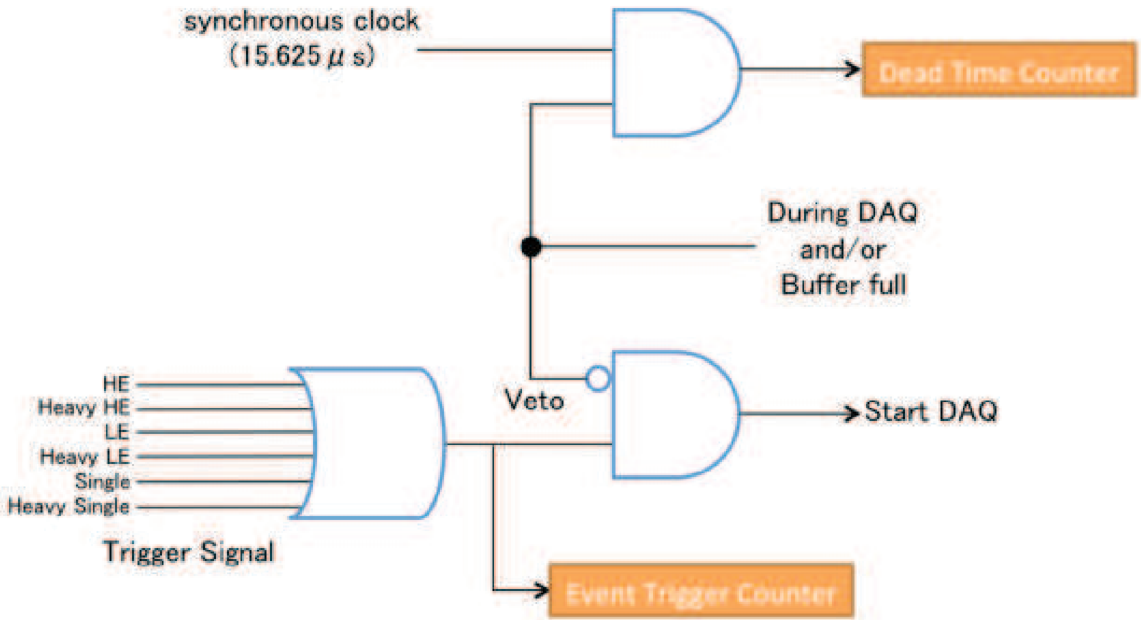

Figure 2.11: *Diagram of the CALET trigger and data acquisition request logic [43]*

2.2.2 CALET acceptances and geometrical factors

In CALET are defined four acceptances categories to identify interestings events. Each acceptance has specific topological requirements according to Tab. 2.1. The geometrical factor $S\Omega$ can be calculated for each acceptance category, using the MC simulation based on the CAD model, according to the following equation [44],

$$S\Omega = \frac{N_{sel}}{N_0} S_0\Omega_0 \tag{2.2.1}$$

where N_0 is the total number of generated events, N_{sel} is the number of events inside the acceptance and $S_0\Omega_0$ is the geometrical factor of the generation surface for the simulation, with S_0 the area of the generation surface and Ω_0 the solid angle.

In the following the four acceptances categories are described.

- **type 1 acceptance:** The incident particle direction crosses CHDX and CHDY layers, the top and bottom TASC layers, and is well contained within a fiducial volume in the TASC (defined by excluding in each layer the calorimeter crystals logs at the TASC edges). The geometrical factor is $S\Omega = 415.7\, cm^2 sr$.

- **type 2 acceptance:** The incident particle direction crosses CHDX and CHDY layers, the top and bottom TASC layers, but it is outside the TASC fiducial volume. The geometrical factor is $S\Omega = 154.6\, cm^2 sr$.

- **type 3 acceptance:** The incident particle direction crosses the 5th IMC layer, the top and bottom TASC layers, but does not crosses CHDX and CHDY layers. The geometrical factor is $S\Omega = 230.1\, cm^2 sr$.

- **type 4 acceptance:** The incident particle direction crosses the 5th IMC layer, the top TASC layer but does not cross the bottom one. In addition the path lengh in the TASC must be longer than thickness of the TASC at normal incidence, because a too short path in the TASC would preclude a precise energy determination. The geometrical factor is $S\Omega = 236.4\, cm^2 sr$.

Table 2.1: *The CALET acceptances categories. The total geometrical factor for CALET instrument is* $1036.6\,cm^2 sr$. L_{TASC} *is the path length in the TASC; the size of the TASC box are* $32.53\,cm(X) \times 32.53\,cm(Y) \times 26.42\,cm(Z)$.

-	Condition	Config.	$S\Omega[cm^2 sr]$
1	CHD-X-top &&CHD-Y-top &&TASC-top (inside 1 log) &&TASC-bot (inside 1 log)	$-44.969 \times 45.0 cm^2 @ z = 0.7005 cm$ $-45.0 \times 44.969 cm^2 @ z = 1.8535 cm$ $-28.446 \times 28.446 cm^2 @ z = 24.927 cm$ $-28.446 \times 28.446 cm^2 @ z = 51.347 cm$	415.7
2	CHD-X-top &&CHD-Y-top &&TASC-top &&TASC-bot &&![TASC-top (inside 1log) && TASC-bot (inside 1log)]	$-44.969 \times 45.0 cm^2 @ z = 0.7005 cm$ $-45.0 \times 44.969 cm^2 @ z = 1.8535 cm$ $-(32.53 \times 32.6 cm^2) - (28.446 \times 28.446 cm^2) @ z = 24.927 cm$ $-(32.6 \times 32.53 cm^2) - (28.446 \times 28.446 cm^2) @ z = 51.347 cm$	154.6
3	IMC5th layer &&TASC-top &&TASC-bot &&![CHDX-top &&CHDY-top]	$-44.796 \times 44.796 cm^2 @ z = 14.247 cm$ $-32.53 \times 32.6 cm^2 @ z = 24.927 cm$ $-32.6 \times 32.53 cm^2 @ z = 51.347 cm$ $-!(44.969 \times 45.0 cm^2) @ z = 0.7005 cm$ $-!(45.0 \times 44.969 cm^2) @ z = 1.8535 cm$	230.1
4	IMC5th layer &&TASC-top &&TASC-*path length* > TASC-*thickness* &&!TASC-bot	$-44.796 \times 44.796 cm^2 @ z = 14.247 cm$ $-32.53 \times 32.6 cm^2 @ z = 24.927 cm$ $-L_{TASC} > 26.42 cm$ $-!(36.6 \times 32.53 cm^2) @ z = 51.347 cm$	236.4

2.3 CALET Main Science Goals

The most important scientific objectives in cosmic-ray physics are to clarify the origin, the acceleration mechanisms, and the propagation properties of cosmic rays. The nature and origin of the dark matter is also one of the most important unresolved problems in astrophysics.

The CALET telescope is carring out perform precise measurements of high energy cosmic rays, with an extensive physics program that includes the detection of possible nearby sources of high energy electrons; searches for signatures of dark matter in the spectra of electrons and γ-rays; long exposure observations of cosmic nuclei from proton to iron and trans-iron elements; measurements of the CR relative abundances and secondary-to-primary ratios; studies of gamma-ray transients and solar modulation.

In the following, a brief description of the main scientific goals of CALET is presented.

2.3.1 Electron observations

The primary science goal of CALET is to perform high precision measurements of the electron spectrum from 1 GeV to 20 TeV. Electrons have unique features because of their low mass and leptonic nature. High-energy electrons lose energy via synchrotron and inverse Compton processes during propagation in the Galaxy. Since the energy loss rates almost increase directly with the square of the electron energy, higher energy electrons lose their energy more rapidly. So, TeV electrons lose most of their energy on a time scale of $10^5 yr$, and their propagation distances are therefore limited to $1\,kpc$. Evidence of non-thermal X-ray emission and TeV γ-rays from supernova remnants suggest that high energy cosmic ray electrons are presumably accelerated in SNRs. Since the number of potential sources satisfying the above constraints are very limited, the energy spectrum of electrons might have a distinctive structure and the arrival directions are expected to show a detectable anisotropy. From information on the ages and distances of the ob-

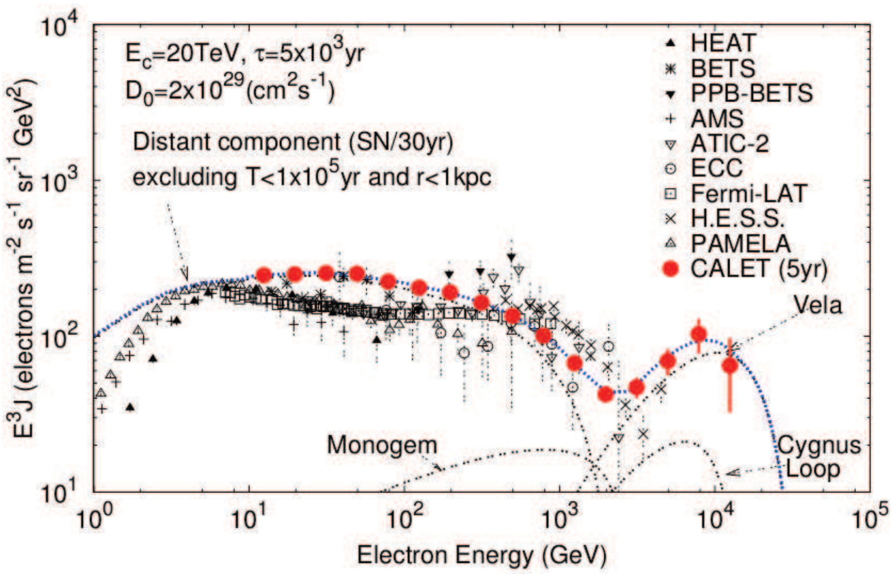

Figure 2.12: *Simulated electron energy spectrum of the CALET for 5 years observations (red point) from a SNR scenario model (blue line), compared to the previous electron measurements (Yoshida et al, 2011 [46]).*

served SNRs, one can determine theoretically which sources could contribute to electrons most efficiently in a given energy range. Nearby SNRs such as Vela, Cygnus Loop, or Monogem, could leave unique signatures, in the form of identifiable structures in the energy spectrum of TeV electrons, and measurable footprints in the dipolar asymmetry (Kobayashi et al, 2004 [45]). The expected electronic spectrum, in the case of one of Kobayashi's parametrizations[2], is represented in Fig. 2.12 by the blue dotted line [45]. In the same figure is shown the expected electron spectrum from CALET (red points) above 1 TeV in 5 years of observations [46]. As can be seen from the figure, CALET has a capability to identify the unique signature from nearby SNRs, especially originating from the Vela SNR, in the energy spectrum. This might provide the first experimental evidence for the presence of one (or more)

[2] For the calculation the parameters include a diffusion coefficient $D_0 = 2 \times 10^{29} cm^2/s$ a 1 TeV, a cut-off energy of $E_c = 20\,TeV$ for the electron source spectrum, and a burst-like release at $\tau = 5 \times 10^3 yr$ after the supernova explosion [45].

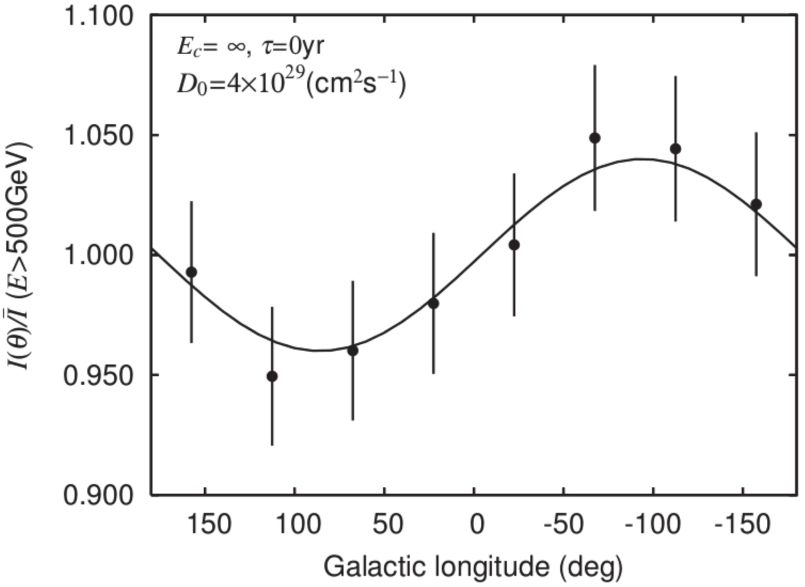

Figure 2.13: *The expected results for Vela anisotropy measurement in the TeV region, and for a 5 year observation period with CALET [46].*

nearby source of electron acceleration at very high energies. The degree of anisotropy of high-energy cosmic electrons is shown in Fig. 2.13, where the electron intensity distribution along the Galactic longitude is plotted [3]. As can be seen from the figure CALET is expected to have the capability to observe a possible anisotropy in the direction of a nearby SNR.

However, the TeV region might as well conceal a completely different scenario where nearby acceleration sources would not be detected and the spectrum might show at a characteristic cut-off energy. In this case, the measurement of the *end-point* of the electron spectrum could be used to constrain the cosmic-ray diffusion coefficient.

The electron energy spectrum from $10\,GeV$ to $1\,TeV$ could be the result of the contribution of several unresolved sources. The hardening of the inclusive electron+positron spectrum in the range $200\,GeV - 1\,TeV$ could be interpreted as the result of the annihilation/decay of dark matter particles or

[3] For the calculation swere used a diffusion coefficient $D_0 = 4 \times 10^{29} cm^2/s$ a 1 TeV, a cut-off energy of $E_c = \infty$ for the prompt release after the supernova explosion ($\tau = 0$) [45].

particles coming from astrophysical objects (e.g. a nearby pulsar) (Motz et al, 2015 [47]). Furthermore, to explain the rise of the positron fraction above $\sim 10\,GeV$ as measured by PAMELA (Adriani et al, 2013 [48]) and extended to the hundreds GeV region by AMS-02 (Aguilar et al, 2013 [49]) requires the presence of an additional spectral component. In this energy region CALET will provide information on the features of the source spectrum, the diffusion time, the density and the nature of sources by the detailed spectral shape and angular distribution of the inclusive spectrum.

2.3.2 Dark Matter searches

In astrophysics, Dark Matter (DM) is an unknown form of matter, which undergoes in gravitational interaction, but does not emit nor absorb electromagnetic radiation.

Dark matter was first postulated in 1932 by the Dutch astronomer Jan Oort, who noted that the orbital velocities v of stars in the Milky Way do not match with their measured masses. The observed mass M_0 was less than the theoretic mass $\frac{M_r G}{r^2} = \frac{v^2}{r}$, and the difference $M_0 - M_r$ was attributed to the presence of dark matter. The phenomenon was also pointed out by Fritz Zwicky in 1933 for the missing mass in the orbital velocities of galaxies in clusters. Subsequently, other observations have manifested the existence of dark matter in the Universe, including the rotational velocities of galaxies, gravitational lensing, and the temperature distribution of hot gas.

From the Big Bang model, the measurements of light nuclei produced in primordial nucleosynthesis, and the study of the cosmic microwave background (CMB) radiation, it is estimated that baryons constitute only about 4 % of the total mass-energy density. The remaining content of the Universe is is supposed to be made of Dark Energy (73%) and Dark matter (23%). The existence of dark matter does not find an explanation in the framework of the Standard Model (SM) of particle physics. For this reason a wide variety of SM extensions have been hypothesized, leading to a proliferation of DM candidates. The only major non-particle candidate for dark matter is the primordial black hole, which would have collapsed directly from highly over-dense regions of the early Universe (B. Carr et al.,2010 [50]). The top-tier candidates are particles called *natural* dark-matter candidates because they are inspired by theories that solve other deep problems in physics. Among the latter there are Weakly-Interacting Massive Particles (WIMPs). This particle class interacts with typical weak-force interactions and it has masses near the weak scale, $\sim 100GeV$. Candidates include the supersymmetric neutralino (the lowest-mass eigenstate of the supersymmetric partners of neutral Standard Model gauge bosons) and the Kaluza-Klein (KK) photon (H. Cheng et al., 2002 [51]; G. Servant et al., 2003 [52]). Both candidates emerge out of theories to introduce new physics at the electroweak breaking scale (the minimal supersymmetric standard model [MSSM] and universal extra dimensions [UED]), and possibly to explain why that scale is so much lower than the Planck scale. Other particles in these theories could be dark matter if they were the lightest of the new particles (satisfying cosmological and collider constraints), but the neutralino and Kaluza-Klein UED photon are typically the lightest stable new particles.

CALET is carrying out a sensitive search of DM candidates in the inclusive electron spectrum and in gamma-ray spectra. Both neutralinos and KK particles can annihilate and produce an excess of positrons and electrons observable at Earth. However, only KK particle can annihilate directly into e, μ and τ[4], so that the electron signal for KK is enhanced with respect to that from neutralinos. Moreover, the direct annihilation provides a mono-energetic electrons and positrons which would create a specific and well detectable spectral feature. That is a sharp edge in the cosmic e^+ e^- spectrum (Fig. 2.14) at an energy equal to the particle mass, (typically several 100 GeV to 1 TeV). In Fig. 2.14, a simulated electron and positron spectrum by CALET observations for 2 years with Kaluza-Klein dark matter annihilations, for 620GeV mass and the boost factor of 40 is shown; the simulated spectrum is superimposed on the galactic background spectrum

[4]The annihilation is chirality suppressed for neutralinos and not for KK particles.

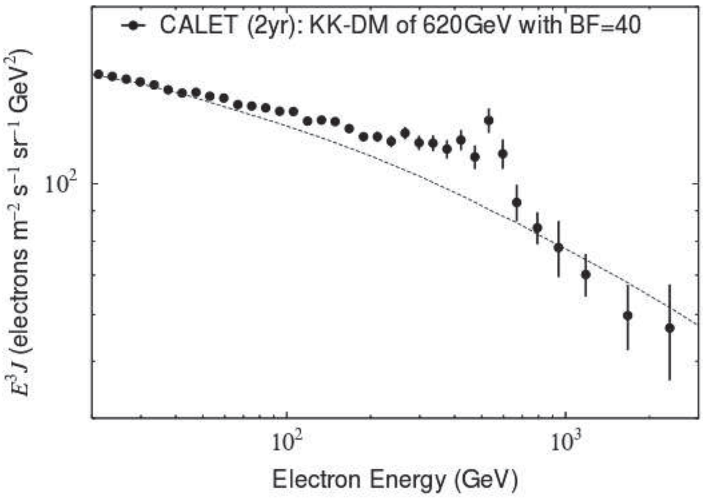

Figure 2.14: *Simulated energy spectrum of from e^+ e^- Kaluza-Klein dark matter annihilation with a 620 GeV mass and a boost factor of 40 for 2 years observations with CALET [46].*

(dashed line). From the figure one can see that CALET has the potential to detect an excess from dark matter annihilation in the energy spectrum.

Another hypothesis is that KK particles are unstable and can decay with a lifetime much longer than the age of the universe [53]: if leptons are produced from decaying DM particles with a lifetime around $10^{26}s$, in the channel $DM \to l^+l^-\nu$ the observed excesses in electron and positron spectra can be explained. Fig. 2.15 presents the expected energy spectrum of electrons and positrons from decaying dark matter.

DM can also decay into gamma rays or interact with interstellar and intergalactic photons to give gamma rays from inverse Compton scattering from $e^+ + e^-$ [53]. In Fig. 2.16 is shown the expected extragalactic gamma ray spectrum from decaying dark matter, including inverse Compton scattering gamma rays (lower energy components) and an isotropic extra-galactic back-ground (a power-law spectrum), with the same parameters as Fig. 2.15.

In case of DM composed by neutralino, the annihilation could be seen as a spectral line in the high energy gamma-ray spectrum. An example of the simulated energy spectrum of monochromatic gamma rays of 820 GeV from

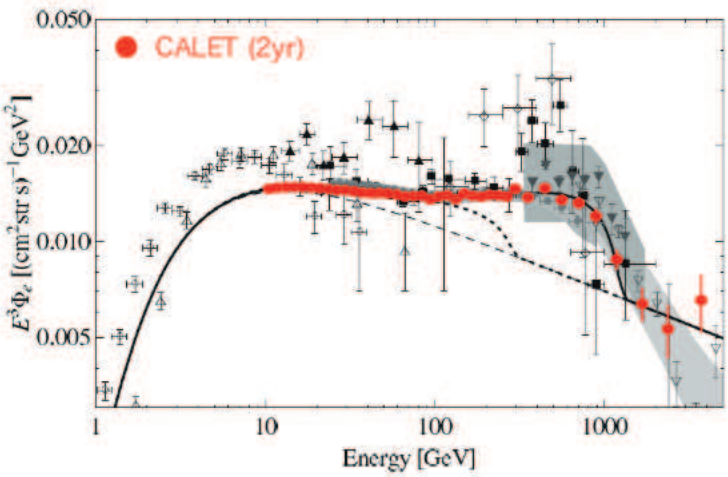

Figure 2.15: *Simulated energy spectrum of $e^+ + e^-$ from decaying dark matter for a decay channel of $DM \to l^+l^-\nu$ with the mass of $2.5\,TeV$ and the decay time of $10^{26}s$, for 2 years observations with CALET [46].*

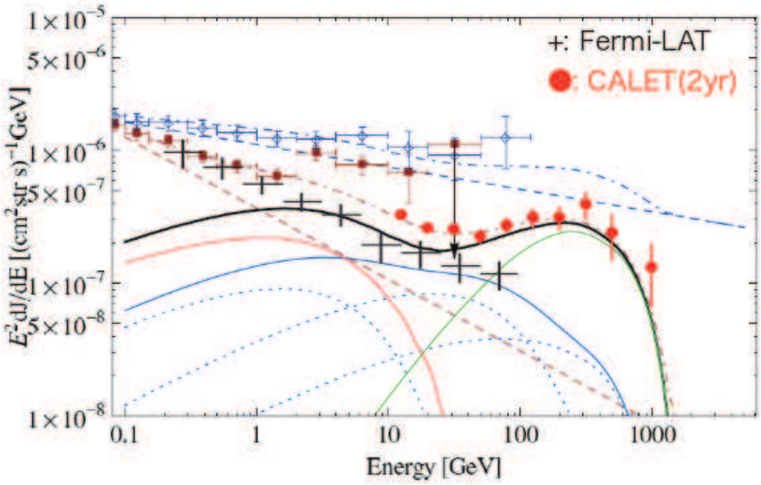

Figure 2.16: *Simulated energy spectrum of the extra-galactic diffuse gamma rays from decaying dark matter, including inverse Compton scattering gamma-ray spectra and an isotropic extra-galactic background [46].*

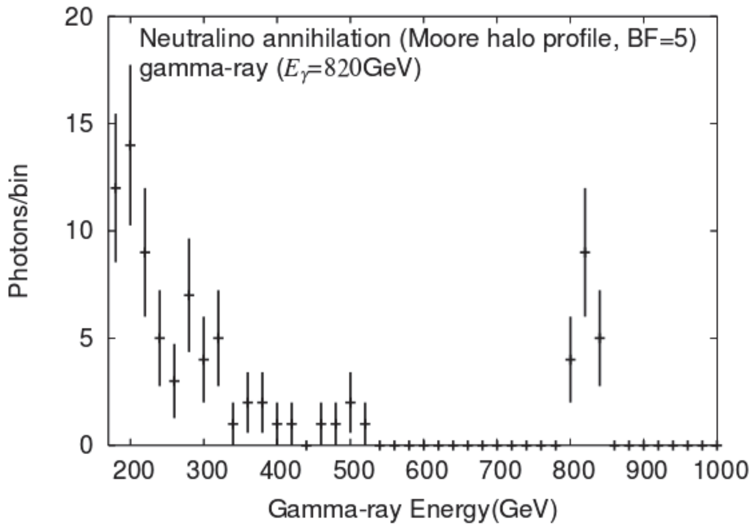

Figure 2.17: *Simulated energy spectrum of a gamma-ray line at* 820 *GeV from neutralino annihilation toward the Galactic center including the Galactic diffuse background for 2 years observations with CALET [46].*

neutralino annihilation, assuming a Moore halo profile with a boost factor of 5 [54], is shown in Fig. 2.17.

As one can see in the figure, CALET is an ideal detector to observe monochromatic gamma rays from dark matter annihilations in the several 10 *GeV* - several TeV region, thanks to its excellent energy resolution ($\sim 2\%$).

2.3.3 Gamma ray observations

Observation of gamma-ray sources are not a primary objective for CALET. However, its excellent energy resolution and good angular resolution (better than $0.4°$, including pointing uncertainty) allows for accurate measurements of diffuse gamma-ray emission and detection of more than one hundred bright sources at high latitude from the Fermi-LAT catalogue. Moreover, the line of sight of the CALET in the opposite direction with respect to the Earth, provides an unique opportunity to observe gamma-ray sources with an exposure of several ten days per year for point source. Fig. 2.18 shows the simplified sky map simulation of gamma rays above 10 GeV with CALET for 3 years

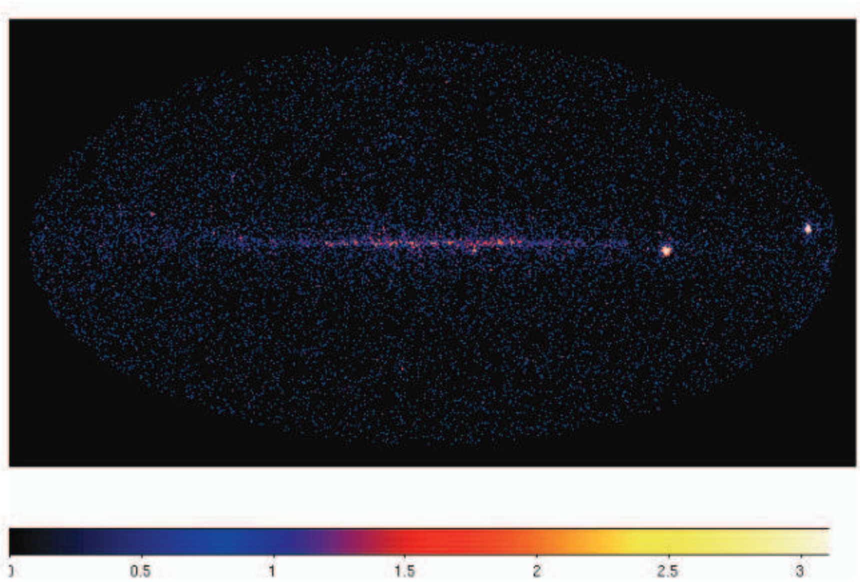

Figure 2.18: *Simulated sky map of gamma rays above 10 GeV with CALET for 3 years observations [46].*

observations. Given the on-axis effective area of $\sim 600\,cm^2$ for energies above $10\,GeV$ (reduced by $\sim 50\%\,at\,4\,GeV$) and field of view of 45° from the vertical direction, CALET is expected to detect $\sim 2.5 \times 10^2$ (~ 7000) photons from the galactic (extra-galactic) background with $E > 4\,GeV$ and ~ 300 photons from the Vela pulsar with $E > 5\,GeV$ [55].

Due to the wide field of view, CALET has also an excellent capability to detect Gamma-Ray Bursts (GRB). The GRB is one of the most energetic events in the universe, with a radiated energy release of $> 10^{51} erg$. For prompt emissions, most of the energies are emitted in an energy range from soft X-rays to GeV gamma-rays. CALET will also monitor X-ray - gamma-ray transients in the energy region from $7\,keV$ to $20\,MeV$ with a dedicated Gamma-ray Burst Monitor. It will extend GRB studies carried out by other experiments (e.g. Swift and Fermi/LAT) and provide added exposure when the other instruments will not be available or pointing to a different direction. Furthermore, high energy photons possibly associated with a burst event can be recorded over the entire CALET energy range down to 1 GeV where the CALET main telescope has still (limited) sensitivity, albeit with low resolution. Upon the detection of a GRB, an alert will be transmitted to a network of ground antennas (including LIGO and VIRGO) for the possible simultaneous detection of gravitational waves associated with the event.

2.3.4 Cosmic-ray spectra

CALET will perform long term observations of light and heavy cosmic nuclei from proton to iron and will also detect trans-iron elements up to $Z \sim 40$. It will be able to identify the most abundant CR elements with individual element resolution and measure their spectral shape and relative abundance in the energy range from a few tens of GeV to the PeV . The first objective is to investigate the intermediate energy region from $200\,GeV/n$ to $800\,GeV/n$ where a deviation from a single power-law, related to a changes in the diffusive propagation mechanisms [56], has been reported for both proton and helium spectra by CREAM [57] and PAMELA [58] and recently confirmed by AMS-02 [59]. CALET will carry out an accurate scan of this energy region to verify the presence of a progressive hardening of the spectrum by measuring its curvature and spectral break point position. In a relatively short time, CALET will be able to close the gap between the AMS-02 highest energy points and CREAM lowest points for proton and He. In five years of data taking on the ISS, CALET will extend the proton energy spectrum up to $\sim 900\,TeV$, the He spectrum up to $400\,TeV/n$ (Fig. 2.19) and measure the energy spectra of the most abundant heavy primary nuclei C, O, Ne, Mg, Si and Fe with sufficient statistical precision up to $\sim 20\,TeV/n$ (Fig. 2.20). The extension of direct measurement of CR nuclei spectra to unprecedented energies is of fundamental importance in order to investigate the presence of possible charge dependent spectral cut-offs at high energies, that are hypothesized to explain the CR *knee* (E. Berezhko et al., 1999 [60]).

Information about CR propagation might be obtained by directly measuring the secondary-to-primary flux ratios. Infact, as seen in Chap.1, cos-

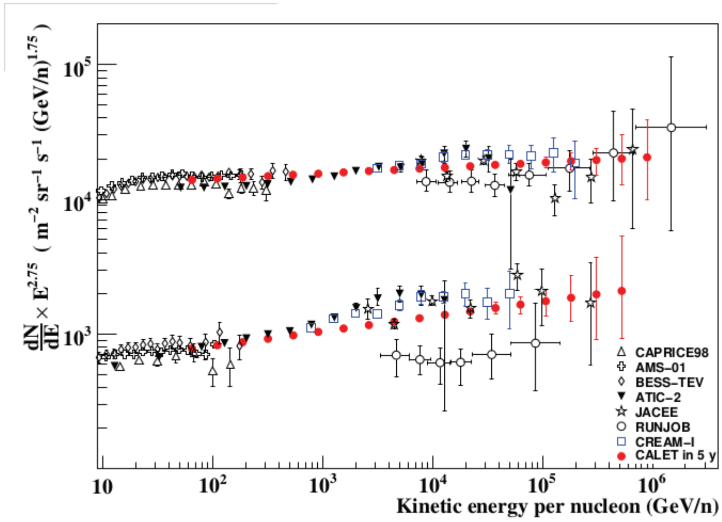

Figure 2.19: *Expected CALET measurement of the energy spectra of proton and He after 5 years of observation, compared with previous data (P. Maestro, 2013 [61])*

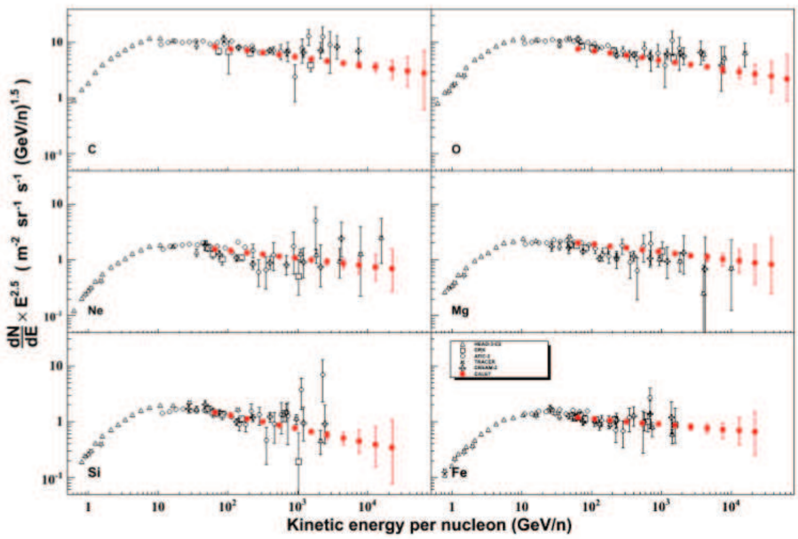

Figure 2.20: *Expected CALET measurement of the energy spectra of the more abundant heavy nuclei after 5 years of observation, compared with previous data [61].*

mic rays of primary origin interact with the interstellar medium to produce secondary fragments; the relative abundances of CR secondary-to-primary elements are known to decrease, following a power law in energy $E^{-\delta}$, where δ is a key parameter in the description of the CR diffusion in the Galaxy at high energies (see 1.3.4). So from measurements of the energy dependence of the flux ratio one can discriminate among different models of CR propagation in the galaxy. The Boron-Carbon ratio is one of the most sensitive quantity to test models, as B is purely secondary and its main progenitors C and O are primaries. Furthermore, the ratio of two nuclei with similar charge, it is less sensitive to systematic errors and to solar modulation than single fluxes or other ratios of nuclei with more distant charge values. Unfortunately, the available measurements, pushed to the highest energies with Long Duration Balloon experiments, suffer from statistical limitations and large systematic errors at several TeV/n, due to the residual atmosphere at balloon altitude. This sets an effective limit to the highest energy points of the secondary-to-primary ratios obtainable with measurements on balloons and has not allowed so far to place a stringent experimental constraint on the value of δ. On the contrary, space experiments like CALET are free from this limitation. With a long exposure and in the absence of atmosphere, CALET can provide new data to improve the accuracy of the present measurements of the B/C ratio above 100 GeV/n and extend them beyond 1 TeV/n, as illustrated in Fig. 2.21 [62].

CALET can also carry out measurements of the relative abundances of the Ultra-Heavy (UH) CR. Infact, the CHD has the charge resolution and dynamic range needed to measure Galactic cosmic-ray (GCR) nuclei up to charge $Z = 40$. But, if on the one hand CALET will measure the energy spectra of the more abundant nuclei with $Z < 28$ together with the track and energy reconstruction from the IMC and TASC, on the other hand, for the rarer UH nuclei $Z > 30$ the statistics collected requiring full passage through the CAL is limited, the requirement is limited only to the passage through the CHD and top IMC layers with a $600\,MeV/n$ threshold. This results

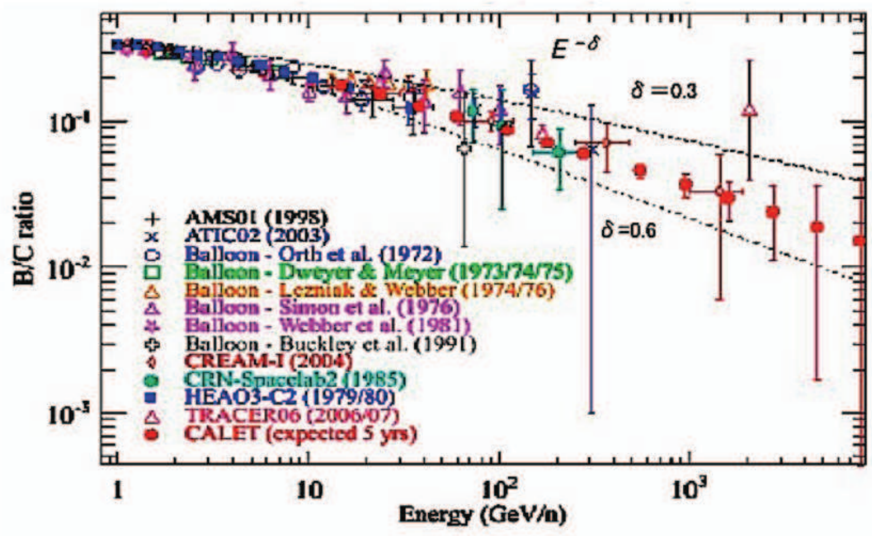

Figure 2.21: *Expected B/C ratio after 5 years of data taking with CALET comparing with previous experiments (P. Marrocchesi et al., 2013 [62]).*

into a large increase of the geometric acceptance factor from $\sim 0.07\, m^2 sr$ to about $0.44\, m^2 sr$ in the *UH mode*. The energy threshold can also be provided taking advantage of the Earth's magnetic field [63]. In fig. 2.22 the expected CALET event numbers over an anticipated 5 year mission are shown [63]. The left plot shows the expected CALET UH event numbers, for the UH (black) and full geometry (blue) measurement modes, compared with those measured by TIGER [64] (black points). The expected collected events for 1 year of data taking in the UH mode are shown (green line). The right plot shows the expected event numbers for the full acceptance over $4 < Z < 40$ for intermediate (black), maximum (red) and minimum (blue) solar modulations. In conclusion CALET is expected to measure ~ 10 times the UH events as TIGER with the UH mode, and ~ 4 times the UH statistics with the full geometry and energy reconstruction.

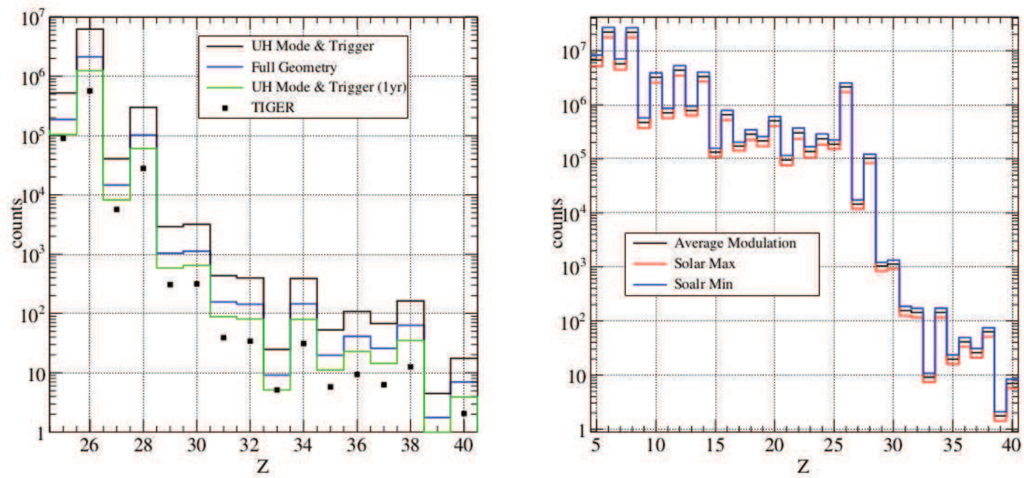

Figure 2.22: *Expected number of Heavy and Ultra-Heavy cosmic rays observed by CALET in 5 years of data taking (B. Rauch et al., 2015 [63]). Left: Predicted CALET UH GCR observations and comparison with the TIGER data. Right: Predicted CALET heavy and UH GCR for full instrument geometry and for different solar modulation hypotheses.*

Chapter 3

Calibration of the CALET Instrument

In order to reach the performances described in Chap. 2 , a careful calibration of each CALET detector, TASC, IMC and CHD is required. The calibration task requirements include evaluating the conversion factors between ADC units and energy deposits, ensuring linearity over each gain range, and providing a seamless transition between neighboring gain ranges. The method is well described in [65] for the TASC detector, but a similar methodology is applicable to the CHD and IMC, when equalizing and calibrating the energy deposit of each of their channels. The following work is focused in two aspects of the energy calibration process: the first one related to the energy position dependence correction in CHD, the second one to the correction for the quenching effect in the CHD and IMC.

3.1 Light attenuation in CHD scintillators

To fully calibrate each CHD paddles it is necessary to correct for the position dependence effects so as to equalize the response along the length of the scintillator. As described in Chap. 2, the measurement of the electric charge in the CHD involves plastic scintillator paddles coupled via a light guide to a photomultiplier. The light generated by an incident particle in a point along the paddle will be attenuated during its propagation before entering the light guide, showing as general an exponential dependence on the position x along the paddle with a long and short attenuation length components λ and λ_1 respectively, described by the expression

$$y(x) = a \cdot e^{-x/\lambda} + d \cdot e^{-x/\lambda_1}. \tag{3.1.1}$$

The first term is the trasmission for photons that have angles greater than or equal to the critical angle[1]. The attenuation length for this mode is around $1\,m$ and it is determined by absorption in the bulk and by the effective reflection coefficient at the interface. The second term is the trasmission for photons that have angles less than critical angle and it can be neglected. The attenuation length for this mode is around few centimeters. Consequently the response of each CHD paddle would be equalised according to Eq. (3.1.1).

In the following the CHD paddles response and their correction procedure are reported.

3.1.1 Data selection

For the following analysis the data from December 2015 to August 2016 are utilised after an appropriate selection. The selection consist in few points reported below:

Acceptance selection Events are selected according to Acceptance 1 and 2, described in Chap. 2.2.2, in order to discard particles that hit the CAL sideways.

Good Traking selection In order to determine which paddle have been hit from particle, only events that have a good track recostruction in IMC according to the Kalman Filter algorithm are selected.

After that, a selected sample of protons are used to correct the CHD response. It is important to note that the light attenuation does not depend on the incident particle kind, so in principle one could use any nucleus. The choice is due to the higher statistics available for protons.

[1]Critical angle is defined as $\vartheta_L = n_0/n$ where n is the refractive index of the medium.

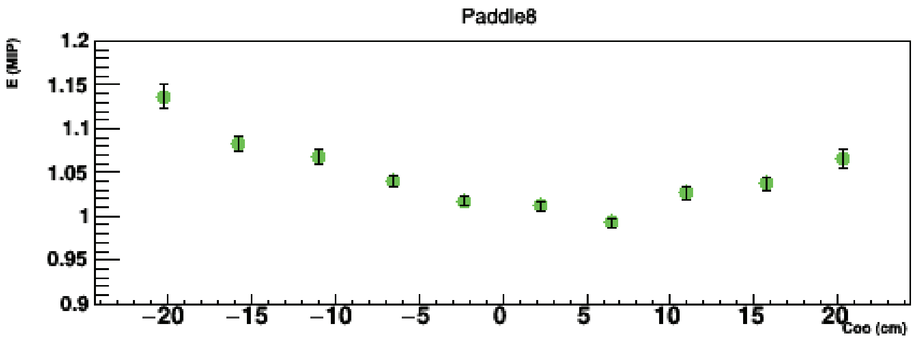

Figure 3.1: *Proton signal for CHDY layer: an example for paddle 8. The points represent the signal from each of the ten longitudinal segments the paddle is divided into. The CHD coordinate x is shown on the abscissa.*

3.1.2 Position dependence correction in CHD

In order to correct the CHD response, each paddle has been divided into ten segments and the signal has been measured for each of them. In Fig. 3.1 the proton signal for the eighth CHDY paddle as function of paddle coordinate is reported, as an example. As one can notice the signal does not decrease according to Eq. (3.1.1), but it reaches a maximum near the PMT, (paddle coordinate $\sim -20\,cm$), than it decreases to a minimum (around the center of the paddle, coordinate $\sim 0\,cm$), finally it slightly increases to a second maximum (end of paddle,$\sim 20\,cm$). The growth of the signal could be explained observing that a fraction β of the emitted light is reflected back to the photomultiplier adding to the direct light a second component according to the following formula:

$$y(x) = a \cdot e^{(-x-L/2)/\lambda} + b \cdot e^{(x-L/2)/\lambda}, \tag{3.1.2}$$

where $L = 45\,cm$ is the paddle length and $\beta = \frac{b}{a}$. In Fig. 3.2 the same plot of Fig. 3.1 is fitted with Eq. (3.1.2). From the fits of each of twenty-four CHD paddles one can estimate the attenuation length λ and the fraction β of reflected light from PMT. The results are summarized in Tab 3.1.

The response of each CHD paddle is described by a function $f(x)$ with three parameters λ, a, and b. Now the light signal for each event can be

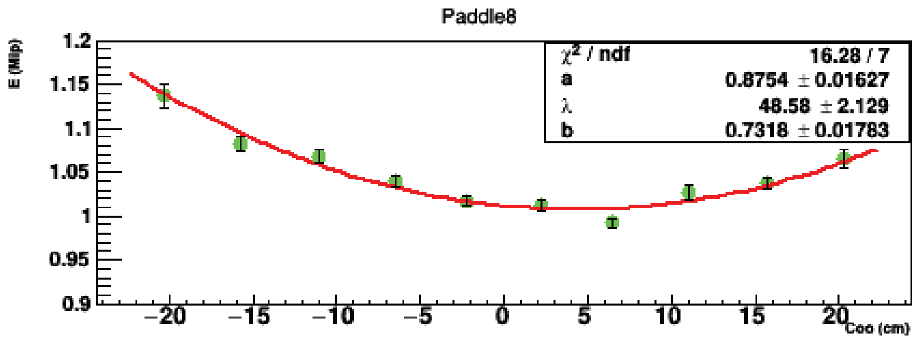

Figure 3.2: *Proton signal for CHDY layer: an example fit for paddle 8. The points represent the the signal from each of the ten longitudinal segments the paddle is divided into. The CHD coordinate x is shown on the abscissa. The red line is the fit with* (3.1.2)*.*

Table 3.1: *Attenuation length and fraction β of reflected light from PMT for each CHDX, CHDY paddles.*

Parameter	Padd.1	Padd.2	Padd.3	Padd.4	Padd.5	Padd.6	Padd.7
λ_X (cm)	65.7 ± 5.7	66.0 ± 5.8	53.5 ± 2.5	64.26 ± 4.2	59.2 ± 2.9	79.9 ± 6.1	85.5 ± 9.3
$\beta_X(\%)$	68	81	69	91	99	83	91
λ_Y (cm)	71.8 ± 8	73.9 ± 8.3	63.8 ± 3.6	67.4 ± 3.2	65.2 ± 3.9	49.8 ± 2.1	56.5 ± 3.3
$\beta_Y(\%)$	50	99	94	88	99	90	81
Parameter	Padd.8	Padd.9	Padd.10	Padd.11	Padd.12	Padd.13	Padd.14
λ_X (cm)	68.3 ± 4.7	64.1 ± 4.6	53.8 ± 3.2	63.1 ± 3.9	66.4 ± 5.0	51.2 ± 2.7	81.29 ± 10
$\beta_X(\%)$	88	77	83	99	92	75	81
λ_Y (cm)	48.6 ± 2.1	61.8 ± 3.5	52.5 ± 2.3	50.1 ± 2.2	73.7 ± 12.6	85 ± 19	65 ± 6
$\beta_Y(\%)$	84	99	73	99	92	99	87

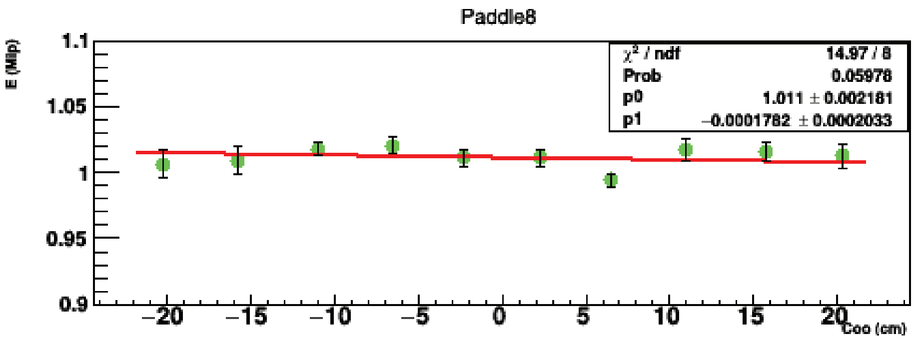

Figure 3.3: *Proton signal after correction for CHDY layer: an example fit for paddle 8. The points represent the the signal from each of the ten longitudinal segments the paddle is divided into. The CHD coordinate x is shown on the abscissa. The red line is the fit with a straight line.*

corrected according to the following relation

$$\bar{E}(x) = E(x)\frac{A}{f(x)}, \tag{3.1.3}$$

where $E(x)$, ($\bar{E}(x)$) is the signal in the point of x coordinate before, (after) the correction, A is a normalization parameter for a given paddle and $f(x)$ is the value of Eq. (3.1.2) in the point at x. In Fig. 3.3 the proton signal for the eighth CHDY paddle as a function of the paddle coordinate after the Eq.(3.1.3) correction is shown. The single measurements of proton signal after the correction differ from the fitting function by less than $\pm 2\%$. An example of the deviation is reported in Fig. 3.4 and in Fig. 3.5 for the fifth paddle of the CHDX and for the eighth paddle of the CHDY respectively.

Since the position dependence of the signal does not depend on the charge, the conversion factors obtained by proton can be used to correct the signals from all nuclei. In Fig. 3.6 the deposited energy in CHDX before and after correcton is shown. As one can see the effect of correction is to shrink the width of each peak.

The effect is clarified in Fig. 3.7 where a zoom of Fig. 3.6 for iron and its gaussian fit is shown, before and after correction. The improvement in resolution resolution for Fe after correction is of the order of 15%.

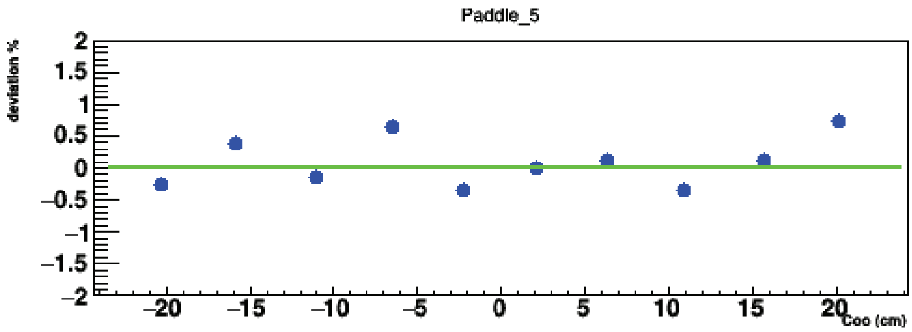

Figure 3.4: *The deviation of corrected signal from a straight line fit for CHDX paddle five.*

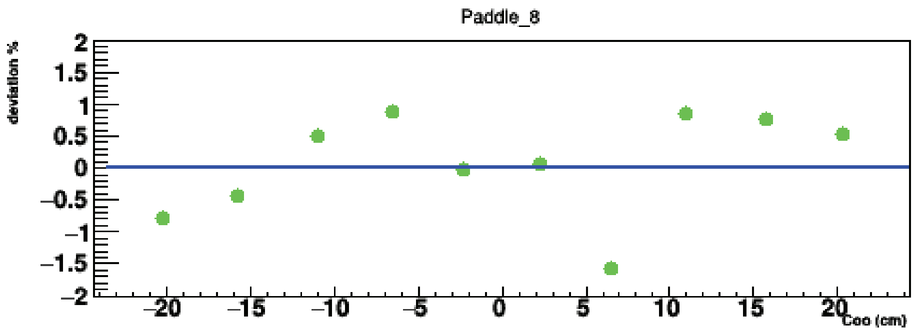

Figure 3.5: *The deviation of corrected signal from a straight line fit for CHDY paddle eight.*

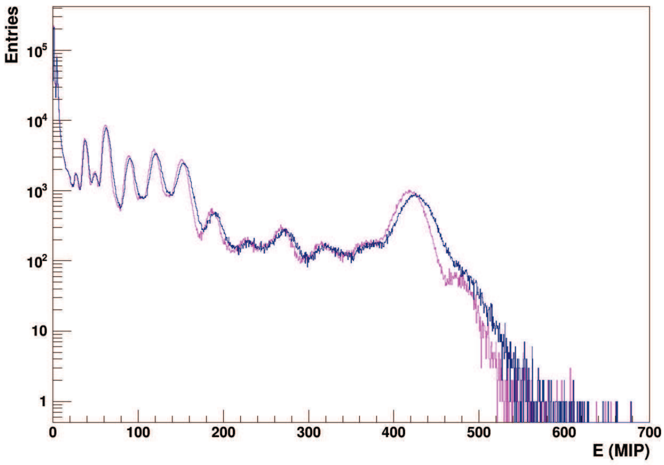

Figure 3.6: *dE/dx before (blue) and after (magenta) correction in CHDX.*

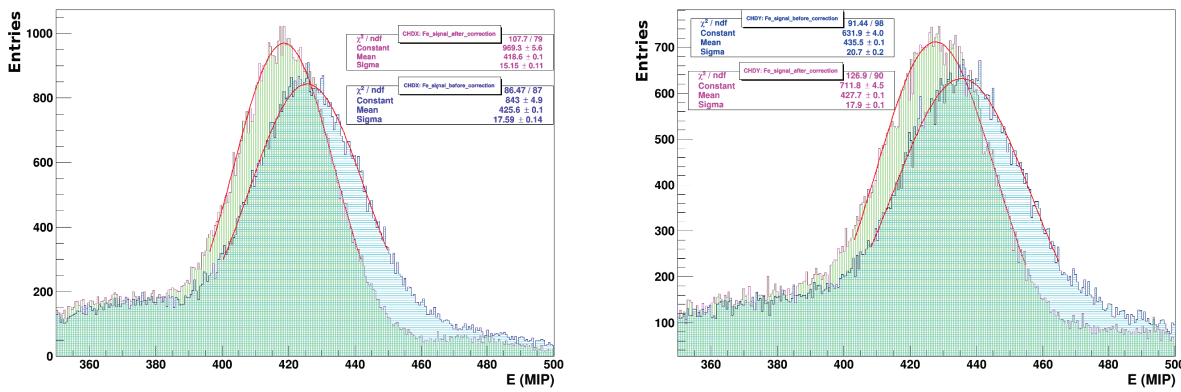

(a) *CHDX* **(b)** *CHDY*

Figure 3.7: *Fe signal before (blue) and after (magenta) correction.*

3.2 Light quenching effect in the plastic scintillators

It is well known that the plastic scintillators are non-linear in their response: as the amount of energy lost by a penetrating particle increases (e.g. with increasing Z of relativistic cosmic ray nuclei) the light output is no longer proportional to the energy lost. The scintillation efficiency dL/dE is reduced in the case of a large linear energy transfer, dE/dx, which is known as quenching effect. Quenching reduces the scintillation photon yield, so that the charge resolution is reduced.

According to several models (G. Tarlé et al.,1979 [66], P. Ahlen, 1980 [67]), the measured light output per unit distance dL/dx, due to an ion crossing a plastic scintillator is a sum of two components: the *core* emission of primary scintillation and the *halo* emission of secondary electrons (delta-ray). The core is a cilindrical region of very dense ionization energy loss around the particle track, whereas the halo is the surrounding region farther away from the track. Near the particle path the highest energy density is deposited and it comes from the excitations produced by the primary particle and by slow secondary electrons arising from distant collision between the primary and the electrons in the medium. The core is the dominant component of the scintillation for electrons and light ions. Farther from the track, energy is deposited only by energetic delta rays arising from close collision, which represents the tail of the energy loss distribution and are rarer. The halo emission becomes dominant when dE/dx is large, i.e. for heavy ions at intermediate energies.

The core component was described extensively by Birks [68] according the following parametrization for the light output per unit path length:

$$\frac{dL}{dx} = \frac{A\frac{dE}{dX}}{1 + B\frac{dE}{dx}} \tag{3.2.1}$$

where B is a quenching parameter and A is an arbitrary gain factor. From this formula one can notice that dL/dx approaches a constant saturation value when dE/dx increases. This parametrization was generalized by Chou [69]:

$$\frac{dL}{dx} = \frac{A\frac{dE}{dX}}{1 + B\frac{dE}{dx} + C\left(\frac{dE}{dx}\right)^2}. \tag{3.2.2}$$

In both parametrizations the effect of delta-rays interactions are neglected. The halo term appears in the works by Meyer and Murray [70] and then by Voltz [71] and Tarlé [66].

In particular, the Tarlé parametrization is the natural extension of Birks's formula:

$$\frac{dL}{dx} = \frac{A(1-f_h)\frac{dE}{dX}}{1+B(1-f_h)\frac{dE}{dx}} + Af_h\frac{dE}{dx} \tag{3.2.3}$$

where the first term represents the saturating part of the light output from the core, while the second is not saturated and represents the light contribution from the halo. The parameter f_h represents the fraction of the energy loss spent for delta-ray production. An expression for f_h has been derived by Ahlen [67]:

$$f_h = \frac{1}{2}\frac{ln(2mc^2\beta^2\gamma^2/T_0) - \beta^2}{ln(2mc^2\beta^2\gamma^2/I) - \beta^2} \tag{3.2.4}$$

where β is the ion velocity, $\gamma = (1-\beta^2)^{-1/2}$, m is the electron mass, I is the mean logarithmic ionization potential of the scintillator, and T_0 is the threshold energy for delta-ray formation, which determines the core-halo boundary.

The Voltz parametrization considers two distinct components of the scintillation. The first one, referred to as the *prompt* is the *core+halo* contribution, whereas the second or *delayed* scintillation component results from singlet states produced by the bimolecular interaction of molecules in the lowest triplet state which are mainly formed following the rapid recombination of ions in the particle track. The contribution of the latter is small for energetic particles and it can be neglected [71]. Therefore, for the *prompt* component, one can write:

$$\frac{dL}{dx} = A\Big[(1-f_h)exp\Big(-B(1-f_h)\frac{dE}{dx}\Big)+f_h\Big]\frac{dE}{dx}. \tag{3.2.5}$$

It is interesting to note that Eq. (3.2.3) is the first order expansion in powers of $B(1-f_h)\frac{dE}{dx}$ of the Eq. (3.2.5).

The deposited energy $\frac{dE}{dx}$ can be written as αZ^2 where, for a plastic scintillator, $\alpha = 2\,MeV g^{-1} cm^2$. Hence, from Eq. (3.2.5) and (3.2.3) one can observe that the lower energy density in the halo is compatible with a linear response in Z^2 of the scintillation light yield. However, for the core, while the Eq. (3.2.3) predicts a constant saturation value, Eq. (3.2.5) predicts an increase up to a maximum value. The contribution of the halo with respect to the core becomes dominant for relativistic ions of high Z due to the larger momentum transfer available to delta rays. Therefore, for a given incident kinetic energy per nucleon, the ionization yeld results in a linear dependence with respect to Z^2 for light nuclei ($Z < 9$), non linear for $9 < Z < 14$ and quasi linear dependence for heavy nuclei ($Z > 14$).

There are physical consequences of the mathematical difference between the two versions. In particular in Eq. (3.2.5) the core contribution increases, reaches a maximum and then decreases asymptotically to zero. This is not the case if one only takes the approximate expression, Eq. (3.2.3). Here the core contribution increases to a maximum and gradually saturates. Physically, as the specific energy loss increases, the light from the core tends to follow the behavior given by the approximate expression. It would never be expected to fall back towards zero.

The Tarlé parametrization was used to obtain the performance of the CHD scintillator. Some results about this performance, as obtained in a dedicated beam test [72], when a single CHD paddle was tested, are shown in Fig. 3.8 (a) e (b). In Fig. (a) solid black line represents the scintillator signal vs. Z^2, normalized with respect to the average response for a $Z = 1$ particle. The ideal response curve in case of no saturation (red line) and the fraction of measured signal with respect to the expected one (blu line) are also plotted. The blue line shows that the effective loss approaches 60% in the iron region, while from the fit of the measured signal response (black) with equation (3.2.3) it is possible to obtain the following values for the parameter of Tarlé parametrization: $f_h = 0.36 \pm 0.01$, $B = (8.0 \pm 0.3) \cdot 10^{-3} g\, cm^{-2} MeV^{-1}$.

In the following, a new parametrization of light saturation has been introduced. In fact, expanding at second order in powers of $B(1 - f_h)\frac{dE}{dx}$ the Eq. (3.2.5) one obtains a new formula (3.2.6), where the core component of the scintillation increases to a maximum and than decrease more slowly than

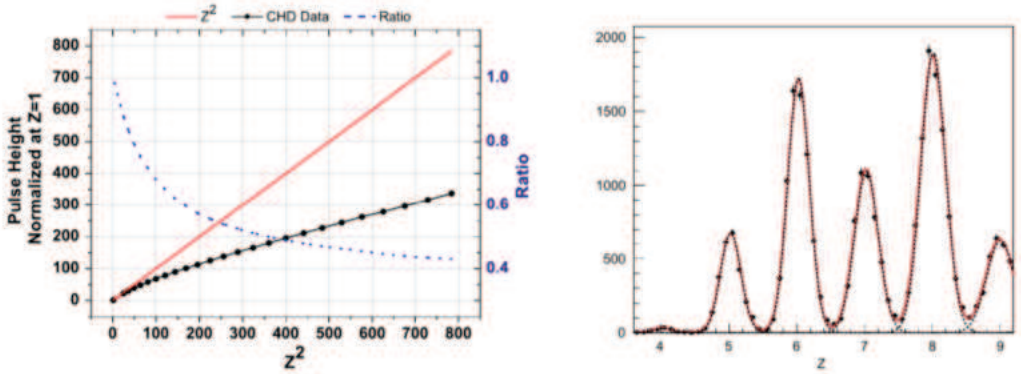

(a) Response function of scintillator EJ204.

(b) Charge distributions from the scintillator for Be, B, C, N, O.

Figure 3.8: *Beam test results at GSI.(Marrocchesi et al., 2011) [72].*

Eq. (3.2.5):

$$\frac{dL}{dx} = \frac{A(1-f_h)\frac{dE}{dX}}{1+B(1-f_h)\frac{dE}{dx}+\frac{1}{2}(B(1-f_h))^2(\frac{dE}{dx})^2} + Af_h\frac{dE}{dx} \tag{3.2.6}$$

The Fig. 3.9 shows the halo and core components of the three parametrization for a fixed parameters value.

In the following the two variants of the core/halo model and the parametrization coming from Voltz equation will be compared.

3.2.1 Light saturation in CHD

In this section the study of light saturation in CHD is reported using calibrated flight data, from December 2015 to August 2016, according to the method described in [65]. Then the calibrated data are selected as explained in section 3.1.1. and using the High Energy Shower Trigger, to select cosmic nuclei from H to Fe (see Chap. 2.2.1).

In order to estimate the light saturation effect each individual peak of the energy loss distribution in the $Z > 2$ range has been fitted with a Gaussian function for both CHDX layer and CHDY layer. Proton and Helium have been fitted with a Landau-Gaussian convoluted function. An example of the CHDX fit for proton and oxygen is shown in Fig. 3.10. Than, the mean

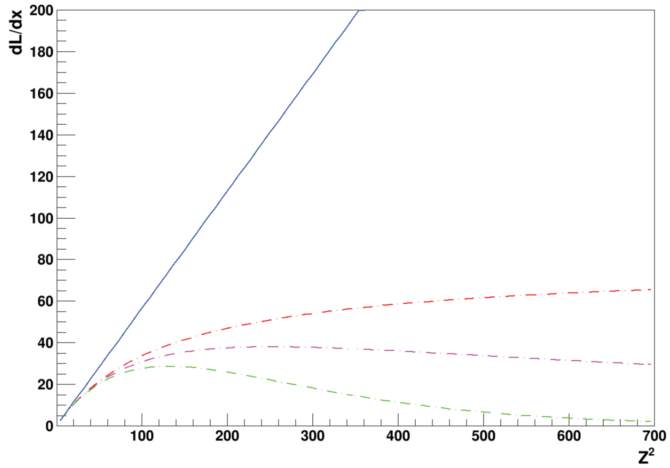

Figure 3.9: *The Halo (solid line) and Core (dashed lines) components for Tarlé (red line), Voltz (green line) and Voltz II order (magenta line) parametrizations. The used parameters are:* $B = 0.007411\, g\, MIP^{-1} cm^{-2}$; $\alpha = 2\, MIP\, g^{-1}\, cm^{-2}$; $f_h = 0.4885$; $A = 0.5775\, MIP^{-1}$.

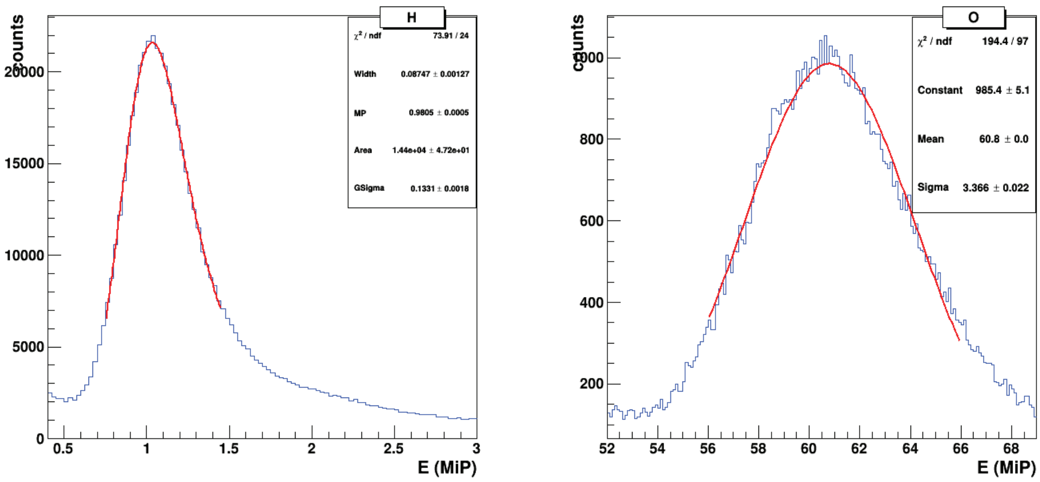

Figure 3.10: *Landau-Gaussian convoluted fit for proton (left) and Gaussian fit for oxygen (right).*

pulse height given from the fit is plotted versus Z^2 both for CHDX layer and CHDY layer. The result is shown in Fig. 3.11, where the blue and green line represent the Tarlé parametrization for CHDY and CHDX layers respectively. In Fig. 3.12 the same plot is fitted with the Voltz II order parametrization. Resulting fit parameters for CHDX and CHDY for both parametrizations are summarized in the boxes. As one can see both version of the model give a good data fit. However, there is indication that the curvature of the Voltz II order model fit provides a better match to the trend of the data: the value of χ^2 is lower in this case, for both CHD layers.

The difference in the curvature between CHD layers can be understood comparing the values of the parameters: only B and A differ between the two layers. In particular the slightly larger value B in the CHDY indicates a larger core quenching with respect to CHDX layers. The A parameter (larger in CHDY layers) indicates a different overall gain normalization. However the fraction of secondary electrons in the halo region, f_h, seems to be the same in the two layers.

3.2.2 Light saturation in IMC

As seen for the CHD, each individual peak of the energy loss distribution is necessary to estimate the light saturation effect. However, infering the charge from the energy deposits of the incoming particle in the IMC fibers is more difficult than in CHD. The point is that the interaction probability inside the IMC is not negligible and after the interaction, the particle can no longer be considered as a Mip. Therefore only the energy deposits in fibers upstream the interaction point can be used to get a measurement of the energy loss by ionization. So, in order to estimate light saturation in IMC, only the mean of the layers before the interaction point is used[2](Fig. 3.13). However the energy peaks are not completaly resolved for element with $Z > 14$, therefore it is not possible to fit them. In order to resolve each peak of the

[2]For a detailed explanation on the method to reconstruct the particle interaction point see [41]

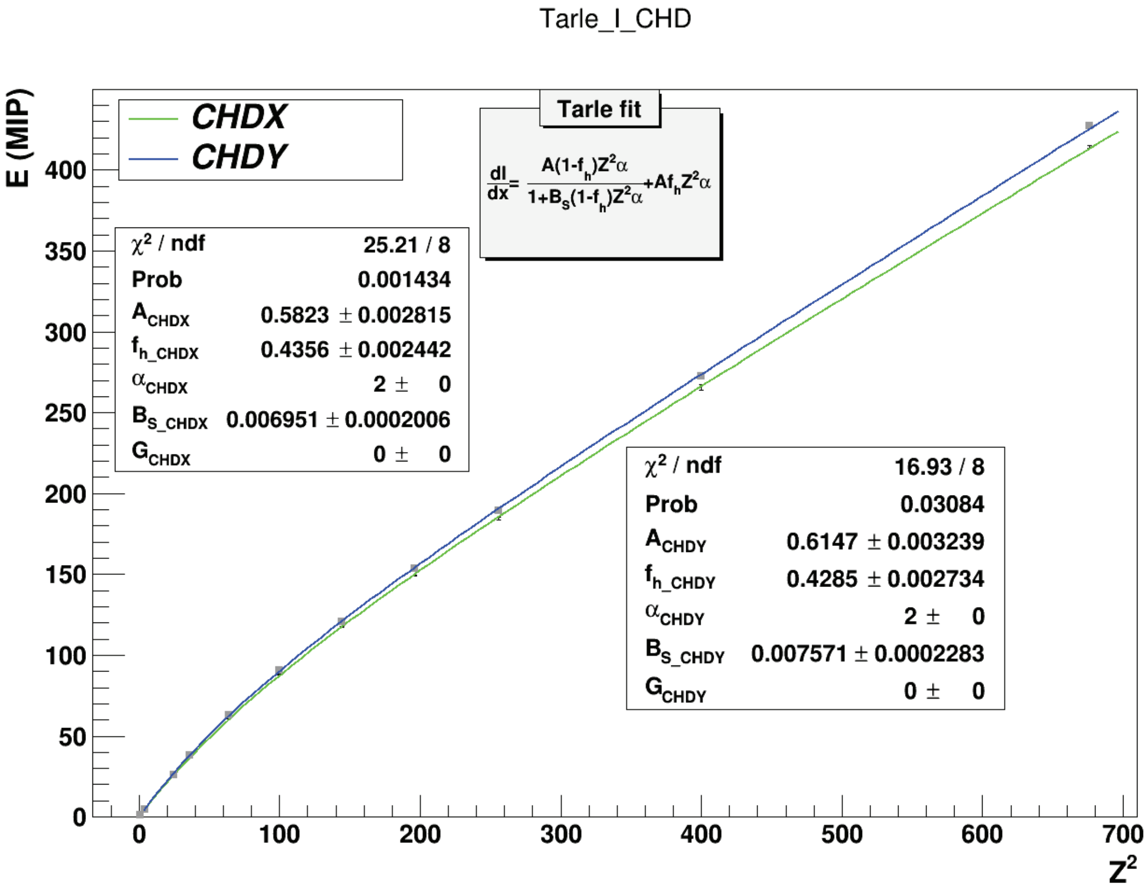

Figure 3.11: *Plot of mean pulse height from H to Fe vs. Z^2 for CHDX and CHDY signal. The green (blue) line is the fit with Tarle parametrizzation for CHDX (CHDY).*

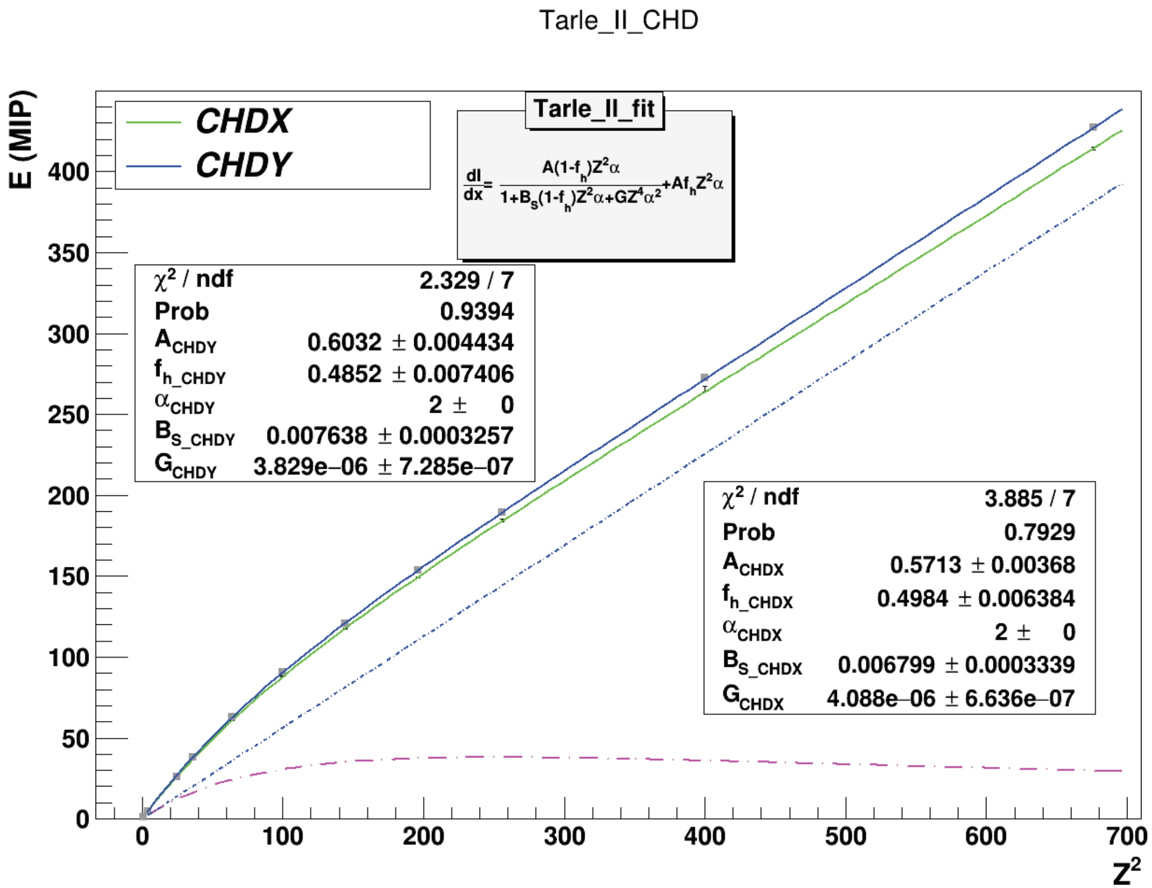

Figure 3.12: *Plot of mean pulse height from H to Fe vs. Z^2 for CHDX and CHDY signal. The green (blue) line is the fit with Voltz II order parametrizzation for CHDX (CHDY). The dashed lines represent the core contribution (magenta) and the halo contribution (blu) from CHDY.*

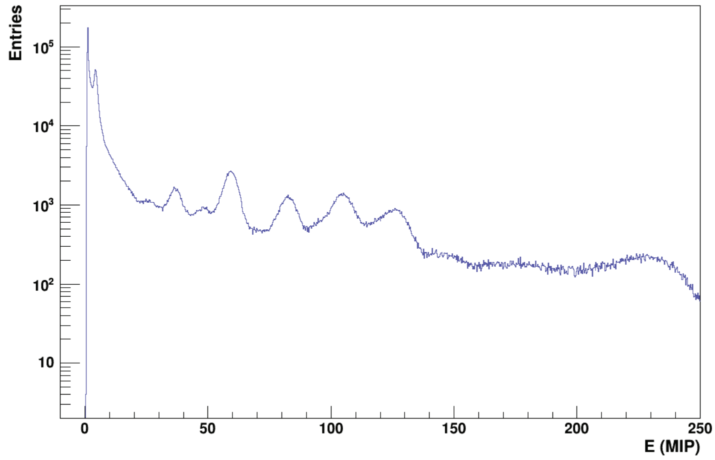

Figure 3.13: *dE/dx mean before interection point in IMC.*

energy loss distribution in IMC, the corresponding energy loss distribution ranging from H to Fe has been selected using the CHDX layer. In Fig. 3.14 the plot and the fit of proton and oxygen in IMC after the corrisponding CHDX selection is shown. Now let us proceed as for CHD. The mean pulse height given from the fit is plotted versus Z^2 for IMC. The Fig. 3.15 and Fig. 3.16 show the fits with Tarlé and Voltz II parametrizations respectively. The curves representing the core and halo contributions to the total light signal are also shown. As in the CHD, the value of the χ^2 is lower for Voltz II model fit: this parametrization seems to provide a slightly better match to the trend of the data. Resulting fit parameters show different value with respect to CHD ones. In particular the fraction of secondary electrons in the halo region, f_h, results lower in IMC: this difference may be due to different size of CHD paddles and IMC fibers that is reflected in a smaller halo region in IMC fibers. If one compares the core and halo contribution of CHD with IMC ones from Fig. 3.15 and Fig. 3.16 it can be noted that in the latter the core is dominant with respect to halo for low Z and become comparable for high Z ($Z \sim 20$). In the CHD, instead, the halo and core are comparable for low Z ($\sim Z < 10$), whereas for higher Z the halo component dominates.

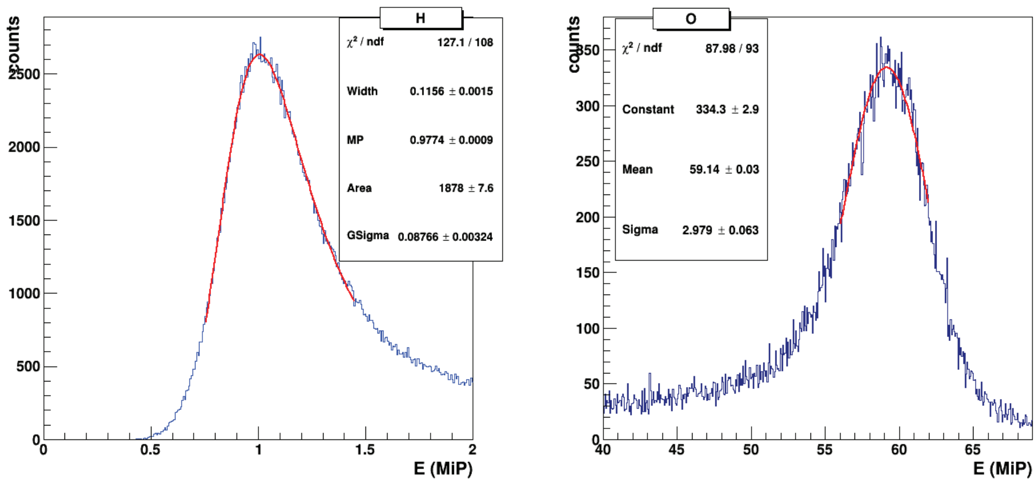

Figure 3.14: *Landau-Gaussian convoluted fit for proton (left) and Gaussian fit for oxygen (right) in IMC after a selection cut in CHDX.*

3.2.3 Light saturation correction in CHD and IMC

In order to correct the CHD and IMC response for the saturation effect, the parameters of the Voltz II model have been used to extract the inverse functions. Fig. 3.17 shows the dE/dx in Z units for CHDX, CHDY (a) and IMC (b) after the correction. In Fig. 3.18 the plots of corrected charge vs Z for CHD (a) and IMC (b) are shown. As one can see the signal of both detectors is linear in Z after light saturation correction.

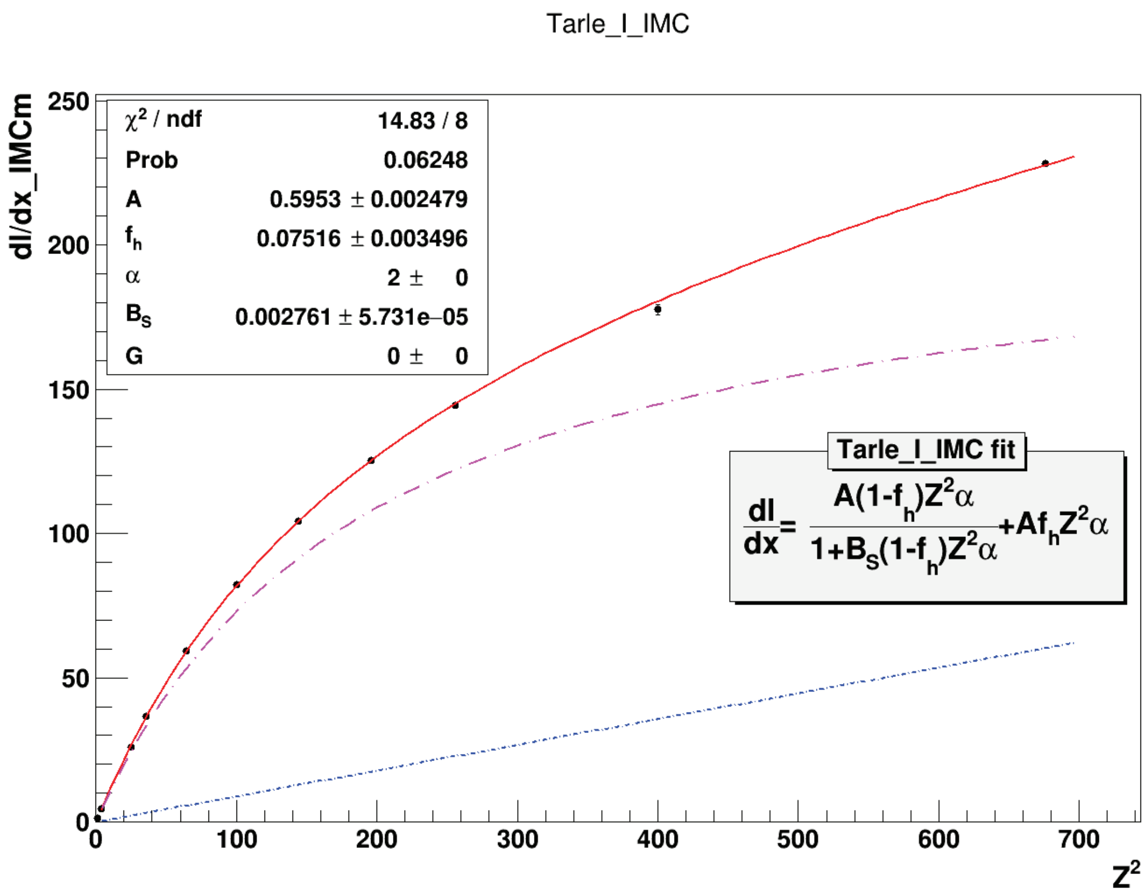

Figure 3.15: *Plot of mean pulse height from H to Fe vs. Z^2 for IMC mean signal. The red line is the fit with Tarlé parametrizzation. The dashed lines represent the core contribution (magenta) and the halo contribution (blu).*

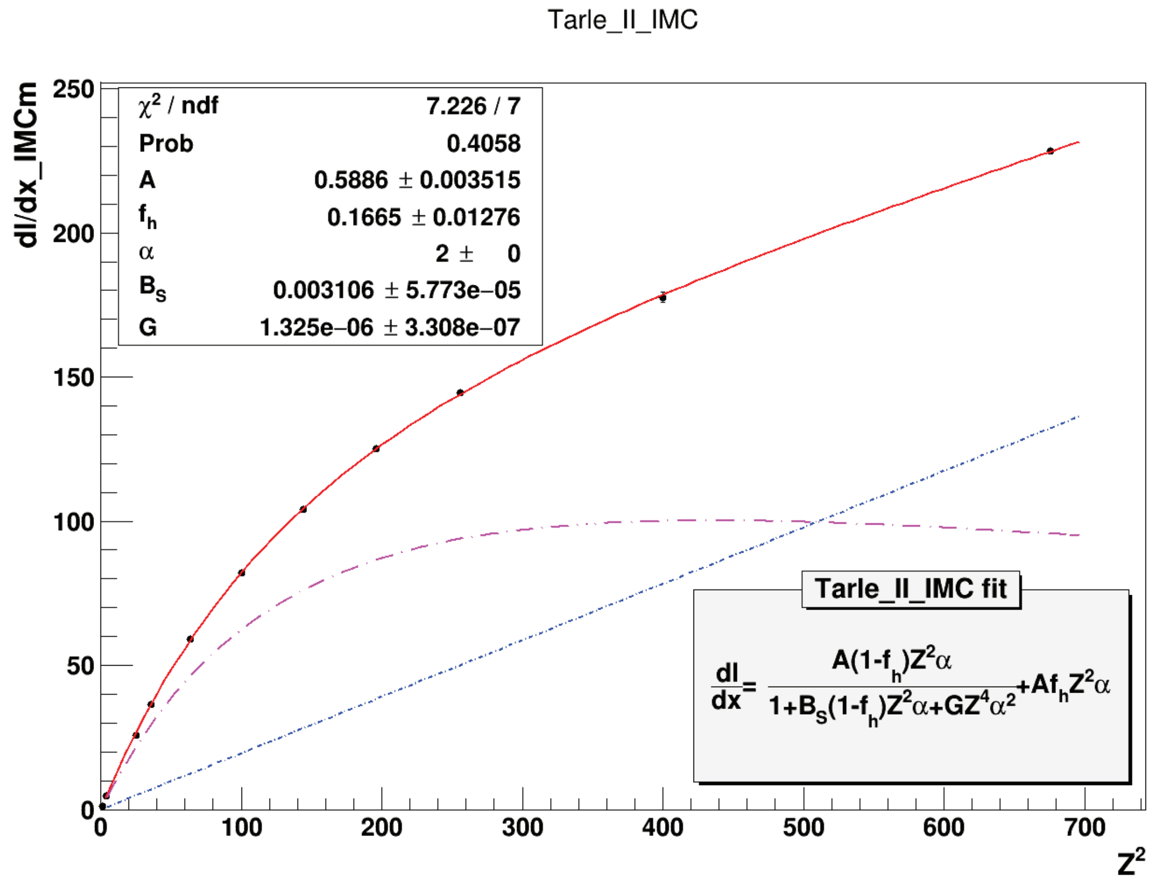

Figure 3.16: *Plot of mean pulse height from H to Fe vs. Z^2 for IMC mean signal. The red line is the fit with Voltz II order parametrizzation. The dashed lines represent the core contribution (magenta) and the halo contribution (blu).*

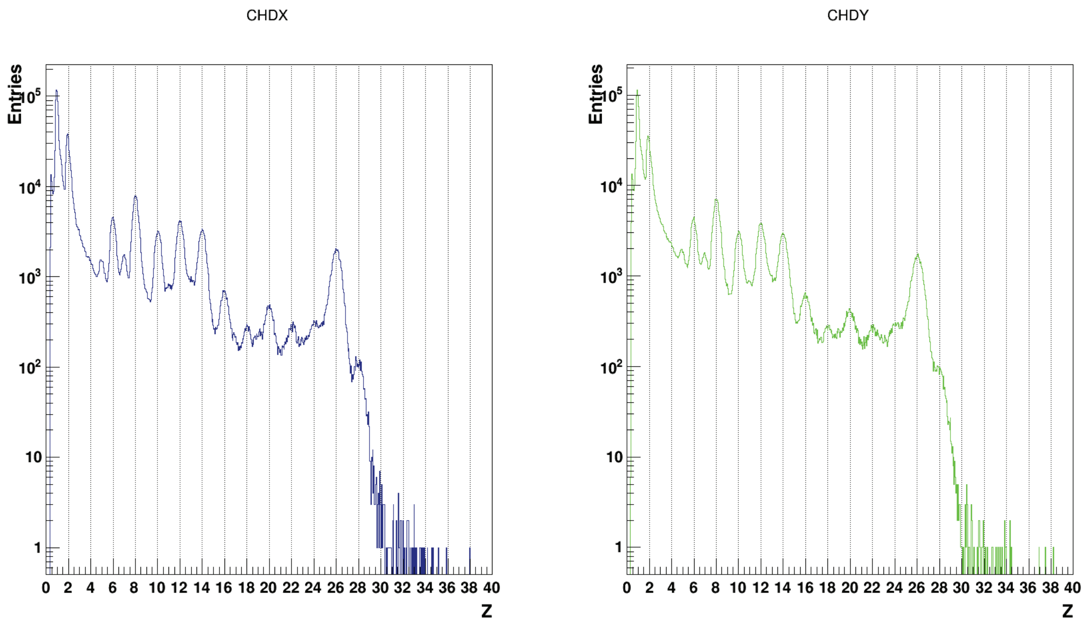

(a) CHDX (left) and CHDY (right).

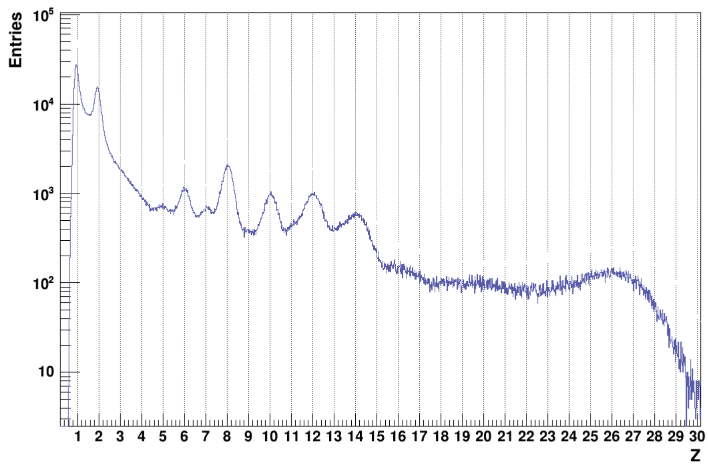

(b) IMC.

Figure 3.17: *dE/dx in Z units for CHD and IMC after calibration.*

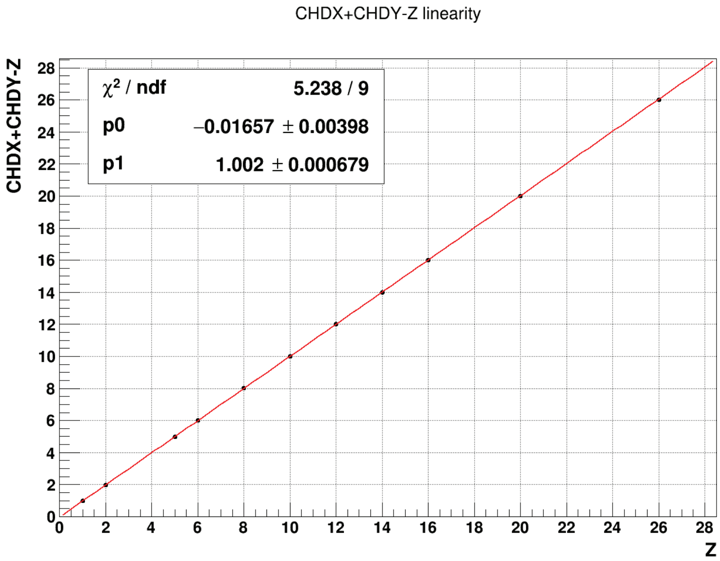

(a) CHDX+CHDY.

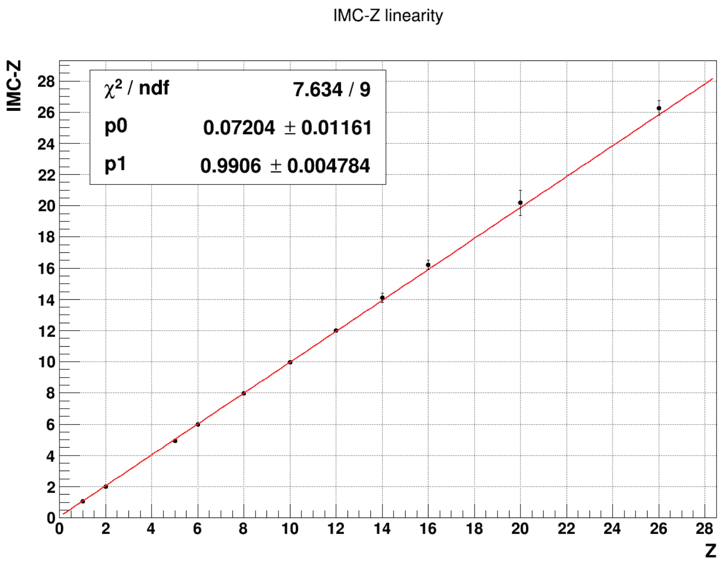

(b) IMC.

Figure 3.18: *CHDX+CHDY and IMC linearity after calibration.*

Chapter 4

Identification of cosmic nuclei

As explained in Chap. 1.3 the energy dependence of the ratio of the fluxes of secondary-to-primary elements can be used to discriminate among different propagation models. This observable is less prone to systematic errors than absolute flux measurements. The energy dependence of the propagation path-length is parametrized in the form $E^{-\delta}$. An accurate measurement of the parameter δ is crucial to infer the shape of the spectra of individual elements at the source by correcting the observed spectrum for the energy dependence of the propagation term. Clearly, it is necessary to identify, with no ambiguity, the incoming nucleus and to measure its energy. So, the measurement of the electric charge of the incoming particle becomes essential to separate different elemental species among the fully stripped nuclei that are present in the cosmic ray flux. For this reason CALET has a dedicated charge detector on top of the instrument. Thanks to its fine granularity and multiple dE/dx measurements, a redundant charge measurement can be carried out by IMC. In fact, especially at high energies, charge tagging in the CHD becomes more challenging, due to the albedo of backscattered particles emerging as secondaries from the interactions in the calorimeter. So the IMC (CHD) can be used as a charge selector to improve the charge separation in the CHD (IMC).

In this chapter charge tagging using both the IMC and the CHD and the performance in terms of the charge resolution of both detectors are described.

4.1 Data Selection

Prior to the identification of incoming nuclei, it is essential to apply selection criteria to flight data. A proper selection accepts events for which the trajectory of the incident particle is well reconstructed before it eventually undergoes an interaction in the apparatus. In fact, charge identification requires a backward extrapolation of the track to the CHD planes to determine which paddle has been hit. In the present thesis only the track reconstructed with the Kalman Filter (KF) technique is taken into account (Good Tracking selection)[1].

To identify cosmic nuclei from H to Fe it is necessary to select the High Energy Trigger that, according to Chap. 2.2.1, allows to select protons and nuclei in the energy range $10\,GeV - 1000\,TeV$.

Furthermore one has to reject events that hit the calorimeter outside CALET acceptance since this kind of event could result into a fake charge identification. According to Chap. 2.2.2 only the tracks that cross CHDX and CHDY layers, the top and bottom TASC layers, and are well contained within a fiducial volume in the TASC are selected (Acceptance selection).

It is possible, also, that a track hits two paddles of the same CHD plane or that it hits the edge of a paddle (Fig. 4.1). In the first case one can have a misidentification of the hit paddle, in the second case the corner-clipping effect may not be negligible. So, a fiducial zone is defined excluding a region of $0.05\,mm$ close to the edge of each paddle, and only tracks that hit the same paddle in the plane are take into account.

[1]For a detailed explanation on the KF traking algorithm see [73]

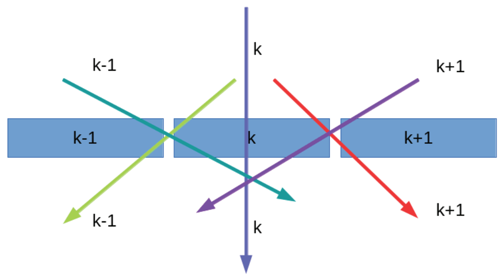

Figure 4.1: *Possible track configurations when hitting a CHD layer.*

4.2 Charge selection with IMC and CHD

In order to improve the charge selection one can take advantage of both the CHD planes and IMC detector. The IMC, thanks to its fine granularity, helps reducing the contamination from backscattering. Furthermore multiple dE/dx samples allows to have up to 16 specific ionization measurements from which one can infer the value of the charge. Instead the CHD thanks to its thick plastic scintillators has high photostatistics and low interaction probability.

Using the information from CHDX and CHDY layers a specific nucleus can be pre-selected and its charge observed in the IMC. In the same way using the information of IMC and one plane of CHD a specific nucleus can be pre-selected and its charge observed in the other CHD plane. Since in the IMC the interaction probability is not negligible, only the planes upstream the particle interaction point can be used to measure multiple dE/dx. For this purpose a specific algorithm has been optimized [41]. The routine calculates the mean or the truncated mean of the IMC planes before the interaction point. In Figs. 4.2, and 4.3 the correlation plot between CHDX-CHDY and CHDX-IMC(mean) are shown, respectively: individual elements from H to Fe are clearly separated, but in the CHDX-IMC(mean) plot a tail extending to lower vaues of the IMC mean charge is shown when a nucleus is identified by CHDX[2]. This is in most cases due to an erroneus interaction point estimation:

[2] The correlation plot CHDY-IMC is not reported, but it shows the same behaviour

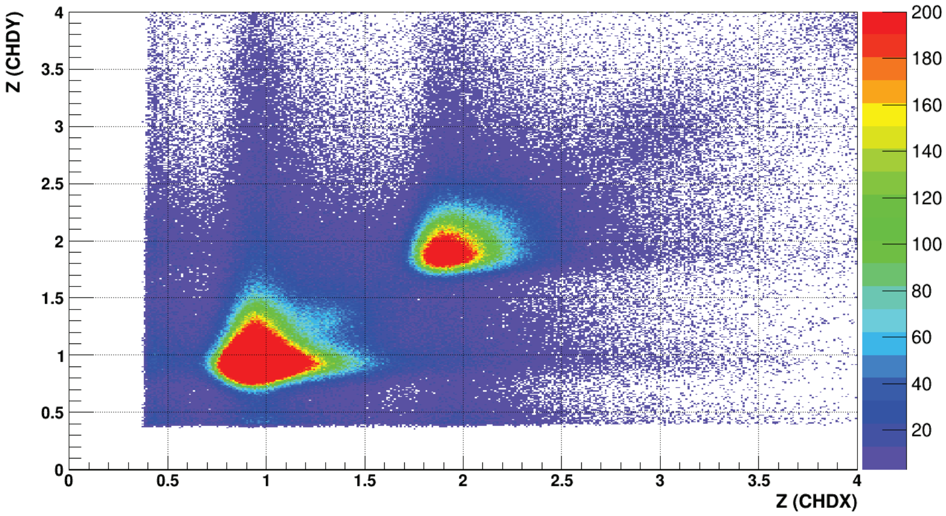

(a) H and He in CHDX-CHDY plot.

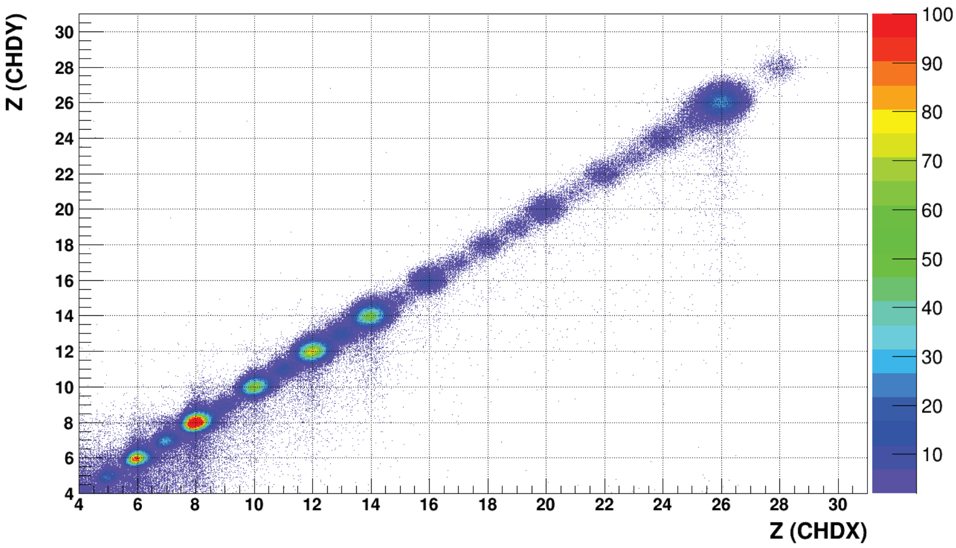

(b) Z>4 in CHDX-CHDY plot.

Figure 4.2: *Correlation plot between CHDX-CHDY.*

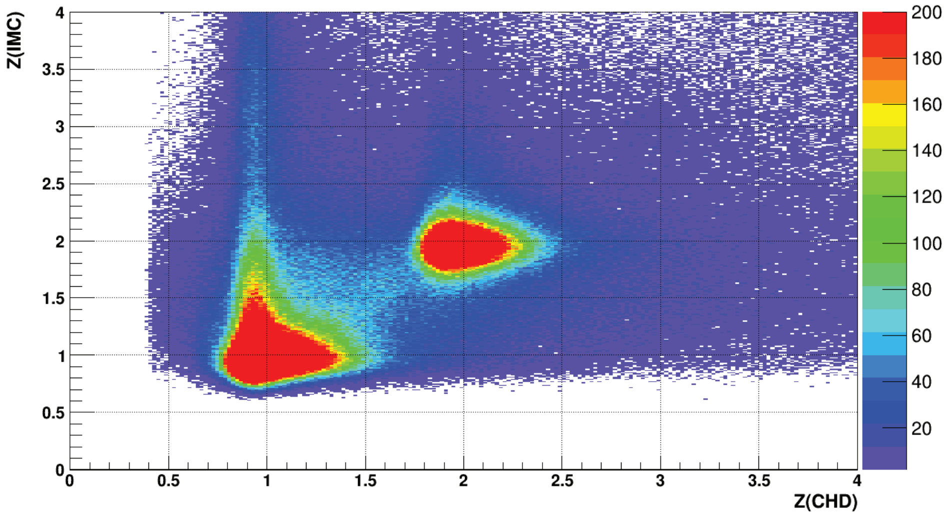

(a) H and He in CHDX-IMC plot.

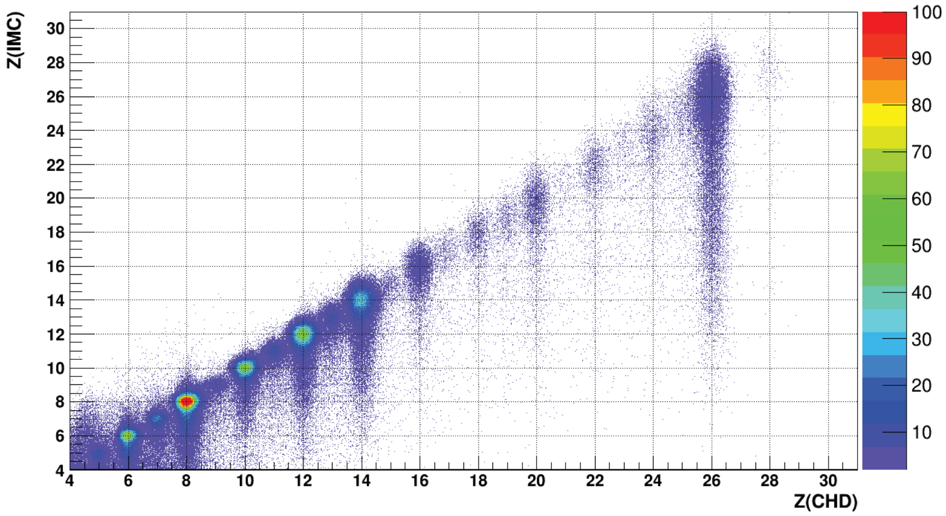

(b) Z>4 in CHDX-IMC plot.

Figure 4.3: *Correlation plot between CHDX-IMC.*

in fact if the particle interacts in the $n-1$ plane but the estimated interaction point is in the n plane , the fragmentation of the incident particle leads to misidentification of charge in the n plane. A possibility to reduce the problem is discussed below.

A possibility in the charge pre-selection is to perform an elliptical cut in the correlation plot between the two CHD layers according to the following expression:

$$\frac{(cos\theta X - sin\theta Y)^2}{r_x^2} + \frac{(sin\theta X + cos\theta Y)^2}{r_y^2} < 1 \tag{4.2.1}$$

where $X = Z_{plane1} - X_C$ and $Y = Z_{plane2} - Y_C$, the point (X_C, Y_C) is the center of the ellipse. The scale of the ellipse can be varied using the ellipse parameter $r = (r_x + r_y)/2$. In order to establish an optimal selection region, a study of the efficiency selection and contamination of the charge sample has been performed varying the r scale parameter. Using flight data, a multi-gaussian fit has been performed of the charge distribution from CHDX and CHDY in the region $6 < Z < 10$ to define a charge selection cut based on the r scale parameter for oxygen. A first order estimate of the charge overlap in the oxygen region due to the tails of the charge distribution of neighbor elements has been carryed out using a toy Montecarlo whereby the gaussian parameters have been extracted from multigaussian fit from the flight data. In Fig. 4.4 (a) the fraction of selected element as a function of the r parameter is shown while the fraction of events leaking into the selected region is shown in Fig. 4.4 (b).

For this pre-selection one wants to have leaking events from neighbors under control in order to have a high purity sample. In this case, selecting a sample with $r = 0.25 - 0.3$ the fraction of leaking events is $\sim 0.3\%$ and the efficiency is around 40%. In Fig. 4.5 two elliptical cuts for oxygen pre-selection are shown.

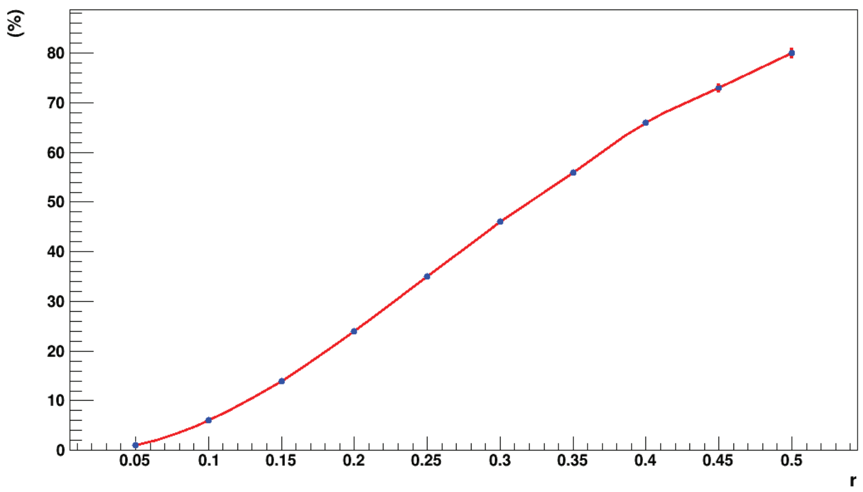

(a) Fraction of oxygen selected events.

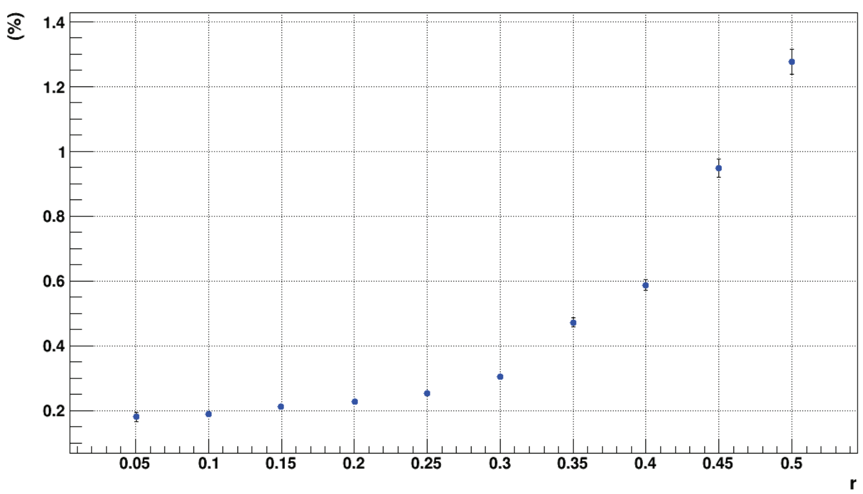

(b) Ratio of neighbor events versus oxygen candidates.

Figure 4.4: *Example of oxygen selection as a function of parameter r.*

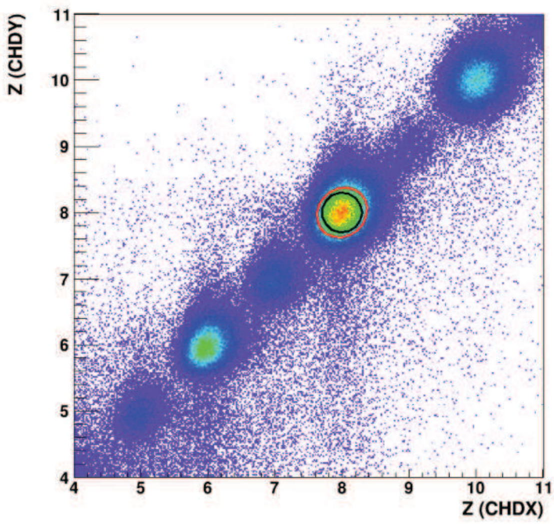

Figure 4.5: *Elliptical cuts in CHDX-CHDY correlation plot for oxygen, according to Eq.* (4.2.1)*: the parameters r are* 0.3 *and* 0.35 *for black and red cut.*

4.3 Charge resolution in CHD

The variance of the charge distribution in CHDY is determined by pre-selecting an exclusive sample of events for each element in the IMC-CHDX plane, as explained in the previous section, and fitting the signal in CHDY with a Gaussian distribution for elements from B to Fe and with a Landau-Gaussian convoluted function for Proton and Helium. The CHDY signal is obtained for element from H to Fe. The procedure is the same for the variance of the charge distribution in CHDX, but each element is pre-selected in IMC-CHDY plane. The charge resolution in terms of the unit charge e is defined as:

$$\sigma_Q = \frac{\sigma}{\mu_{Z+1} - \mu_Z} \tag{4.3.1}$$

where μ and σ are respectively the mean and the sigma value of the fitting curve for a Z nucleus. For Proton and Helium the FWHM is used instead. It is useful to note that the CHD signal is in Z units, so the denominator in

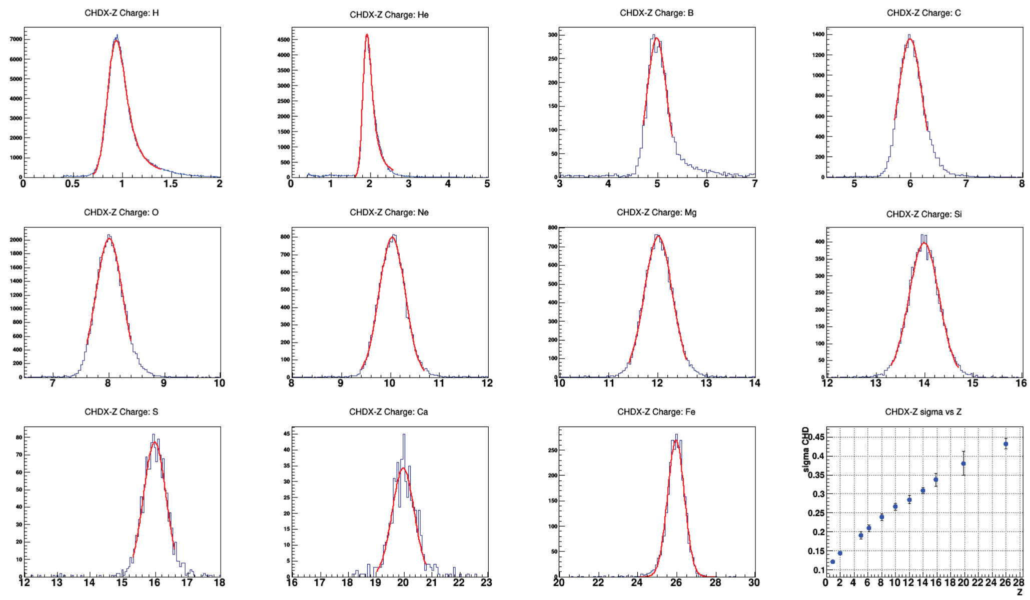

Figure 4.6: *The plots and the fits (in red) of nuclei from H to Fe in CHDX after cut pre-selection in the IMC-CHDY plane, and the charge resolution for the CHDX.*

Eq. (4.3.1) is $\sim$ 1 and the effective charge resolution[3] is simply the sigma value of fitting curve. The charge separation power (in units of σ) is defined as the reciprocal of Eq. (4.3.1). The measured charge resolution σ for the CHDX scintillator layer is plotted in Fig. 4.6 for elements from proton to iron and it spans from $0.12\,e$ at H to about $0.43\,e$ at Fe. In the same figure the signal for each nucleus in the CHDX is plotted. In Fig. 4.7 the charge resolution σ for the CHDY scintillator layer is plotted. In this case it spans from $0.14\,e$ at H to about $0.51\,e$ at Fe. The lower resolution in CHDY is due to the back-scattered particles coming from the calorimeter causing an extra amount of deposited energy along the length of the scintillator.

[3] The 68% of values that lie around the mean in the normal distribution defines the charge resolution.

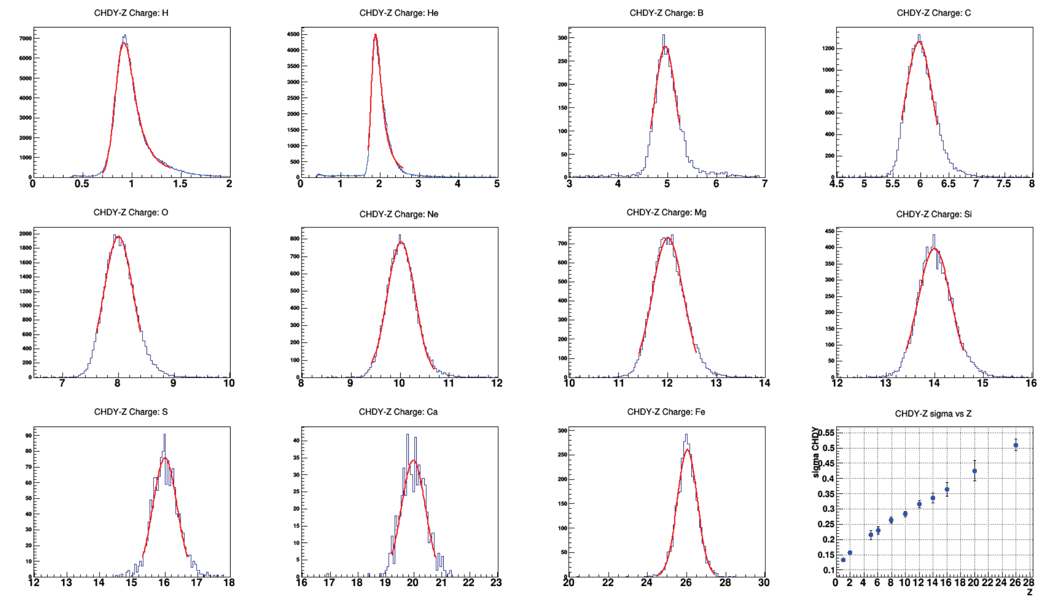

Figure 4.7: *The plots and the fits (in red) of nuclei from H to Fe in CHDY after cut pre-selection in the IMC-CHDX plane, and the charge resolution for the CHDY.*

4.3.1 Charge resolution in CHDX+CHDY

A better charge resolution can be obtained using the sum of CHDX, CHDY layers. In this case, in fact, it is expected to scale down approximately by a factor $1/\sqrt{2}$. In Fig. 4.8 the plots and the fits of nuclei from H to Fe in CHDX+CHDY after pre-selection are shown. The measured charge resolution σ for the CHDX+CHDY vs. Z is plotted in Fig. 4.9 for elements from proton to iron and it spans from $0.09\,e$ at H to about $0.28\,e$ at Fe. In the same figure the resolutions are fitted with a straight line (red): this implies that the width of the charge distribution increases linearly with Z, to a good approximation, as $\sigma = kZ$, where $k = 0.0074 \pm 0.0001$ from the fit.

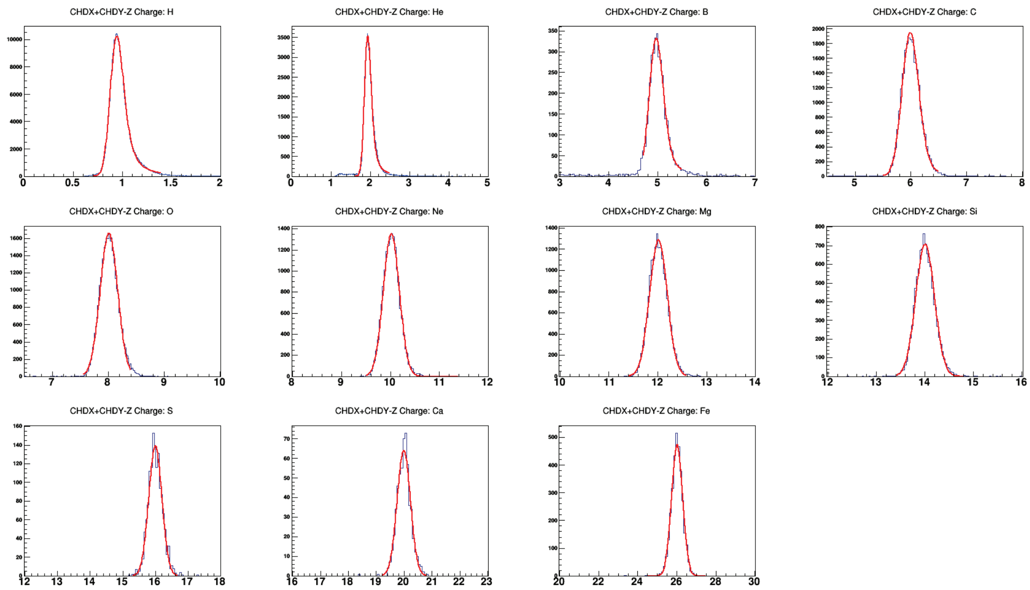

Figure 4.8: *The plots and the fits (in red) of nuclei from H to Fe in CHDY+CHDX after cut pre-selection.*

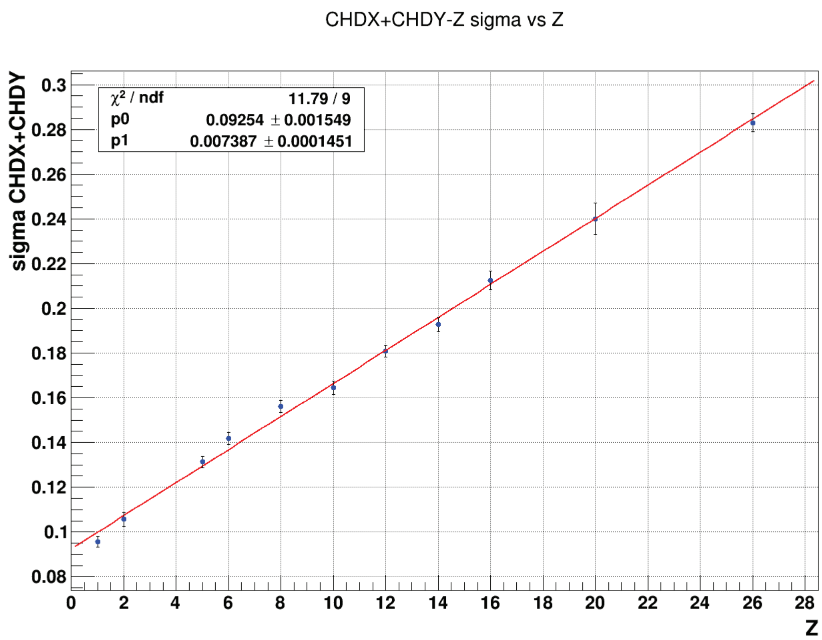

Figure 4.9: *Charge resolution plotted as a function of Z for nuclei from H to Fe in CHDY+CHDX. The solid line (red) is a linear fit.*

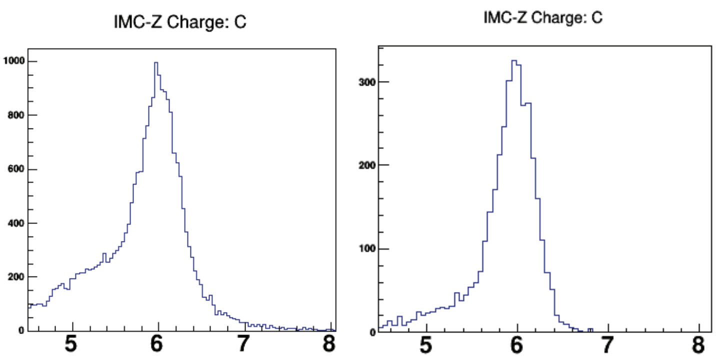

(a) Selection on CHDX-CHDY.

(b) Selection on CHDX-CHDY and last IMC plane.

Figure 4.10: *Plots for carbon in IMC plane.*

4.4 Charge resolution in IMC

In order to determine the variance of the charge distribution in IMC a pre-selection on an exclusive sample of events for each element in the CHDX-CHDY plane appears non adequate, as explained at the beginning of this chapter. The problem is that the plots of elements show a tail at lower charge values due to a misidentification of the interaction point in IMC. The idea to reduce the issue is to use the first 15 planes of IMC to calculate the mean before the interaction point, and to use the last IMC plane as additional selection in charge. In this way the particles that interact in IMC are reduced. The plots for carbon in IMC plane using only the selection in the CHDX-CHDY plane, and using the selection in the CHDX-CHDY plane and the last IMC plane are shown in Fig. 4.10 (a) and (b) respectively.

Then, the procedure is the same for the variance of the charge distribution in CHD.

Using this method, in Fig. 4.11 the plots and the fits of nuclei from H to Ne in IMC after pre-selection are shown. The measured charge resolution σ for the IMC vs. Z is plotted in Fig. 4.12 for elements from proton to neon and it spans from $0.11\,e$ at H to about $0.3\,e$ at Ne. In the same figure the resolutions are fitted with a straight line (blue). The width of the charge

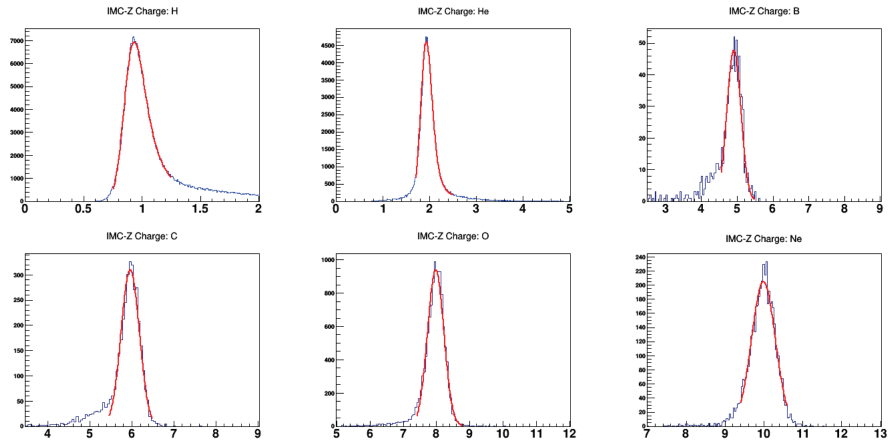

Figure 4.11: *The plots and the fits (in red) of nuclei from H to Ne in IMC after pre-selections cuts.*

distribution increases linearly with Z as $\sigma = kZ$ where $k = 0.019 \pm 0.001$ from the fit.

4.5 Charge resolution at the beam test

The performance of a scintillator paddle of CHD was studied at the GSI beam test [72]. During the beam test a Ni^{28+}_{64} primary beam was accelerated at an energy $E = 1000 - 1300 MeV/amu$ with an intensity of about $10^7 ions/spill$. A Be target $(1.036 g/cm^2\ )$ was used to produce different charged ions by fragmentation reactions. In this case the charge distributions provided by the scintillator were fitted with a multi-Gaussian parametrization for elements ranging from B to Fe and the variance of the charge distribution was determined by selecting a sample of events for each element. However the data were not corrected using the Tarlè parametrization (see Eq. (3.2.3)), but they remained saturated. The charge resolution was found to be close to $0.15\,e$ for boron, close to $0.25\,e$ at Si, while was found to be close to $0.3\,e$ for iron and sub-iron, as shown in Fig. 4.13. The observed $Z > 10$ dependence of σ is due to the non-linear relation between Z and the charge as a result of the light saturation effect in the scintillator.

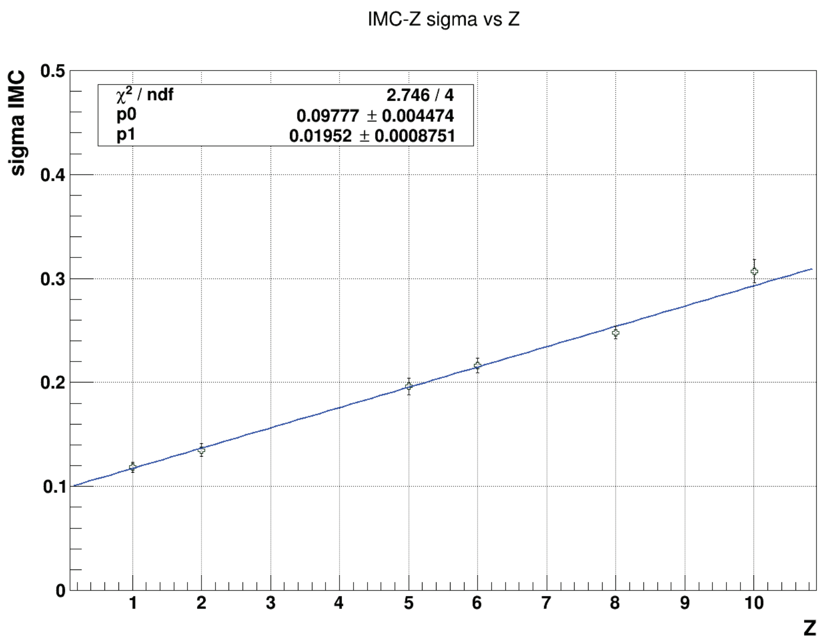

Figure 4.12: *Charge resolution plotted as a function of Z of nuclei from H to Ne in IMC. The solid line (blue) is a linear fit.*

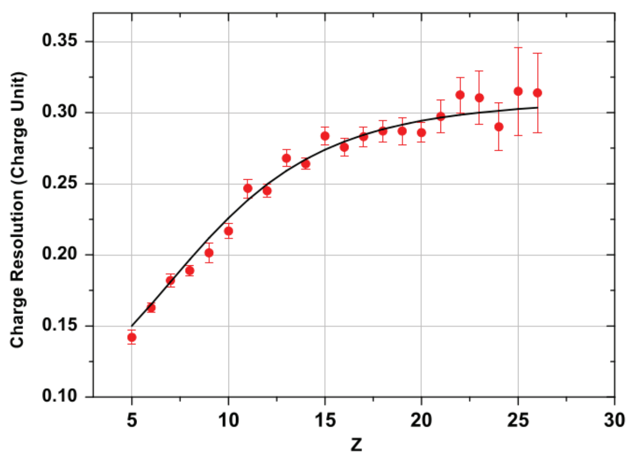

Figure 4.13: *Charge resolution plotted as a function of Z for nuclei from B to Fe with data taken at GSI [72].*

4.6 Charge identification in the B to O region

One of the science goals of the CALET experiment is the measurement of the ratio B/C of the fluxes of the two elements up to a few TeV/n. The charge separation of boron from carbon is of particular importance given that, to obtain a good measurement with reduced systematic errors, the requirement of 5σ separation of boron from carbon signal is necessary. The charge separation in units of σ between two consecutive elements of atomic number Z and $Z+1$ can be defined as the reciprocal of Eq. (4.3.1). So in the flight data, the charge separation of B from C results $\sim 7\sigma$, exceeding the 5σ requirement for CHDX+CHDY measurement and is near to the 5σ for IMC measurement, with charge resolution for boron and oxygen close to $0.13\,e$, $0.16\,e$ and to $0.2\,e$, $0.26\,e$ respectively. The results are consistent with those obtained at the GSI beam test where a charge resolution close to $0.15\,e$ for boron was found, exceeding the requirement for a 5σ separation from carbon.

4.7 Time stability of the charge measurement

In order to obtain the best charge resolution it is crucial that the MIP signal of a given nucleus does not change with time. Temperature variation due to the angle between the orbital plane of the ISS and the sun can be responsible for a RMS variations of 3% in Mip signal. This variations was successfully corrected, reducing the RMS variation to 1% as reported in [65].

Here a check on time stability of Mip signal is made for CHD and IMC detectors in order to avoid time dependence.

In Fig. 4.14 (a) the variations of proton signal over a period of nine months for CHD is reported. Each point corresponds to two weeks of data and the straight line represents a linear data fit. As one can see the deviation from the fitted line is lower than 0.2%. The analogous plot for IMC is shown in Fig. 4.14 (b). The variation is less than 0.2% here too, except for the period from 1st to 15th February 2016. This confirms the goodness of correction.

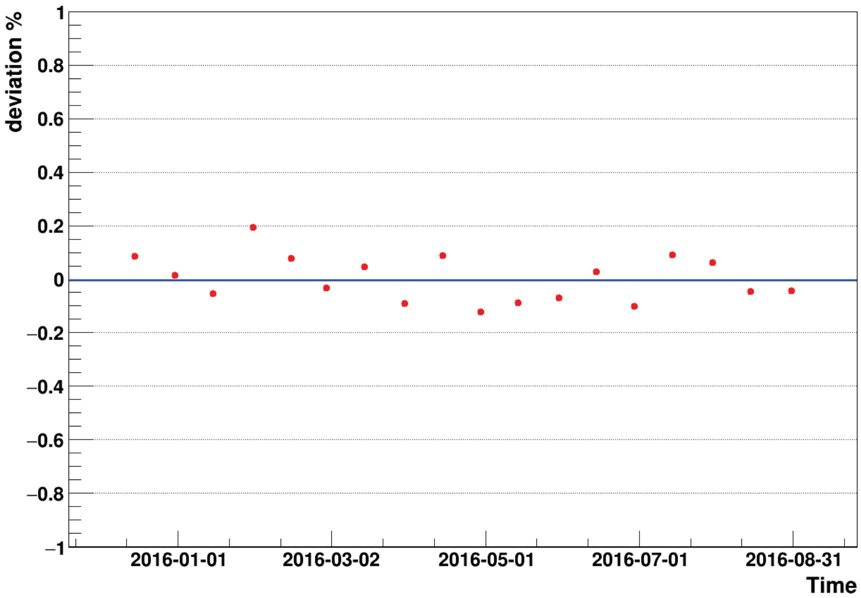

(a) CHD.

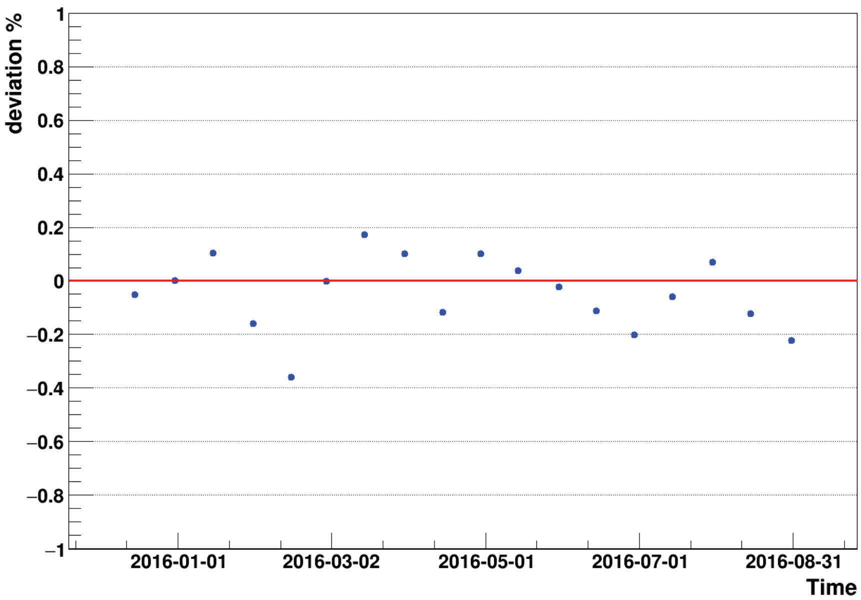

(b) IMC.

Figure 4.14: *The deviation (%) of proton signal from straight line fit from December 2015 to August 2016.*

4.8 Combined charge identification with CHD and IMC

In the previous sections the performances in charge resolution of CALET have been described. Both IMC and CHD have a good charge resolution, especially for light elements, so the idea is to use both detectors for the charge identification of cosmic nuclei. In order to separate single elements one can correlate the charge measurements in the IMC with the charge measurements in the CHD as shown in the Fig. 4.15 where the IMC signal is plotted vs. CHD signal. In this case, in order to remove events that interact in the CHD, consistency between the charge assignment from two CHD layers is required within 15%. Efficiency of this cut is around 85% for nuclei from B to Ne and around 65% for He and H. It is clear that well separated charges with flat background emerge from the plot 4.15 for H and He and for elements from B to Ne.

Using an elliptical selection cut, (as described in section 4.2) in the plane CHD-IMC, a clean charge separation is possible. It is important to note that, a clear identification of each chemical species represents a crucial point in the data analysis aiming to a flux measurement.

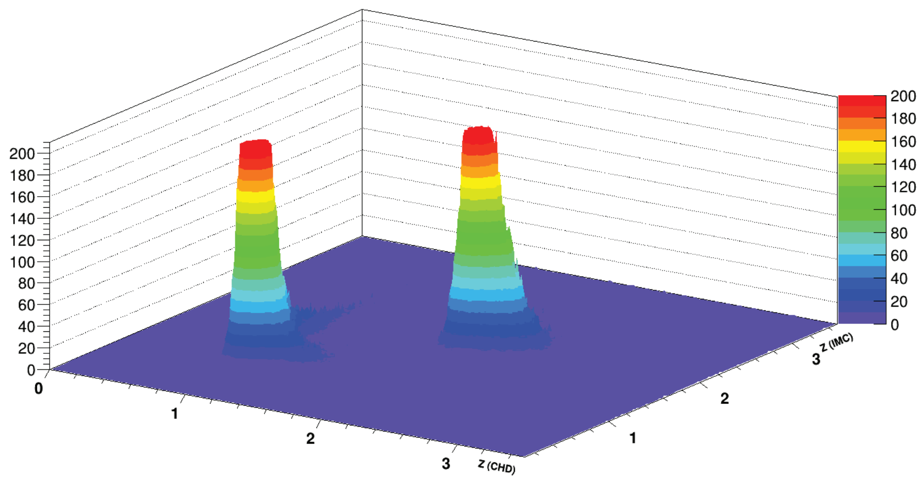

(a) Proton and Helium.

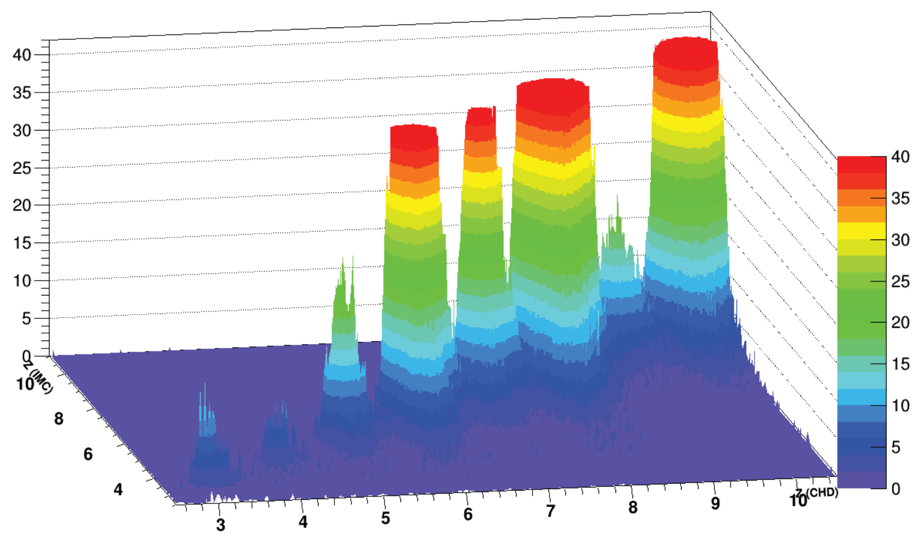

(b) Li, Be, B, C, N, O, F, Ne.

Figure 4.15: *Charge distributions in the CHD-IMC plane. The charge peaks of the most abundant elements have been chopped off in the picture to improve the visibility of the less abundant ones.*

Chapter 5

Current status of the CALET mission

From October 2015, CALET is collecting scientific data on the ISS. These data are sent to JAXA Tsukuba Space Center (TKSC) and immediately transferred to Waseda CALET Operations Center (WCOC) at Waseda University, for real time monitoring. In order to check the observation status of CALET in real-time and visualize cosmic-ray events, a quick look (QL) system was developed. This system monitors the orbit of ISS, the temperature trend of each part, the trigger rate of detectors, high voltage (HV) status and more. In WCOC, the scientific raw data (Level-0) are converted in into Level-1 data (the data format for scientific data analysis) and both data are used in a quick analysis: the results are used as feedback for better operation planning and more refined real-time monitoring. Physics analysis is performed using CALET Level-2 data, that are generated by applying detector calibrations to flight data.

At the time of writing, CALET has reached a total live time of $4.43 \times 10^7 s$, and a total number of HE events (on May 2017) of 3.89×10^8 (Fig. 5.1) Meanwhile data processing and scientific analysis of the first CALET observations are progressing smoothly.

In this Chapter a few examples of preliminary results of the CALET mission after ~ 1.5 years of data taking are shown.

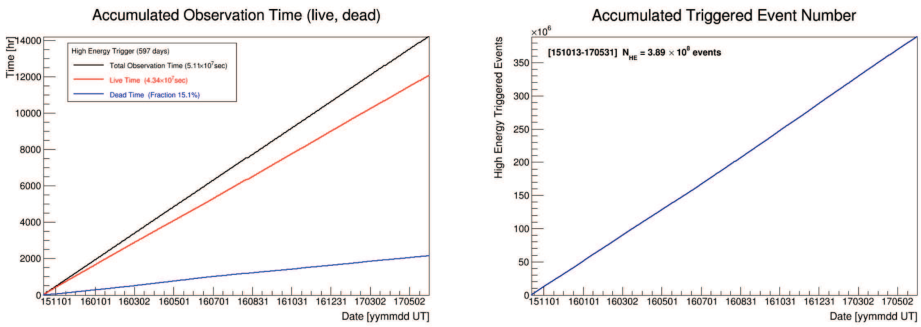

Figure 5.1: *Left: observation time (black line), live time (red) and dead time (blue). Total live time reaches* $4.43 \times 10^7 s$ *. Right: HE triggered events. Total number of HE events through the end of May 2017 reaches* 3.89×10^8 *(S. Ozawa, 2017 [74]).*

5.1 Preliminary measurements of nuclei

5.1.1 Preliminary proton energy spectrum

A preliminary proton analysis was carried out in order to measure the proton differential flux. In Fig. 5.2 the preliminary CALET results for the proton differential flux multiplied by $E^{2.7}$ vs. particle kinetic energy E are shown [75]. Proton is selected by an elliptical cut in the IMC-CHD plane. Helium and electron contamination, at percent level above $50\,GeV$, are subtracted. The flux is corrected for tracking efficiency, charge selection efficiency (flat at 95% above 50 GeV and around 90% at $10\,TeV$) and it is also corrected for HET efficiency. Energy unfolding is applied.

The figure shows good agreement with previous measurements within the statistical error. The full assessment of systematic errors is underway.

5.1.2 Preliminary light nuclei measurements

At the time of writing this thesis only a preliminary analysis on light nuclei was made. The analysis of the absolute and relative fluxes is under study. In Fig. 5.3 the dN/dE distributions of light nuclei from proton to oxygen as a function of the reconstructed calorimetric energy are reported.

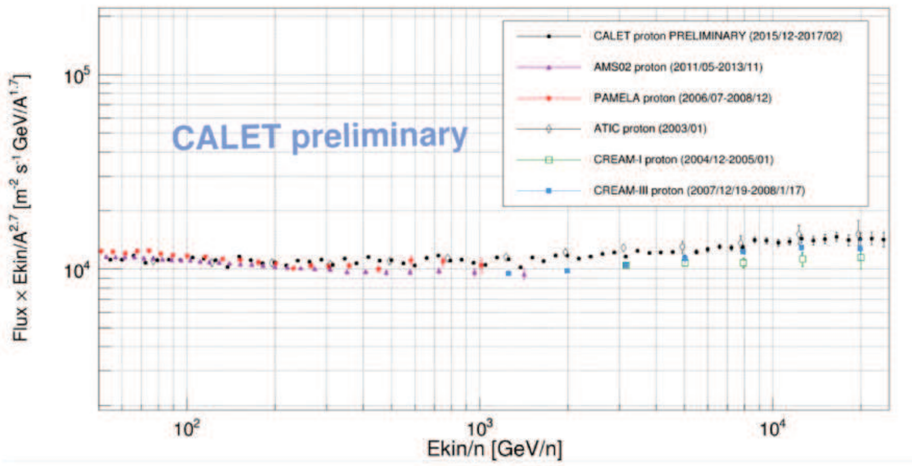

Figure 5.2: *Preliminary proton flux* $\times E^{2.7}$ *vs. particle kinetic energy E in* GeV *from* $50\,GeV$ *to* $22\,TeV$ *(black points). Only statistical errors are shown. Proton flux measurements by other experiments are also reported (P. Marrocchesi, 2017 [75]).*

Candidates that passed the CALET HET trigger, had well reconstructed track inside Acceptance-type 1 and passed the CHD charge consistency cuts are selected. The charge is selected in the IMC-CHD plane (see Chap. 4.8) by applying a circular cut of radius $0.8\,Z$ centred on the nominal charge Z for $Z > 2$.

5.1.3 Cosmic Ray swith Ultra High Charge (UHCR)

As seen in Chap. 2.3, CALET has the capability to study the UHCR abundances up to $Z = 40$ thanks to the large dynamic range of the charge measurement provided by the CHD detector. The Fig. 5.4 (left) and (right) summarize the preliminary result on UHCR measurements[1] for the first 18 months of CALET data. In Fig. 5.4 (left) the events that passed the CALET UH trigger, with well reconstructed trajectories, within 60° of vertical, compatible with CHD charge consistency cuts, and which had a geomagnetic vertical cutoff rigidity $> 4\,GV$ are reported. It is important to note that

[1]The preliminary measurements were reported in [76].

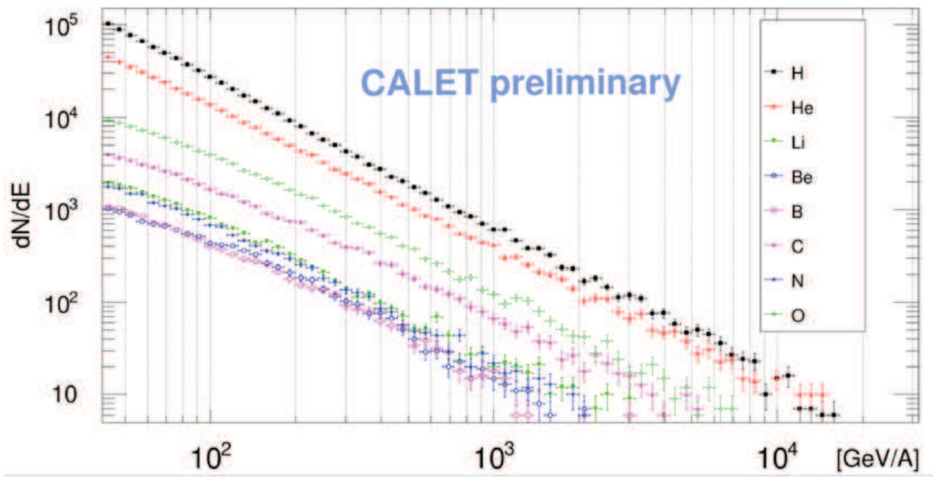

Figure 5.3: *Preliminary energy distribution dN/dE in kinetic energy per nucleon [GeV/A] for light elements from proton to oxygen from a sub-sample of the available data collected in a restricted fiducial volume (P. Marrocchesi, 2017 [75]).*

the cut based on geomagnetic rigidity eliminates lower energy events where the scintillation signal varies significanty with energy, so that it improves the charge resolution. The relative abundances to Fe are reported in Fig. 5.4 (right), together with Super-TIGER abundances.

5.2 Electron identification

The measurement of the electron+positron flux is one of the main science goal of CALET. The preliminary analysis that has been carried out so far required various steps in order to identify electrons. It started with selections on acceptance-1, HET trigger, and track reconstruction using several different algorithms mainly based on the IMC fiber signals. Acceptance-1 was selected because for this tipology of events the electromagnetic showers are almost fully contained in the calorimeter so that only a small correction ($< 5\%$) of the energy deposited in the calorimeter is needed in order to assess the true energy of the electron. An additional selection that rejected events outside acceptance-1 was applied reducing the contamination in the electron flux at

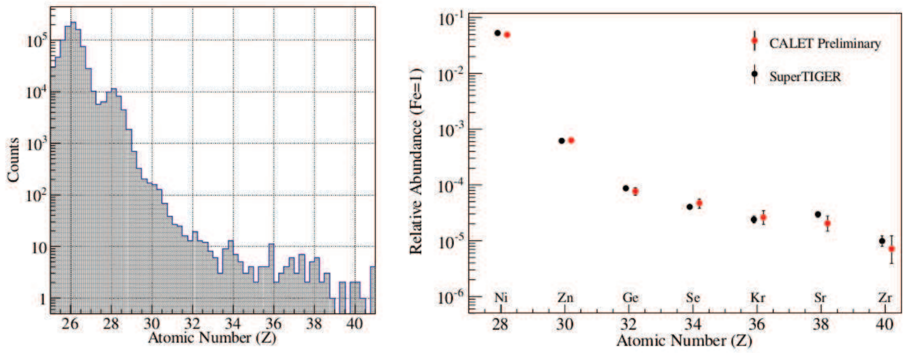

Figure 5.4: *Left: Preliminary CALET UHCR charge measurements. Right: Even-Z relative abundances to Fe for CALET (red points) compared with Super-TIGER (black points) (B. Rauch and Y. Akaike, 2017 [76]).*

less than 1.5%. A charge cut is also applied in CHD in order to reject He and heavier nuclei. The total efficiency of these selection cuts is $\sim 97.5\%$ from 100 GeV to 1 TeV.

The electron identification was performed by exploiting the shower shape difference between electromagnetic and hadronic showers. Two methods were applied: a simple two parameters selection and multivariate analysis (MVA) with boost decision tree (BDT). The first one uses a cut on K parameter defined by $K = log_{10}(F_E) + 0.65\, R_E$, where R_E is the second moment of the lateral energy-deposit distribution in the TASC first layer with respect to the shower axis, and F_E is the fractional energy deposit of TASC-Y6 layer sum with respect to the TASC total sum. In the second one, additional discriminant variables were included besides R_E and F_E [77], [78]: parameters from the fit of the longitudinal shower development in TASC, and parameters of the fit to the pre-shower development with an exponential function in IMC. Results for the electron identification are shown in Fig. 5.5 (a) and (b) for K and BDT methods respectively. The proton contamination fraction in the final sample of electron candidates below 1 TeV resulted around 5% with the BDT and 8% with K-cut analysis.

The electron differential flux was measured according to the following

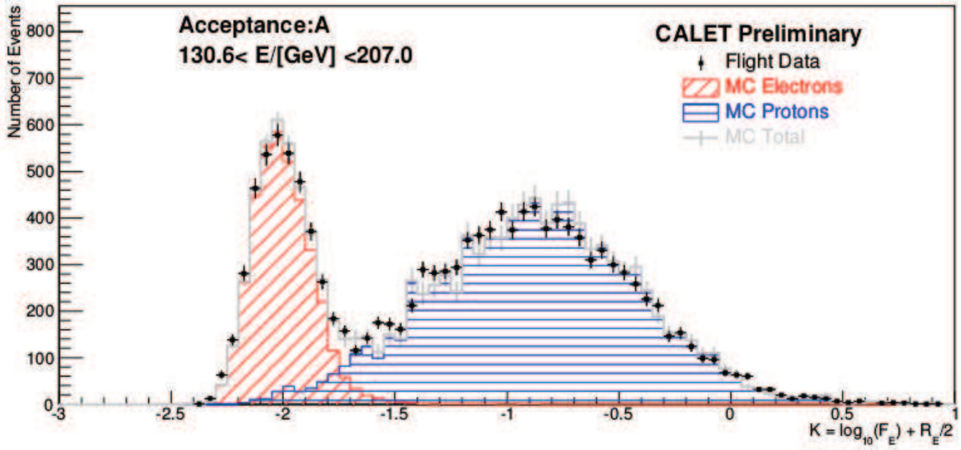

(a) K-cut analysis.

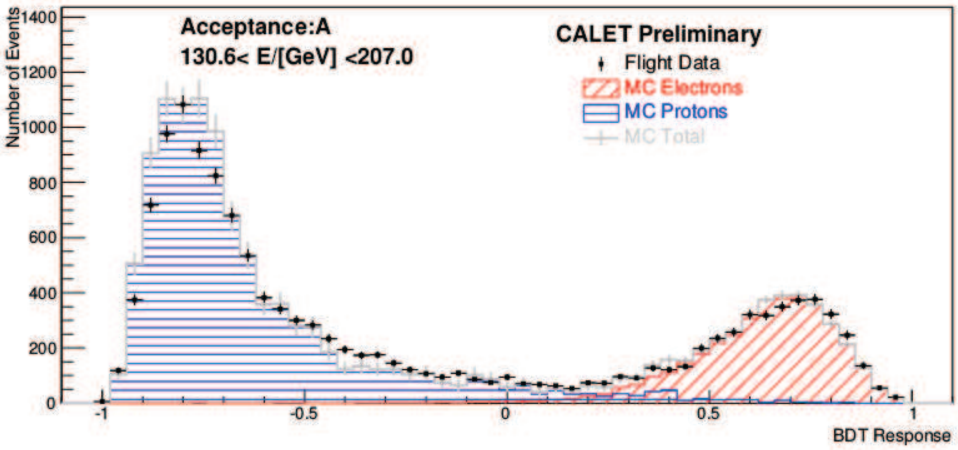

(b) BDT analysis.

Figure 5.5: *Electron identification with K-cut (a) and BDT (b) in the* $131 < E < 207GeV$ *bin. Black points represent flight data, whereas red and blue histograms represent MC simulation for electrons and protons, respectively (Y. Asaoka, 2017 [78]).*

expression:

$$\Phi(E) = \frac{N(E) - N_{BG}(E)}{S\Omega\varepsilon(E)T(E)\Delta E(E)} \tag{5.2.1}$$

where $N(E)$ is the number of electron candidates in the corresponding energy bin, $N_{BG}(E)$ is the number of background events estimated as MC protons, $S\Omega$ is the geometrical acceptance, $\varepsilon(E)$ is the detection efficiency for electrons, and $T(E)$ is the observational live time. A preliminary spectrum of total electrons (electrons + positrons) was obtained in an energy range of $10\,GeV$ to $1\,TeV$. It was presented at the International Cosmic Ray Conference 2017 [78] and has been submitted for publication.

5.3 Gamma-ray bursts detected by CALET

Until the end of May 2017, the CGBM has detected 65 GRBs, corresponding to a GRB detection rate of about 40 per year. The 18% of the total were short GRBs. An example of very bright, long GRB is the 160625B that was detected by CGBM at 22:40:15.49 (UT) together with many other instruments in flight as Fermi-GBM and LAT, Konus-Wind, INTEGRAL SPI-ACS and MAXI. The fluence and peak flux were estimated to be $5.0 \times 10^{-4}\, ergs\, cm^{-2}$ and $167 \pm 1\; photons\, cm^{-2} s^{-1}$ in the $10 - 1000\, keV$ range. In Fig. 5.6 the CGBM HXM1, 2 and SGM spectra of this GRB are shown up to $20\, MeV$.

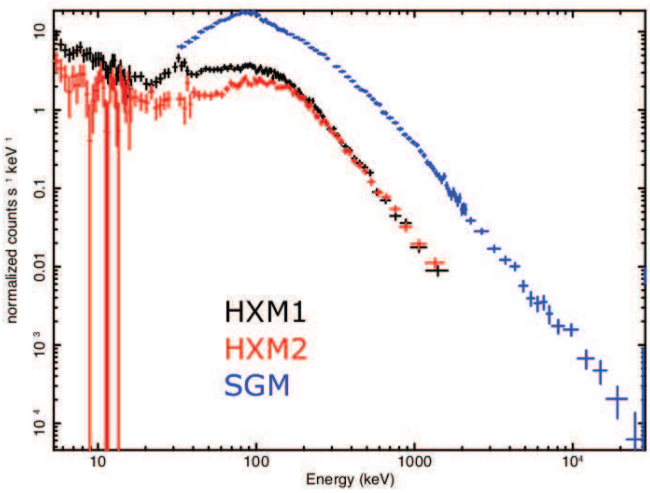

Figure 5.6: *CGBM spectra of GRB 160625B. X-ray and gamma-ray photons are clearly detected up to* $20\, MeV$ *(K. Yamaoka, 2017 [79]).*

5.3.1 Electromagnetic counterpart of Gravitational Wave (GW) with CALET

CALET has defined upper limits in the hard X-ray and gamma-ray bands at the time of the LIGO gravitational wave event GW 151226, showing that if there was an electromagnetic counterpart of GW, CALET would have the

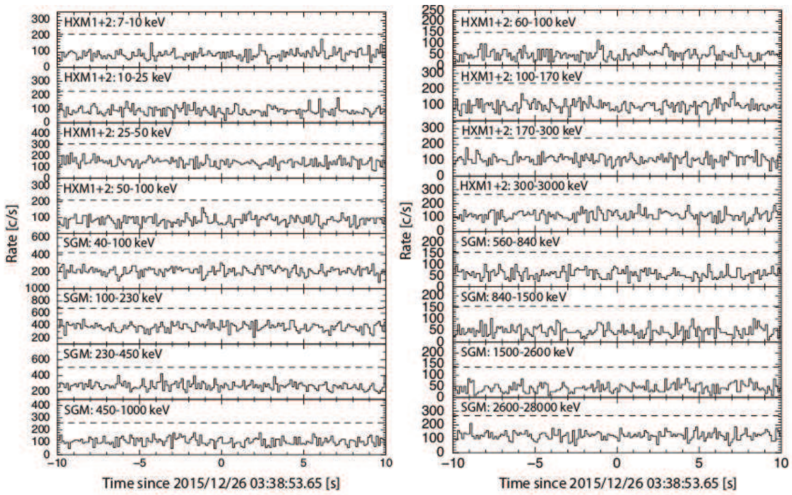

Figure 5.7: *The CGBM light curves in* $0.125\,s$ *time resolution for the high gain data (left) and the low-gain data (right). The time is offset from the LIGO trigger time of GW 151226. The dashed lines correspond to a* 5σ *level from the mean count rate using the data of* $\pm 10\,s$ *[80].*

capability to detected it (Adriani et al., 2016 [80]). GW 151226 is the 2nd gravitational wave candidate identified by both LIGO Hanford Observatory and LIGO Livingston Observatory at 3:38:53.647 UT on December 26, 2015. The luminosity distance of the source is estimated as $440^{+190}_{-180}\,Mpc$. Fermi-GBM, FermiLarge Area Telescope (LAT), High-Altitude Water Cherenkov Observatory (HAWC), and Astrosat-CZTI reported no detections of electromagnetic counterpart around the GW trigger time. CALET was fully operational at the time of GW 151226 and it was performing regular scientific data collection: the CAL was operating in the low-energy gamma-ray mode (operation mode with a lower energy threshold of 1 GeV), whereas the CGBM was operating in nominal operational mode, but there was no CGBM on-board trigger at the trigger time of GW 151226. The CGBM continuous light curve data in $0.125\,s$ time resolution were recorded at eight different energy bands for each instrument in the time range between $\pm 10\,s$ from the GW 151226 trigger time (Fig. 5.7). However, significant signals in the CGBM data associated with the gravitational-wave event were not detected. In order to understand whether the CGBM has the capability to detect GRBs generated at a distance of $440^{+190}_{-180} Mpc$ the flux upper limits of HXM and SGM are evaluated assuming a typical BATSE s-GRB spectrum. It was found that upper limits correspond to the k-corrected luminosity of $3.9 \times 10^{49} ergs^{-1}$ for HXM and $4.7 \times 10^{49} ergs^{-1}$ for SGM in the 1 keV - 10 MeV band. The isotropic-equivalent luminosity of s-GRBs is in the range from $5 \times 10^{48} ergs^{-1}$ to $1 \times 10^{52} ergs^{-1}$ with an average of $6 \times 10^{51} ergs^{-1}$. Therefore, if s-GRBs occur within 440 Mpc, CGBM could detect a signal from the majority of s-GRBs. In Fig. 5.8 (a) the sky maps of the 7σ upper limit overlaid with the shadow of ISS are shown.

Gamma-ray events associated with GW 151226 were searched for using the CAL data in the time interval from $-525\,s$ to $+211\,s$ around the LIGO trigger, applying a selection by tracking pair creation events in the imaging calorimeter: no gamma-ray candidate inside this time window was found. The CAL upper limit, was estimated assuming a single power-law model with a photon index of -2 by applying the estimated exposure map. It was found that the flux upper limit at 90% confidence level is $2 \times 10^{7} erg\, cm^{-2} s^{-1}$, corresponding to a luminosity of $5 \times 10^{48} ergs^{-1}$ in the 1 - 100 GeV band where CAL reaches 15% of the integrated LIGO probability. So, if s-GRBs occur within 440 Mpc, the CAL could detect a signal from a majority of s-GRBs. In Fig. 5.8 (b) the sky map of the flux upper limit at 90% confidence level is shown.

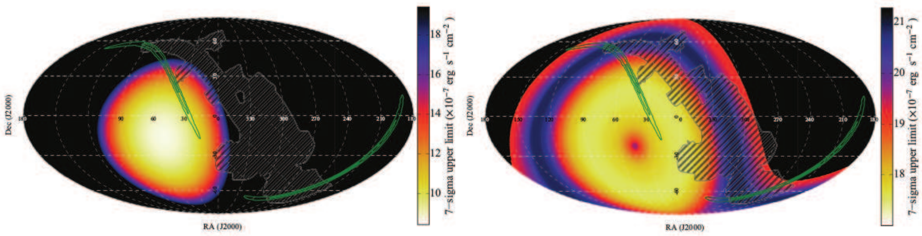

(a) The sky maps of the 7σ upper limit for HXM (left) and SGM (right). The energy bands are $7-500\,keV$ for HXM and $50-1000\,keV$ for SGM. The GW 151226 probability map is shown in green contours. The shadow of ISS is shown in black hatches.

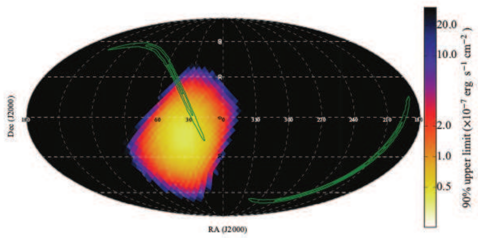

(b) The sky map of the 90% upper limit for CAL in the $1-100\,GeV$ band. The GW 151226 probability map is shown in green contours.

Figure 5.8: *The sky maps for HXM and SGM and CAL [80].*

Brief summary of candidate's activity

The candidate started its research activity as a Ph.D. student in 2014. During the first period he participated in the analysis of the CHD prototypes data of the beam test performed at CERN in March 2015. During this beam test a CALET prototype was studied with relativistic ions obtained from fragmentation of primary argon nuclei at energies 13, 19 and 30 GeV/n. In particular he focused his efforts on understanding the light saturation effect of the CHD plastic scintillators. These studies were then carried on using CALET flight data: the candidate corrected the saturations effects both in the CHD and in the IMC using an improvement of Tarlé parametrization. The results of this analysis are reported in Chap.3. In addition to the correction for the quenching effect in the CHD and IMC, the candidate focused its work on an aspect of the energy calibration process regarding the energy position dependence correction in the CHD. Then, in perspective of in-flight measurements of the spectra of light element, he studied the performance in terms of the charge resolution of CHD and IMC, confirming the important role of the IMC in the charge identification. The results of this analysis are reported in Chap.4. In September 2016 he attended the 102nd National Congress of the Italian Physical Society (SIF) in Padua, where he presented an overview on the gamma-ray bursts detected by CALET, and on the CALET capability to detected the electromagnetic counterpart of gravitational wave (GW)151226 [80].

List of Figures

List of Tables

Bibliography

[1] V. F. Hess: *Über Beobachtungen der durchdringenden Strahlung bei sieben Freiballonfahrten.* Physikalische Zeitschrift, 13:1084–1091, November 1912.

[2] W. Kolhörster: *S.N.* Physikalische Zeitschrift, 14:1153, 1913.

[3] D. Skobel'cyn: *Ubereine neue Art sehr schneller β-strahlen.* Zeitschrift für Physik, 54:686–702, 1929.

[4] C. Anderson: *The apparent existence of easily deflected positives.* Science, 76:238–239, 1932.

[5] P. Blackett and G. Occhialini: *Some Photographs of the Tracks of Penetrating Radiation.* Proceedings of the Royal Society of London., A139:699–726, 1933. `http://www.jstor.org/stable/96057`.

[6] P. Auger *et al.*: *Extensive Cosmic-Ray Showers.* Reviews of Modern Physics, 11:288–291, 1939. `http://link.aps.org/doi/10.1103/RevModPhys.11.288`.

[7] J. Simpson: *Elemental and isotopic composition of Galactic cosmic rays.* Annual Reviews of Nuclear and Particle Science, 33:323–381, 1983.

[8] S. Swordy: *The energy spectra and anisotropies of cosmic rays.* Space Science Reviews, 99:85–94, 2001.

[9] S. Potgieter: *Solar Modulation of Cosmic Rays.* Living Reviews in Solar Physics, 10, 2013.

[10] Todor Stanev: *High Energy Cosmic Rays.* Springer-Verlag Berlin Heidelberg, 2010.

[11] J. Beringer *et al.*: *Review of Particle Physics.*

[12] K. Greisen: *End to the cosmic-ray spectrum?* Physical Review Letters, 16:748–750, 1966.

[13] G. Zatsepin and V. Kuzmin: *Upper limit of the spectrum of cosmic rays.* Soviet Journal of Experimental and Theoretical Physics Letters, 4:78–80, 1966.

[14] W. Cronin: *The highest-energy cosmic rays.* arXiv:astro-ph/0402487. `https://arxiv.org/abs/astro-ph/0402487`.

[15] E. Fermi: *On the origin of the cosmic radiation.* Physic Reviews., 75:1169–1174.

[16] Leer E. Axford, I. and G. Skadron: *The acceleration of cosmic rays by shock waves.* Proceedings of the 15th International Cosmic Ray Conference, 11:132–135, 1977.

[17] G. Krymsky: *A regular mechanism for the acceleration of charged particles on the front of a shock wave.* Doklady Akademiya Nauk SSSR, 234:1306–1308, 1977.

[18] A. Bell: *The acceleration of cosmic rays in shock fronts.* I, Monthly Notices of the Royal Astronomical Society, 182:147–156, 1978.

[19] R. Blandford and J. Ostriker: *Particle acceleration by astrophysical shocks.* Astrophysical Journal, 221:L29–L32, 1978.

[20] P. Lagage and C. Cesarsky: *The maximum energy of cosmic rays accelerated by supernova shocks.* Astronomy and Astrophysics, 125:249–257, 1983.

[21] Berezhko E.: *Maximum energy of cosmic rays accelerated by supernova shocks.* Astroparticle Physics, 5:367–378, 1996.

[22] V. Ginzburg and S. Syrovatskii: *The Origin of Cosmic Rays*. 1964.

[23] A. Hillas: *The origin of ultra-high-energy cosmic rays.* Annual Review of Astronomy and Astrophysics, 22:425–444, 1984.

[24] M. Ahlers *et al.*: *Latin-American School of High-Energy Physics.* FERMILAB-FN-0847-A, YITP-SB-10-01.

[25] A. Strong and I Moskalenko: *Propagation of cosmic-ray nucleons in the Galaxy.* The Astrophysical Journal, 509:212–228, 1998.

[26] Thomas K. Gaisser: *Cosmic Rays and Particle Physics*. 1990.

[27] A. Obermeier *et al.*: *Galactic propagation of cosmic rays and the B/C ratio.* 32nd International Cosmic Ray Conference.

[28] A. Strong and I Moskalenko: *Model for Galactic Cosmic Ray Propagation.* Invited talk at the 33rd COSPAR Scientific Assembly.

[29] J. Engelmann *et al.*: *Charge composition and energy spectra of cosmic-ray nuclei for elements from Be to Ni - Results from HEAO-3-C2.* Astronomy and Astrophysics, 233:96–111, 1990.

[30] S. Swordy *et al.*: *Relative abundances of secondary and primary cosmic rays at high energies.* Astrophysical Journal, 349:625–633, 1990.

[31] W. Webber *et al.*: *Voyager Measurements of the Charge and Isotopic Composition of Cosmic Ray Li, Be, and B Nuclei and Implications for Their Production in the Galaxy.* Astrophysical Journal, 568:210, 2002.

[32] M. Aguilar *et al.*: *Relative Composition and Energy Spectra of Light Nuclei in Cosmic Rays: Results from AMS-01.* Astrophysical Journal, 724:329–340, 2010.

[33] K. Lave *et al.*: *Galactic cosmic-ray energy spectra and composition during the 2009-2010 solar minimum period.* Astrophysical Journal, 770:117, 2013.

[34] A. Oliva *et al.*: *Precision Measurement of the Cosmic Ray Boron-to-Carbon Ratio with AMS.* 33nd International Cosmic Ray Conference.

[35] N. Yanasak *et al.*: *Measurement of the Secondary Radionuclides ^{10}Be, ^{26}Al, ^{36}Cl, ^{54}Mn, and ^{14}C and Implications for the Galactic Cosmic-Ray Age.* Astrophysical Journal, 563:768, 2001.

[36] S. Stephens and R. Streitmatter: *Cosmic-Ray Propagation in the Galaxy: Techniques and the Mean Matter Traversal.* Astrophysical Journal, 505:266, 1998.

[37] B. Wiebel-Sooth *et al.*: *Cosmic rays. VII. Individual element spectra: prediction and data.* Astrophysical Journal, 330:389–398, 1998.

[38] S. Torii *et al.*: *The Calorimetric Electron Telescope (CALET) for High Energy Astroparticle Physics on the International Space Station.* 33nd International Cosmic Ray Conference, 2013.

[39] K. Yamaoka *et al.*: *CALET Gamma-ray Burst Monitor (CGBM).* 33nd International Cosmic Ray Conference, 2013.

[40] Y. Shimizu *et al.*: *The CALET CHD for determination of nuclear charge.* 32nd International Cosmic Ray Conference, 2011.

[41] P. Brogi: *Tracking and Identification of Proton and Helium in CALET and Perspectives for Flux Measurements.* Ph.D Thesis, 2015.

[42] I. Daijito *et al.*: *High-dynamic range readout system using dual APD/PD for the CALET-TASC.* 32nd International Cosmic Ray Conference, 2011.

[43] CALET D.H.&A. Japan: *CALET Trigger System.* internal note WCOC-2015-001NC, 2015.

[44] J. Sullivan: *Geometrical factor and directional response of single and multi-element particle telescopes*. Nuclear Instruments and Methods, 95:5, 1971.

[45] T. Kobayashi *et al.*: *The Most Likely Sources of High-Energy Cosmic-Ray Electrons in Supernova Remnants*. The Astrophysical Journal, 601:340–351, 2004.

[46] K. YOSHIDA *et al.*: *The science objectives for CALET*. 32nd International Cosmic Ray Conference, 2011.

[47] H. Motz *et al.*: *CALET Sensitivity to Dark Matter and Astrophysical Sources*. 35nd International Cosmic Ray Conference, 2015.

[48] O. Adriani *et al.*: *Cosmic-Ray Positron Energy Spectrum Measured by PAMELA*. Physical Review Letters, 111:081102, 2013.

[49] M. Aguilar *et al.*: *Electron and Positron Fluxes in Primary Cosmic Rays Measured with the Alpha Magnetic Spectrometer on the International Space Station*. Physical Review Letters, 113:121102, 2014.

[50] B. Carr *et al.*: *Cosmological constraints on primordial black holes*. Physical Review D, 81:104019, 2010.

[51] H. Cheng *et al.*: *Kaluza-Klein Dark Matter*. Physical Review Letters, 89:211301, 2002.

[52] G. Servant *et al.*: *Is the lightest Kaluza-Klein particle a viable dark matter candidate?* Nuclear Physics B, 650:391, 2003.

[53] A. Ibarra *et al.*: *Decaying dark matter in light of the PAMELA and Fermi LAT data*. Journal of Cosmology and Astroparticle Physics, 009:1–22, 2010.

[54] L. Bergström *et al.*: *Neutralino gamma-ray signals from accreting halo dark matter*. Physical Review D, 63:083515, 2001.

[55] P. Marrocchesi *et al.*: *CALET on the ISS: a high energy astroparticle physics experiment*. XIV International Conference on Topics in Astroparticle and Underground Physics, 718, 2016.

[56] E. Blasi *et al.*: *Spectral breaks as a signature of cosmic ray induced turbulence in the Galaxy*. Physical Review Letters, 109(6):061101, 2012.

[57] Y. Yoon *et al.*: *S.n.* The Astrophysical Journal, 714:89, 2010.

[58] O. Adriani *et al.*: *PAMELA Measurements of Cosmic-Ray Proton and Helium Spectra*. Science, 332:69, 2011.

[59] M. Aguilar *et al.*: *Precision Measurement of the Proton Flux in Primary Cosmic Rays from Rigidity* $1GV$ *to* $1.8TV$ *with the Alpha Magnetic Spectrometer on the International Space Station*. Physical Review Letters, 114:171103, 2015.

[60] E. Berezhko *et al.*: *A Simple Model of Nonlinear Diffusive Shock Acceleration*. The Astrophysical Journal, 526:385–399, 1999.

[61] P. Maestro: *High-energy astroparticle physics with CALET*. 23rd European Cosmic Ray Symposium, Journal of Physics, 409:012026, 2013.

[62] P. Marrocchesi *et al.*: *CALET measurements with cosmic nuclei and performance of the charge detectors*. 33nd International Cosmic Ray Conference, 2013.

[63] B. Rauch *et al.*: *Predicted CALET Measurements of Heavy and Ultra-Heavy Cosmic Ray Nuclei*. 34nd International Cosmic Ray Conference, 2015.

[64] B. Rauch *et al.*: *Cosmic Ray origin in OB Associations and Preferential Acceleration of Refractory Elements: Evidence from Abundances of Elements* $_{26}Fe$ *through* $_{34}Se$. The Astrophysical Journal, 697:2083–2088, 2009.

[65] Y. Asaoka *et al.*: *Energy calibration of CALET onboard the International Space Station*. Astroparticle Phisycs, 91:1–10, 2017.

[66] G. Tarlé *et al.*: *Cosmic Ray Isotope Abundances From Chromium to Nickel*. The Astrophysical Journal, 230:607–620, 1979.

[67] P. Ahlen: *Theoretical and experimental aspects of the energy loss of relativistic heavily ionizing particles*. Reviews of Modern Physics, 52:121, 1980.

[68] J. Birks: *The Theory and Practice of Scintillation Counting*. Pergamon, New York, 1964.

[69] C. Chou: *The Nature of the Saturation Effect of Fluorescent Scintillators*. Physical Review, 87:904, 1952.

[70] A. Meyer and R. Murray: *Effect of Energetic Secondary Electrons on the Scintillation Process in Alkali Halide Crystals*. Physical Review, 128:98, 1962.

[71] R. Voltz *et al.*: *Influence of the Nature of Ionizing Particles on the Specific Luminescence of Organic Scintillators*. The Journal of Chemical Physics, 45:3306, 1966.

[72] P. Marrocchesi *et al.*: *Beam test performance of a scintillator-based detector for the charge identification of relativistic ions*. Nuclear Instruments and Methods in Physics Research, A-569:477–483, 2011.

[73] P. Brogi *et al.*: *CALET measurements with cosmic nuclei: expected performances of tracking and charge identification*. 34nd International Cosmic Ray Conference, 2015.

[74] S. Ozawa: *CALET on-orbit operations and data analysis system at the Waseda CALET Operations Center(WCOC)*. 35nd International Cosmic Ray Conference, 2017.

[75] P. Marrocchesi: *Observation of Protons and Light Nuclei with CALET: Analysis and Preliminary Results*. 35nd International Cosmic Ray Conference, 2017.

[76] B. Rauch and Y. Akaike: *Status of the CALET Ultra Heavy Cosmic Ray Analysis*. 35nd International Cosmic Ray Conference, 2017.

[77] L. Pacini: *Capability of electron identification for the CALET measurement*. 35nd International Cosmic Ray Conference, 2017.

[78] Y. Asaoka: *Analysis and Preliminary Results for the Cosmic Ray Electron Spectrum from CALET*. 35nd International Cosmic Ray Conference, 2017.

[79] K. Yamaoka: *CALET GBM Observations of Gamma-ray Bursts and Gravitational Wave Sources*. 35nd International Cosmic Ray Conference, 2017.

[80] O. Adriani *et al.*: *CALET upper limits on X-ray and gamma-ray counterparts of GW 151226*. The Astrophysical Journal Letters, 829.